Constraining the Mantle's Rheology using Methods in Uncertainty Quantification

Thesis by

Vishagan Ratnaswamy

In Partial Fulfillment of the Requirements for the
degree of
Doctor of Philosophy

Caltech

CALIFORNIA INSTITUTE OF TECHNOLOGY
Pasadena, California

2019
Defended October 23rd, 2018

Vishagan Ratnaswamy
ORCID: Vishagan Ratnaswamy 0000-0002-2371-807X

To my parents

ACKNOWLEDGEMENTS

This work would not have been possible without the contribution of many people who I have had the opportunity to work with. First and foremost, I would like to thank my advisor Michael Gurnis for introducing me to this project and having the patience to explain the geophysical concepts as well as the guidance to explore different ideas and challenges for these geophysical optimization problems. I would also like to thank my thesis committee members Prof. Dan Meiron, Prof. Mark Simons and Prof. Guruswami Ravichandran.

This work would not have been possible if it weren't for the collaboration with Prof. Georg Stadler, Johann Rudi and Prof. Omar Ghattas. Specifically, the discussions with Georg Stadler and Johann Rudi on various optimization topics as well as computational issues that have come up during this project has been very helpful. I would also like to thank the geodynamics research group, specifically Xiaolin Mao, Dan Bower, Laura Alisic, Mark Turner, Ting Yang, Xi Liu, Chris Gross for helpful discussions.

The administrative staff in both GALCIT and the Seismolab have been very helpful when whenever I needed help specifically Christine Ramirez, Donna Mireles, Rosemary Miller, Kim Baker-Gatchalian, Sarah Gordon, and Priscilla McLean. I would also like to thank my officemates Ollie Stephenson, Vasilije Dobrosavljevic, Minyan Zhong, Zhe Jia whom have always been a source of entertaining discussions.

I would also like thank the friends I have made here specifically, Cheikh Mbengue, Hilary Martens, Steve Perry, Jurg Schuler, Jose Luis Reyes, Chris Rollins who have all made my time wonderful. I'd also like to thank Darren and Kristy Wong for fun times hanging out whether it's having dinner/movie or just catching up. Another two people I want to thank are Christopher Berkeley and Edwin Abo for great advice, and all the fun times we had hanging out at Barneys before it closed down. The last set of people I would like to thank who I've met over the past two years are Ray Nhan, Robert, Brian Easton, John Dailey, Raymond, Andrew Chan, Adam Bolt, Roxanne Ramirez, Matt, Rigo, David, William, Leanne, Nick, Cheryl, John Hahn, Michele, Jason, Brian, Larry, and gboy.

I would like to thank my friends in New Jersey, who I've certainly not forgotten: Jenshi, Ade, Arpan, Amin, Dave, and Phil. I would like to thank my advisor from NJIT, Prof. Anthony Rosato who always has given me good advice and has been an important part of my academic journey. Finally, I would like to thank my parents who have always given me love and support throughout this journey.

ABSTRACT

An accurate estimation of the large-scale forces in the mantle has been difficult to obtain as numerical models either do not use an accurate rheology nor reproduce surface observations. While much work has been done in developing high-fidelity forward models that capture the salient physics of shear-thinning and dynamic weakening, they fail to reproduce observations such as plate motions and topography. In this thesis, we develop an optimization methodology that minimizes the misfit in surface observations such as plate motions and average effective viscosity for certain regions of the mantle. We utilize adjoints to calculate the gradient, while using second-order adjoints to construct the Hessian so as to infer the rheological parameters of the mantle's rheology. Furthermore, we build on this optimization scheme by constructing the Gaussian approximation of the posterior distribution for the inferred rheological parameters using the Hessian and establish the trade-offs between each parameter through their conditional distributions. We further extend this Gaussian approximation to infer extrinsic quantities such as the stresses in the fault zones and the average effective viscosity in the hinge zones to not only quantify the uncertainty, but also to see partitioning of the coupling of each subduction zone.

TABLE OF CONTENTS

Acknowledgements iv
Abstract vi
Table of Contents vii
List of Illustrations ix
List of Tables xv
Chapter I: Introduction 1
Chapter II: Adjoint-based estimation of plate coupling in a non-linear mantle flow model: theory and examples 9
Abstract 10
- 2.1 Introduction 11
- 2.2 Nonlinear Stokes Forward Problem 14
- 2.3 Bayesian inversion 16
- 2.4 Model Setup and Numerical Solution 23
- 2.5 Forward Model 26
- 2.6 Inverse Model 29
- 2.7 Quantification of Uncertainty 37
- 2.8 Discussion and Conclusions 43
- 2.9 Acknowledgments 48
- .1 Integration of viscosity bounds in rheology 48

Chapter III: The inverse of mantle flow with velocity and topography constraints 50
Abstract 51
- 3.1 Introduction 52
- 3.2 Forward Model 54
- 3.3 Bayesian Inverse Problem 55
- 3.4 Model Setup 60
- 3.5 Results 61
- 3.6 Discussion 64
- 3.7 Supplementary Material: Gradient and Hessian Tests 64
- 3.8 Cases 1 and 2 64
- 3.9 Cases 3-5 65

Chapter IV: Inference of plate boundary properties with an adjoint optimization with large scale two-dimensional models 67
Abstract 68
- 4.1 Introduction 69
- 4.2 Forward Model 71
- 4.3 Bayesian Problem Formulation 72
- 4.4 Model Setup 81
- 4.5 Results 86
- 4.6 Discussion 100

Chapter V: Future Work 108
Bibliography 111
Appendix A: Analysis of Data Covariance for Plate Motion Models 119
Abstract 120
  A.1 Introduction 121
  A.2 Transformation of Covariance 121
  A.3 Covariance Mapping 122
  A.4 Reference Frames 124
  A.5 No-Net Rotation Reference Frame 125
  A.6 Analysis of Corner Flow and its Application to Normal and Shear stresses in a Viscous Subduction Zone Model 137

LIST OF ILLUSTRATIONS

Number *Page*
1.1 Summary of forces in a suduction zone. 3
2.1 (a) Surface velocity from a forward calculation (thin blue line) and sub-sampling used to create the data for the inverse models (red lines). (b) $\log_{10}$ of the effective viscosity in Pa·s. (c) Detail of the effective viscosity for the left-most subduction zone overlaid by contours of temperature (in black). (d) Profile of the weak zone used in our dynamic model (black line) compared against a representative sample of global seismic coupling zones taken from the Slab 1.0 model (Hayes et al., 2012) (in grey). 27
2.2 (a) Change in plate velocity (as RMS across the top surface) as a function of plate coupling $\langle\Gamma\rangle$ for a set of models in which all three plate margins have the same coupling factor. Filled symbols denote the cases shown in panels b-d. Viscosity structure in the vicinity of right most subduction zone for three values of coupling: (b) $\langle\Gamma\rangle = 10^{-8}$, (c) $\langle\Gamma\rangle = 10^{-5}$, and (d) $\langle\Gamma\rangle = 1$ (e) Surface velocity profile of right most subduction zone at $\langle\Gamma\rangle = 1$. 28
2.3 Relationship between the normalized standard deviation σ (in blue) and the average plate velocity V_{rms} (in red) as a function of the plate coupling factor $\Gamma(= \Gamma_1 = \Gamma_2 = \Gamma_3)$ (a), and as a function of the average effective viscosity η_{eff} within the weak zones (b). 30
2.4 Convergence towards MAP points for Case XII (a–c) and for Case XIX (d–f). The plots show the convergence of Γ_i, n, and σ_y as function of the iteration. The open circles depict the iterates and the dashed horizontal lines show the values used to generate the synthetic data. 34

2.5 (a) Plate velocities from a forward calculation (blue curve) with a large coupling factor for right-most subduction zone. The distribution of velocities used to compute RMS velocities over 87% (pink line) and 47% (green line) over the right most plate. (b) Effective viscosity from the forward model. (c) Inverse with plate velocities (blue) of right-most subduction zone with green line denoting data. (d) Effective viscosity (Case XV). (e) Inverse with plate velocities (blue) and pink line denoting data over 87% of right most plate (Case XVII). (f) Effective viscosity (Case XVII). 35

2.6 Comparison of two-dimensional conditional distributions for the three parameters n, Γ and σ_y. Contour lines (for 22%, 44%, 66%, 88%) corresponding to the Gaussian approximation at the MAP point for a setting without a prior are shown in red and for the true posterior distribution are shown in blue. For these conditionals, the parameters kept fixed are in (a) $\sigma_y = 128.9$ MPa, in (b) $\Gamma = 10^{-5}$, and in (c) $n = 3$. Note that due to the parameterization in (2.14), the contour lines of the Gaussian approximation do not appear as ellipses when plotted in the original n, Γ and σ_y system. 39

2.7 Comparison of two-dimensional conditional distributions (with Gaussian priors) for the uncertain parameters n, Γ and σ_y. Shown are contour lines (22%, 44%, 66%, 88%) corresponding to the Gaussian approximation at the MAP point (in red), contour lines for the actual posterior distribtion (in blue) and contour lines for the prior distributions (grey). For these conditionals, the parameters kept fixed are in (a) $\sigma_y = 128.9$, in (b) $\Gamma = 10^{-5}$, and in (c) $n = 3$. 41

2.8 Comparison of two-dimensional marginal distributions for the unknown parameters n, Γ and σ_y. Contour lines (for 22%, 44%, 66%, 88%) for the marginals from the Gaussian approximation of the posterior distribution are shown in red. Contour lines for the marginals of the true postrior distribution, obtained from an MCMC sampling approach are shown in blue. (a) Marginals distributions for Γ vs. n (b) Marginal Distributions for σ_y vs. n (c) Marginal distributions for Γ vs. σ_y. 42

2.9 Chain history for weak zone factor Γ. 43

3.1 (a)Effective viscosity (b)Dynamic topography (km) with 4 % noise . 60

3.2 (a)Cases 1 and 2 (inference for weakfactor with only normal stress data) (b)Cases 3-5 (inference for strain rate exponent with only normal stress data) (c) Cases 6 and 7 (inference for activation energy with only normal stress data) (d)Weakfactor comparison between cases 8 and 13 (e)Strain rate exponent comparison between cases 8 and 13 (f)Activation energy comparison between cases 8 and 13 63

4.1 (A) Normal distributions for the strain rate exponent prior (B) Uniform distributions for the strain rate exponent prior. In (A) we compare the possibility of using two different normal distributions to demonstrate our knowledge or lack thereof of what the values of the strain rate exponent should be. 80

4.2 A. Velocity vectors in the no net rotation reference frame from MORVEL56(Argus, Gordon, and DeMets, 2011). Cross sections indicated with black lines, including western to eastern Pacific (WEP), Sumatra (SU), Tonga to Chile (TC) and Middle America (MA) B. Velocity in the direction of cross-section WEP.(C)Temperature distribution for cross section WEP. Zoom in of the Marianas (in D) and the Chilean (in E) slabs for the WEP cross section. In D and E, the solid green lines show the position of the weak zones. 84

4.3 (A) Effective viscosity in the final converged state of Case 1 for the WEP cross section. Distance in degrees east along the great circle. (B) Case 1 surface velocity at two different iterations (dashed lines) compared with plate motion data (solid blue line). The velocity near the Mariana plate margin is shown in detail. (C) Convergence of coupling factors for Case 1 (solid circles) and Case 6 (open squares) for the Chile (CHL in blue), Ryukyu (RYU in black), and Mariana (MAR in green) plate margins. Convergence for the non-linear exponent (n, shown in D) and yield stress (σ_y, shown in E) for three cases (Case 1 and 6 have the same symbol as in C while Case 14 is shown with the open diamond symbols). 90

4.4 Effective viscosity for Middle America: (A) the inversion Case 32 ($\Gamma = 7.75 \cdot 10^{-5}$, $\sigma_y = 139.1$ MPa, and $n = 3.062$); (B) zoom in of Middle America slab from Case 32; (C) otherwise identical forward model except $\Gamma = 4.0 \cdot 10^{-3}$; (D) otherwise identical forward model except ($\Gamma = 4.0 \cdot 10^{-5}$). 91

4.5 Case 1: Strain rate exponent vs. yield stress (A), yield stress vs. plate coupling (B), and strain rate exponent vs. plate coupline (C). Chile (red), Ryukyu (black) and Marianas (green). Cases 15, 24 and 32 (Sumatra in black, Tonga in red and Middle America in blue): Yield stress vs. strain rate exponent (D), yield stress vs. plate coupling (E), and non-linear exponent vs. plate coupling (F). Contour levels correspond to 30%, 60% and 90% probabilities. 92

4.6 The influence of priors on the conditional distribution of activation energy vs. strain rate exponent. Generic priors on (A) WEP and (B) Sumatra. For the WEP cross section, conditional distribution with permissive (C) and restrictive prior knowledge (D). Throughout, thin black contours are the priors, thick blue ones are conditionals without priors, and thick red ones are those with priors. (E) WEP model comparison for no-priors (blue contours) and restrictive priors (Γ_i vs. strain rate exponent) (F) WEP model comparison for no-priors (blue contours) and restrictive priors (Γ_i vs yield stress). Contour levels correspond to 30%, 60% and 90% probabilities. 96

4.7 Fault zone stresses (Tensile stresses are positive while compressive are negative). Results for the WEP with Case 6 with Chile (red), Ryukyu (black) and the Marianas (green) resolved for the (A) stress stress and the (B) normal stress. Results for the Sumatra (black, Case 16), Tonga (red, Case 24) and Middle America (blue for Case 35) resolved for the (C) shear stress and (D) normal stress. Contour levels correspond to 30%, 60% and 90% probabilities. 97

4.8 Principal stresses in the fault zones. Compression (-) and Tensional Axis (-) for (a)Middle America (Case 35) (b) Sumatra (Case 16) (c)Tonga (Case 24) (d)Chile (WEP) (e)Ryukyu and Marianas (WEP) Case 6 within the fault zone. 98

4.9 Principal stresses in the fault zones. Compression (-) and Tensional Axis (-) for (a)Middle America (Case 35) (b) Sumatra (Case 16) (c)Tonga (Case 24) (d)Chile (WEP) (e)Ryukyu and Marianas (WEP) Case 6 within the plates. 99

4.10 (A) Average effective viscosity vs. strain rate exponent in the upper mantle showing the influence of adding viscosity data to the inversion (blue, Case 12) compared to Case 6 without (green). (B) Average effective viscosity in hinge zones vs. strain rate exponent for Case 6. Note that all of the distributions are close for the three subduction zones in WEP and so they appear to overlie one another. Contour levels correspond to 30%, 60% and 90% probabilities. 99

4.11 (A) Convergence for the plate couplings in Case 7 for WEP (b) convergence for the strain rate exponent (c) convergence for the yield stress (Case 7 for WEP, Case 20 for Sumatra, Case 37 for Middle America and Case 28 for Tonga). 105

A.1 Plates on the surface of the earth and the vectors from (Argus, Gordon, and DeMets, 2011) 127

A.2 Plates on the surface of the earth with velocity vectors and corresponding error ellipses 127

A.3 Covariance data distributions for Nazca between each of its angular velocity components (a)ω_1 vs ω_2 (b)ω_1 vs ω_3 (c)ω_2 vs ω_3 128

A.4 Covariance data distributions for Pacific (conditioned on Amur) with a rotational component between each of its angular velocity components (a)ω_1 vs ω_2 (b)ω_1 vs ω_3 (c)ω_2 vs ω_3 129

A.5 Covariance data distributions for Pacific (conditioned on JDF) with a rotational component between each of its angular velocity components (a)ω_1 vs ω_2 (b)ω_1 vs ω_3 (c)ω_2 vs ω_3 130

A.6 Covariance data distributions for Pacific (conditioned on Nazca) with a rotational component between each of its angular velocity components (a)ω_1 vs ω_2 (b)ω_1 vs ω_3 (c)ω_2 vs ω_3 131

A.7 Covariance data distributions for Pacific (conditioned on Cocos) with a rotational component between each of its angular velocity components (a)ω_1 vs ω_2 (b)ω_1 vs ω_3 (c)ω_2 vs ω_3 132

A.8 Covariance data distributions for Pacific (conditioned on Nubia) with a rotational component between each of its angular velocity components (a)ω_1 vs ω_2 (b)ω_1 vs ω_3 (c)ω_2 vs ω_3 133

A.9 Covariance data distributions for Pacific (conditioned on Nubia) with a rotational component between each of its angular velocity components (a)ω_1 vs ω_2 (b)ω_1 vs ω_3 (c)ω_2 vs ω_3 134

A.10 Covariance data distributions for Pacific (conditioned on Nubia) with a rotational component between each of its angular velocity components (a)ω_1 vs ω_2 (b)ω_1 vs ω_3 (c)ω_2 vs ω_3 135
A.11 Covariance data distributions for Pacific (conditioned on Nubia) with a rotational component between each of its angular velocity components (a)ω_1 vs ω_2 (b)ω_1 vs ω_3 (c)ω_2 vs ω_3 135
A.12 Covariance data distributions for Pacific (conditioned on Nubia) with a rotational component between each of its angular velocity components (a)ω_1 vs ω_2 (b)ω_1 vs ω_3 (c)ω_2 vs ω_3 136

LIST OF TABLES

Number *Page*

2.1 Physical quantities used in our tests. 25

2.2 Parameter estimation results for several test cases. Each entry for the prefactors, yield stress, and strain rate exponent are given as inferred/true/standard deviation (log($\boldsymbol{m}$)). Quantities that are considered known and thus fixed in the inversion are shown in parentheses. The top surface velocity data is constant for each plate, and the percentage of the top surface with these constant velocity constraints is indicated in the second column. 31

2.3 Dissipation occurring locally and throughout the whole domain for selected cases. Values are shown as recovered/true. Symbols defined in text. 37

3.1 Case study summary for inversions for multiple parameters with different pieces of data used. Note T means topography, while v means velocity data used. 62

3.2 Inversion statistics for $\gamma_{\text{guess}} = 10^{-2}$ 65

3.3 Inversion statistics for $\gamma_{\text{guess}} = 10^{-3}$ 65

3.4 Inversion statistics for $n_{\text{guess}} = 2.85$ 65

3.5 Inversion statistics for $n_{\text{guess}} = 2.0$ 66

3.6 Inversion statistics for $n_{\text{guess}} = 3.5$ 66

3.7 Gradient check for activation energy with $E_a^0 = 4.0$ 66

4.1 Assumed parameters left as constants in the 84

4.2 Sensitivity of initial guesses for Case 1 87

4.3 Summary of inversions (**bold** values held fixed) 89

4.4 Summary of seismic coupling coefficients (χ_s) is the seismic coupling coefficient, while χ_g is the geodetic coupling coefficient (Scholz and Campos, 2012). 103

A.1 Comparison of correlations between Pacific and other plates, (ω_i, ω_j) represent the correlation of the Pacific plate's angular velocity with another plate of interest. 135

Chapter 1

INTRODUCTION

Plates moving on the earth's surface are a manifestation of circulation of the mantle which behaves as a viscous fluid on geological time scales (that is, greater than several thousand years). Plate tectonics is the kinematic description in which the earth's surface is divided into about a dozen plates; the plates have negligible strain internally and strain is concentrated at plate boundaries. Mantle convection is the dominant driving force of plate tectonics and is associated with the creation and destruction of plates including mountain building and volcanism at subduction zones. The viscous properties are attributed to creep of mantle minerals at high temperatures. Moreover, subduction of oceanic lithosphere where plates are returned to the mantle is associated with large magnitude earthquakes along some plate margins.

Developing an understanding of plate motion from a convection point of view involves formulating models of the mantle that capture surface observations along with an accurate description of viscous flow. The standard approach uses the steady-state Stokes (or momentum) equation which follows from assumptions made upon the Navier Stokes equations. The continuity equation is a statement of mass conservation, while the momentum equation is a reflection of a balance of forces. The mantle has a Prandtl number (ratio between kinematic viscosity to thermal diffusion) that is very large, $O(10^{22})$, with the inertial and nonlinear advective terms of the Navier Stokes equations being negligible.

In convection models meant to describe the system over time-scales longer than thousands of years, the mantle and plates are commonly assumed to be viscous. However, plates and mantle are visco-elastic and commonly described as a Maxwell body, the decay time of elastic stresses is the Maxwell time, $\frac{\mu}{\eta}$, where η the effective viscosity and μ the shear modulus. The Maxwell time likely varies substantially within plates and the mantle. For example, studies have suggest that the highest effective viscosities within plates is about $10^{23} Pa \cdot s$ and this leads to relaxation times of 10^5 years, while the viscosity of the upper mantle is about $10^{19} - 10^{21} Pa \cdot s$ with relaxation times from $10 - 10^3$ years. This suggests that on the million year time scales we are interested in, the elastic stress for the plates could be important, but they are not so within the bulk of the mantle. While the Maxwell decay time suggests that on geological time-scales, the oceanic plates behave like a viscous fluid, it is important to ascertain what role does elasticity play in the stresses within plates. Recent studies by Farrington et al. (2014) and Mao et al. (2017) have explored the role of visco-elasticity in the hinge-zone, where plates bend as they first subduct into the mantle. Although, the use of a visco-elastic model can give rise to a more accurate estimation of the stresses on the surface, leading to moderately different surface topographies Mao et al. (2017), argued that to a first-order, the viscous flow approximation is suitable for studying the large-scale tectonic forces within plates.

Numerical models aimed at describing mantle convection can either be instantaneous or time-dependent. For instantaneous models, the subject of this thesis, only the momentum equation resulting from assuming an infinite Prandtl number, the Boussinesq approximation, and incompressibility is used. Solving instantaneous models by assuming known buoyancy, one can predict surface velocity, topography and a host of other outcomes. If the objective is to investigate the evolution of plates, plate boundaries and the mantle, then the momentum and continuity equations need to be coupled to the advection-diffusion equation. Coupling to the advection-diffusion equation is beyond the scope of this thesis.

The primary forces in a subduction zone are slab pull, ridge push, the bending force in the hinge zone, the anchor force from the pressure and the lower mantle resisting force (Fig.1.1). Slab pull is likely the primary force driving plate motions (Forsyth and Uyeda, 1975; Chapple and Tullis, 1977) and is estimated to account for approximately 70% of the driving forces in the mantle (Conrad and Lithgow-Bertelloni, 2002). An important constraint in models is reproducing the asymmetric motion at subduction zones. Without the direct coupling of slabs to the down-going plate, there would be symmetric convergence at subduction zones (Conrad and Lithgow-Bertelloni, 2002). Ridge push and slabs in the lower mantle may also be important as they act as a 'push force' and a resisting force respectively. Some key resisting forces include a bending force, when slabs first bend during subduction, and the frictional resistance between plates and faults. The bending of plates at a subduction zone (Fig. 1.1) can lead to significant dissipation (Conrad and Hager, 1999); however, the stresses in the bending zone may not be accurately approximated by viscous flow models, leading to varying estimates of viscous dissipation (Buffett and Rowley, 2006; Buffett and Becker, 2012). Slabs may act as stress-guides (Elsasser, 1969), allowing stresses to propagate from the lower mantle

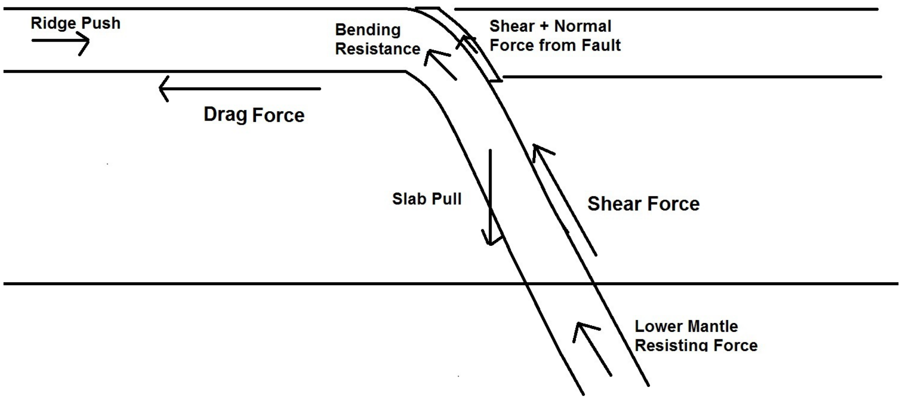

Figure 1.1: Summary of forces in a suduction zone.

to the oceanic lithosphere (Stadler et al., 2010). The propagation of stresses through the high viscosity slabs act to resist plate motion due to the increase in viscosity from the upper to lower mantle.

Mapping out the forces at subduction zones is important as it can aid in understanding the forces that contribute to great earthquakes. There are two prevailing ideas for the occurrence of great earthquakes. One idea holds that broad scale forces lead to variations in normal stress and changes in seismic coupling through the frictional resistance at the subducting plate (Scholz and Campos, 1995). Alternatively, the varying properties within the fault zone may give rise to variations in coupling. It is thought that both likely give rise to variations in seismic coupling as opposed to one solely explaining the occurence of great earthquakes. Whatever the origin of earthquakes, any model needs to explain the end-member cases of the Marianas and Chile subduction zones. The Marianas-style subduction zones are the least seismically coupled, while the Chile subduction zone is more coupled (Uyeda and Kanamori, 1979). The degree to which subduction zones are mechanically coupled remains uncertain.

Broad-scale forces of plate tectonics (e.g. normal force at plate boundaries, along with the bending force in the hinge zone) may control the variations in the occurrence of great earthquakes. Earlier, Ruff and Kanamori, 1983a suggested that there was a relationship between the occurrence of great earthquakes and the broad scale forces in an subduction zone. This relationship suggests that great earthquakes are more likely to occur at subduction zones that have large stresses caused by young plates converging at a high rate. However, the relationship between plate motions, plate age and large earthquakes of Ruff and Kanamori, 1983b has been undermined with recent seismic activity such as the 2004 Sumatra earthquake (Stein and Okal, 2007). Still, the idea that such broader forces play an important role has considerable merit as subduction zones show substantially different dynamics that are potentially governed by plate age, dip, depth, and stress distribution.

As we develop an understanding of the relationship between large magnitude earthquakes and where they occur, the tectonic stress distribution along plate boundaries needs to be considered. Existing studies use simple fluid dynamics in 2-D to estimate the normal forces acting on the slab (Scholz and Campos, 1995; Conrad, Bilek, et al., 2004; Scholz and Campos, 2012). Such studies approximate the Stokes flow in the mantle in a subduction-by-subduction zone basis, that is computing the broad-scale forces (similar to Fig.1.1) such as the drag-force which is approximated as the force under an ellipsoid in a viscous fluid. Under this balance of broad-scale forces, the change in normal stress at plate boundaries is computed and a relationship between the reduction of normal force and seismic coupling is advanced. In a similar vein, broad-scale forces were estimated along with the state of stress for major subduction zones in a simple Stokes flow model Conrad, Bilek, et al., 2004, they found that slabs that are nearly detached from plates tend to produce great earthquakes (Conrad, Bilek, et al., 2004). While the conclusions between great earthquakes, seismic coupling and broad-scale forces are noteworthy those studies fall short because the dynamics, (dislocation creep, yielding and large variations in effective viscosity), that occur on a broad-scale are more complex than represented in those elementary calculations (Conrad, Bilek, et al., 2004; Scholz and Campos, 2012). For example, although there is broad-scale flow in the global models of Conrad, Bilek, et al., 2004, in reality there is no curving bending plates in subduction zones. In the Scholz and Campos, 2012 models, although there are falling Stokes spheres, there again are no slabs that act as stress guides from the interior of the surface.

While, the broad-scale forces are important on a geological timescale, what happens on the shorter timescale in the fault zone is traditionally described by rate and state frictional laws (Ruina, 1983). Typically, the fault zone is undergoing creep and the more coupled part of the fault zone displays stick-slip motion behavior (Scholz and Campos, 2012). When there is unstable sliding, the motion of the fault-zone becomes pure stick-slip resulting in a large seismic coupling (Ruina, 1983; Scholz and Campos, 1995) and thus great earthquakes. In contrast to broad scale forces, seismic coupling may be attributed to subduction zone properties in the fault zone. There are potential underlying causes that suggest different properties give rise to strongly coupled subduction zones. A few possibilities as to why certain subduction zones are more seismically coupled than others include the accretion of sediments and the subduction of seamounts. The amount of sediments at each subduction zone could give rise to a larger shear force; however, sediments may primarily control the stick-slip nature of the plate interface and may not be responsible for increased mechanical coupling over long time scales. Furthermore, it has been argued that subducted seamounts would increase the friction in the faults (Geersen et al., 2015). Consequently, the exact influence each of these subduction zone properties has on seismic coupling.

Ultimately, the occurrence of great earthquakes and the state of stress between plates and indeed plate motions are governed by the mechanical properties of the mantle and plates. Correctly describing the constitutive relationship of mantle viscosity is essential in producing accurate models consistent with plate motions. The strength of slabs plays a key role in how fast plates move. Creep of mantle minerals is thermally activated and governed by an Arrhenius relation and in the upper mantle, dislocation creep is the dominant mechanism that gives rise to a power law rheology, i.e. non-Newtonian viscosity. In the lower mantle, diffusion creep (movement of defects in a crystalline lattice), may be the predominant mechanism giving rise to a Newtonian viscosity. Therefore, an appropriate viscosity must take into account the dominance of dislocation and diffusion creep occurring in the upper and lower mantle, respectively (Karato and Wu, 1993).

There have been numerous studies (Zhong, 2001) that have used a temperature dependent Newtonian viscosity but they generally do not predict plate motions well. However, the use of a non-Newtonian viscosity is more appropriate in the upper mantle since there there is substantial strain-rate weakening in mantle rocks due to dislocation creep (Karato and Wu, 1993). Furthermore, a more realistic rheology needs to account for the dynamic weakening that occurs as plates bend, in which dynamic weakening is controlled by an effective yield stress (Billen and Hirth, 2005; Billen and Hirth, 2007; Stadler et al., 2010; Buffett and Becker, 2012). The yield stress reduces the viscosity in the hinge zone which allows the slab to overcome the bending force and subduct into the mantle. Similar to the activation energy and strain rate exponent, a small yield stress weakens the slab

The desired resolution needed in a flow model influences whether a 2D or 3D domain is used. While a 3-D spherical flow model has the benefit of capturing poloidal (convergence or divergence) and toroidal motion (strike-slip), those models can be expensive and therefore may not properly resolve the thermal boundary layers, slabs and plate margins and were avoided for many years. Consequently, much of the dynamics has been studied in 2-D which was computationally tractable. Using a 2D domain can significantly reduce the computational cost while also allowing for a significant increase in resolution compared to models computed in a 3D domain. Furthermore, the reduced computational cost of 2D problems enables one to use non-Newtonian rheologies (Billen and Hirth, 2005; Billen and Hirth, 2007) where the complex dynamics can be fully explored. However, these 2D approximations do not include both toroidal and poloidal flow which can be key depending on what region of the earth is modeled. Therefore, a 3D domain should be used when one needs to capture the complex flow in the mantle. Previous spherical models can be classified into two approaches: a torque-balance approach or a solving the Stokes flow problem where the forces are a natural dynamic outcome. Models of the torque-balance approach (Forte and Peltier, 1991) are able to constrain the surface observables such as plate motion and dynamic topography; however, they fall short of incorporating the salient aspects of the rheology and lateral variations in viscosity.

The second approach is where the forces are solved through the full solution of the Stokes flow with lateral variations in viscosity; however, there was always a misfit between model results and observations (Ghosh et al., 2010). However, with the use of adaptive mesh refinement (AMR), there have been spherical models that incorporate non-Newtonian rheology along with fine-scale resolution of fault zones and slabs (Stadler et al., 2010) which can produce the complex motions of both large-scale and micro plates. While those spherical models were the first accurately modeled models for plate motion and mantle flow, they were computationally expensive.

Unfortunately, the strain rate exponent, yield stress and activation energy governing plate motions and mantle flow are poorly constrained. To remedy this situation, an optimization problem could be used to minimizing a misfit in surface data that is constrained by Stokes flow. Unfortunately, optimization problems that minimize the misfit in surface data only specify a single set of optimal parameters consistent with observed data but does not provide estimates of the uncertainty. A better approach for inferring parameters is through a Bayesian framework as it incorporates data uncertainty and a prior distribution for each inferred rheological parameter, while providing the covariance matrix for the inferred parameters (Tarantola, 2002). A common method for solving Bayesian inverse problems is to use sampling methods such as Markov Chain Monte Carlo (MCMC), where the parameter space is explored using an acceptance-rejection proposal (Tarantola, 2002). However, MCMC can be expensive if the parameter space is large or the forward model is expensive (Baumann et al., 2014).

An important aspect in these uncertainty quantification problems is the data. We will mostly use plate motion data (Argus and Gordon, 1991; Argus, Gordon, and DeMets, 2011), which assumes that plates are rigid, that is they have negligible strain. In our studies, we will make use of the MORVEL56-NNR plate motion data (Argus, Gordon, and DeMets, 2011), which contains plate motion data for all 56 (major and minor) plates. However, an assumption of this plate motion model is that it assumes a no-net rotation reference frame.

Another option for parameter inference is to assume a form of the posterior density of the inferred parameters. Typically, the posterior density is assumed to be a normal distribution, however to find the mean and the covariance of a parameter distribution, an optimization problem needs to be solved through minimizing a misfit between a model outcome and observed data. The normal distribution approximation is a good approximation to first order to the true posterior distribution around the maximum a posteriori (MAP) point (Petra and Stadler, 2011). However, the normal approximation is less accurate away from the MAP point as the true posterior distribution is more non-Gaussian.

Since mantle viscosity is nonlinear, the true posterior distribution of the rheological properties of the mantle would be expected to have some degree of nonlinearity (not normal). However, constructing the accurate posterior distribution is difficult in a spherical model with appropriate resolution because it requires repeat forward solutions, which is expensive. We will show, however, that the Gaussian approximation is reasonable in Chapter 2, as it is a first-order approximation for the conditional distributions for each inferred parameter and therefore is a viable means to provide a high-probability estimate of the inferred parameters.

Building a posterior distribution for the rheological parameters provides the range of possible values each rheological value can take in addition to the correlations among parameters. The highest probability of a posterior distribution can accurately quantify forces that occur at plate boundaries. Therefore, capturing the true posterior distribution is not necessary because the high probability regions exist near the MAP point which can be cheaply approximated by a Gaussian distribution. Using this Gaussian approximation of the inferred parameters, the Gaussian approximation of the posterior shear and normal stresses between plates can be computed. The posterior distributions for the shear and normal stresses would provide a physical interpretation of the degree of coupling between subduction zones and where great earthquakes occur.

In this thesis, we will develop a Bayesian Uncertainty Quantification approach to infer the rheological parameters in models using a rheology that captures the nonlinear flow of the mantle, with realistic thermal distribution of plates and slabs along with an accurate representation of the fault zone, which has not been done before. This method will combine the use of both accurate models (non-Newtonian rheology and realistic thermal distribution and fault zones), while constraining plate motions to infer the rheological parameters using adjoints–a first in the field of geodynamics. Furthermore, we quantify the uncertainty in the poorly constrained constitutive parameters as well as forces at plate boundaries while honoring the complexities of the geometry of slabs and fault zones. In Chapter 2, we will derive the adjoint equations and demonstrate how to appropriately sample surface data to avoid spurious results for 2D models. We will show the sensitivity of plate coupling to surface velocity. In Chapter 3, we will look at surface normal stress as data and likewise derive the gradients and the forcing terms for the adjoint system. We will then present some examples to show proof of concept and discuss limitations of this method. In Chapter 4, we introduce average effective viscosity data for certain regions in the upper mantle. Furthermore, we will derive the adjoint system for both plate velocity and effective viscosity and present examples using realistic temperature and velocity data. Additionally, we will derive expressions for the covariance of plate boundary stresses in addition to comparing the stress (normal and tangential) conditional distributions between plate margins, which has not been explored in geodynamics. In Chapter 5, we will discuss ideas that builds upon the work completed in this thesis.

Chapter 2

ADJOINT-BASED ESTIMATION OF PLATE COUPLING IN A NON-LINEAR MANTLE FLOW MODEL: THEORY AND EXAMPLES

ABSTRACT

We develop and validate a systematic approach to infer plate boundary strength and rheological parameters in models of mantle flow from surface velocity observations. Based on a realistic rheological model that includes yielding and strain rate weakening from dislocation creep, we formulate the inverse problem in a Bayesian inference framework. To study the distribution of parameters that are consistent with the observations, we compute the maximum a posteriori (MAP) point, Gaussian approximations of the parameter distribution around that MAP point, and employ Markov Chain Monte Carlo (MCMC) sampling methods. The computation of the MAP point and the Gaussian approximation require first and second derivatives of an objective function subject to nonlinear Stokes equations; these derivatives are computed efficiently using adjoint Stokes equations. We set up two-dimensional numerical experiments with many of the elements expected in a global geophysical inversion. This setup incorporates three subduction zones with slab and weak zone (interplate fault) geometry consistent with average seismic characteristics. With these experiments, we demonstrate that when the temperature field is known, we can recover the strength of plate boundaries, the yield stress and strain rate exponent in the upper mantle. When the number of uncertain parameters increases, there are tradeoffs between the inferred parameters. These tradeoffs depend on how well the observational data represents the surface velocities, and on the weakness of plate boundaries. As the plate boundary coupling drops below a threshold, the uncertainty of the inferred parameters increases due to insensitivity of plate motion to plate coupling. Comparing the tradeoffs between inferred rheological parameters found from the Gaussian approximation of the parameter distribution and from MCMC sampling, we conclude that the Gaussian approximation—which is significantly cheaper to compute—is often a good approximation, in particular locally around the MAP point. Thus, the method can be applied to the global problem of inferring nonlinear constitutive parameters and plate coupling factors for each subduction zone in a global geophysical inversion with known slab structure.

2.1 Introduction

Plate motion is likely primarily driven by slab pull, the concentration of negative buoyancy from subducted oceanic plates at convergent margins (Forsyth and Uyeda, 1975; Chapple and Tullis, 1977), while other driving forces, including ridge push and traction at the base of plates, also contribute. Although estimates of slab pull suggest that it may be responsible for more than about 70% of the total driving force (Conrad and Lithgow-Bertelloni, 2002), the relative strength of forces controlling plate motion has been difficult to firmly establish because of the diverse origin of driving mechanisms and the close association between slab pull and resisting forces. The slab pull force arises from concentration of negative buoyancy and through thermally activated mantle rheology leads to a larger effective strength of slabs. Slabs both concentrate the driving force (because they act as stress guides (Elsasser, 1969)) and concentrate resistance (because the relatively strong slabs bend in the hinge zone (Conrad and Hager, 1999)). There is a significant effect from dynamic weakening at plate boundaries manifested as the development of normal faulting and diffuse seismicity in the outer rise associated with plate bending (Kikuchi and Kanamori, 1995). Presumably, as plates are underthrusted at plate boundaries, there is a large stress concentration within the hinge zone leading to the growth of faults which dissipates energy and weakens the plate. Slabs are a fundamental, highly nonlinear component of the system of plate forces, but deconvolving these forces and quantifying uncertainty has been difficult, especially in global models meant to predict and explain actual plate motions.

At convergent plate boundaries, in addition to plate bending, the resistance to plate motion is also likely strongly influenced by sliding of subducting with respect to over-riding plates. Such motion gives rise to great earthquakes that occur along many, but not all, subduction zones. Seismic coupling (ratio of seismic moment release to the rate implied by plate motion) varies substantially between subduction zones. Variation in seismic coupling is likely strongly influenced tectonically, that is by local convergence, plate age, and the geometry of both the shallow and deep structure of slabs (Ruff and Kanamori, 1983b). Seismic coupling could also be influenced by the nature of the material (such as the thickness of the sediment on the incoming plate (Ruff, 1989)) within the zone between the plates. Such quantities vary substantially not only between subduction zones but also along strike of a plate boundary. A simple heuristic model suggests that highly coupled subduction zones (such as Peru or Chile) may have large normal forces, while weakly coupled subduction zones (such as the Marianas or the Izu-Bonin) have small normal forces

(Scholz and Campos, 1995; Scholz and Campos, 2012).

The importance of driving and resisting forces has been evaluated with forward and inverse models (Hager and O'Connell, 1981; Forte and Peltier, 1987; Conrad and Lithgow-Bertelloni, 2002). Some spherical models essentially invert observed plate motions for the radial viscosity of the mantle while being driven by the long-wavelength distribution of mantle buoyancy (Forte and Peltier, 1987). The models balance stresses from piecewise rigid plates (spherical caps) against the resistance from viscous linear mantle flow with small lateral variations in viscosity.

Such spherical inversions do not include the essential character of slabs which act as stress guides while resisting plate motions through plate bending. By incorporating constitutive relationships with thermally activated diffusion and dislocation creep (Karato and Wu, 1993) with yielding, regional 2-D (Billen and Hirth, 2005; Billen and Hirth, 2007) and 3-D Cartesian models (Zhong, Gurnis, and Moresi, 1998) capture the potentially relevant processes within the bending plate while producing plate-like surface motion. Such models require high resolution locally ($\sim$ 1 km), especially within the hinge zone of the subducting plates, and robust Stokes solvers that can handle the many orders of magnitude variations in effective viscosity implied by laboratory-based constitutive relationships (variations can be six to eight orders of magnitude). The ability to incorporate these resolutions and solvers in spherical models capable of achieving global plate motions has been a computational challenge, and only recently overcome (Stadler et al., 2010). Through adaptive mesh refinement, the sharp gradients in viscosity within and near slabs have been achieved in instantaneous models that forward predict global plate motions (Alisic, Gurnis, Stadler, Burstedde, and Ghattas, 2012; Alisic, Gurnis, Stadler, Burstedde, Wilcox, et al., 2010). Such models are also able to show finer scale tectonic motions, such as rapid trench rollback, while not requiring plates to be rigid. As such forward models only approximately matched observed plate motions, their full potential has yet to be achieved.

There has been important progress developing inverse models of mantle flow that bring different sets of data together toward the inference of geophysical properties. For example, adjoints have been implemented with different combinations of the convection equations to infer the initial temperature distribution in the mantle in both regional (Ismail-Zadeh et al., 2004; Spasojevic et al., 2009) and global (Bunge et al., 2003; Horbach et al., 2014) contexts. Nevertheless, all of these models use simplified rheologies that do not incorporate the essential physics of strain rate weakening and yielding that are arguably essential for computing the driving and resisting forces of plate motions.

Here we explore how the high resolution flow models can be recast as an inverse problem capable of resolving the complex role of slabs and plate margins. We develop a method to infer plate boundary strength, yield stress and strain rate exponent by fitting plate motions in high-resolution models in which slabs and hinge zones are well resolved. We expand on the work of Worthen et al. (2014) in three ways. First, the test problems employed here are functionally equivalent to the expected geophysical inverse problem. Second, we formulate the problem as a Bayesian inverse problem, which allows a more complete characterization of the physical tradeoffs and the uncertainties in the inferred parameters. Third, we provide expressions for the second derivatives (the Hessian matrix) of the mismatch functional between the geophysical observations and model predictions. For that purpose, we derive the first-order adjoint equations along with the expression of the gradient of this misfit functional with respect to the parameters. A Bayesian formulation of the inverse problem allows us to quantify uncertainties in the inferred parameters in addition to computing the best-fit, i.e., maximum a posteriori (MAP), parameters. The computation of the MAP estimate amounts to solving a PDE-constrained optimization problem, for which we employ an inexact Newton conjugate gradient method. To estimate the uncertainty in these parameters we explore their posterior distribution, that is, the solution of the Bayesian inverse problem. We compare results obtained from sampling the posterior distribution with its Gaussian approximation centered at the MAP parameters. With a series of computations of a 2-D model problem, we demonstrate the tradeoffs between the mechanical properties that occur in the system. We demonstrate that the Gaussian approximation of the a posteriori distribution is a reasonable approximation of the posterior distribution near the MAP point. We then discuss issues associated with applying the methods to the spherical global mantle flow problem to infer of the parameters in the nonlinear constitutive relationship and the spatial distribution of plate coupling from present day plate motions.

2.2 Nonlinear Stokes Forward Problem

We model mantle flow with the infinite Prandtl-number Boussinesq approximation, which leads to the following non-dimensional Stokes equations:

$$\nabla \cdot \boldsymbol{\sigma} = -\mathrm{Ra}\, T \mathbf{e_r} \qquad \text{on } \Omega, \tag{2.1a}$$

$$\nabla \cdot \boldsymbol{u} = 0 \qquad \text{on } \Omega, \tag{2.1b}$$

where Ω is the mantle domain (assumed to be two-dimensional in this paper), $\boldsymbol{\sigma} = \boldsymbol{\sigma}(\boldsymbol{u}, p) = 2\eta\dot{\boldsymbol{\varepsilon}}(\boldsymbol{u}) - p\mathbf{I}$ is the stress tensor with the viscosity $\eta = \eta(\dot{\varepsilon}_{\mathrm{II}}, \Gamma, T, \sigma_y)$, which depends on the velocity $\boldsymbol{u}$ (through the second invariant of the strain tensor $\dot{\varepsilon}_{\mathrm{II}}$ defined below), on multiplicative factor Γ modelling plate boundaries, on the temperature T and on the yield stress $\sigma_y > 0$. Moreover, $\dot{\boldsymbol{\varepsilon}}(\boldsymbol{u}) := \frac{1}{2}(\nabla \boldsymbol{u} + \nabla \boldsymbol{u}^T)$ is the strain rate tensor, p is the pressure and $\mathbf{I}$ the identity tensor. The Stokes equations (2.1) are driven by thermal buoyancy. Here, $\mathrm{Ra} = \frac{\rho g \alpha \Delta T D^3}{\kappa \eta_{\mathrm{ref}}}$ is the thermal Rayleigh number, where ρ is the density of the mantle, g is the gravitational acceleration, α is the thermal diffusivity, ΔT is the temperature difference, D is the length scale, η_{ref} is the reference viscosity, and κ is the thermal diffusivity. The second invariant of the strain rate tensor is $\dot{\varepsilon}_{\mathrm{II}} = \frac{1}{2}[\mathrm{tr}(\dot{\boldsymbol{\varepsilon}}^2(\boldsymbol{u})) - \mathrm{tr}(\dot{\boldsymbol{\varepsilon}}(\boldsymbol{u}))]$. In the limit of incompressibility considered here, $\dot{\varepsilon}_{\mathrm{II}}$ reduces to

$$\dot{\varepsilon}_{\mathrm{II}} = \frac{1}{2}\mathrm{tr}(\dot{\boldsymbol{\varepsilon}}^2(\boldsymbol{u})). \tag{2.2}$$

Note that, in the geophysics literature sometimes the square root of $\dot{\varepsilon}_{\mathrm{II}}$ is referred to as the second invariant of the strain rate tensor. No normal flow and free-slip tangential conditions on the boundary $\partial\Omega$ of Ω are used, i.e.,

$$\boldsymbol{u} \cdot \mathbf{n} = 0, \ \mathbf{T}(\boldsymbol{\sigma}\mathbf{n}) = 0. \qquad \text{on } \partial\Omega \tag{2.3}$$

Here, we use the tangential operator for the Neumann condition defined as $\mathbf{T} = \mathbf{I} - \mathbf{n}\mathbf{n}^T$ is the projection onto the tangential direction. In particular, plate velocities on the top are not imposed but are an outcome of model calculations.

In the following, we prefer to work with the weak (variational) form of the Stokes equations (2.1). This weak form is derived by multiplying (2.1a) and (2.1b) by arbitrary functions $\boldsymbol{v}$ and q, respectively, which are assumed to be sufficiently smooth, and satisfy the equivalent Dirichlet boundary condition, $\boldsymbol{v} \cdot \mathbf{n} = 0$. Using integration by parts and the boundary conditions (2.3), this results in

$$\int_\Omega 2\eta(\dot{\varepsilon}_{\mathrm{II}}, \Gamma, n, \sigma_y)\dot{\boldsymbol{\varepsilon}}(\boldsymbol{u}) : \dot{\boldsymbol{\varepsilon}}(\boldsymbol{v}) d\Omega - \int_\Omega p \nabla \cdot \boldsymbol{v} d\Omega - \int_\Omega q \nabla \cdot \boldsymbol{u} d\Omega = \int_\Omega \mathrm{Ra} T \mathbf{e}_r \cdot \boldsymbol{v} d\Omega. \tag{2.4}$$

On geological time scales, the mantle behaves like a viscous fluid from thermally activated creep. The viscosity strongly depends on temperature, and this dependence can be represented by an Arrhenius-type law. In the upper mantle, dislocation creep likely dominates over diffusion creep (Stocker and Ashby, 1973). Although one can prescribe the rheology as composite (Billen and Hirth, 2007; Stadler et al., 2010) such that both, diffusion and dislocation creep can play a role depending on the state of stress and the strain rate, we have found that dislocation creep dominates within the plates and slabs and hence is the deformation mechanism which likely controls plate motions. Thus, underlying our models is a temperature-dependent shear-thinning rheology,

$$\tilde{\eta}(\dot{\varepsilon}_{\mathrm{II}}, T) = \Gamma a(T) \dot{\varepsilon}_{\mathrm{II}}^{\frac{1-n}{2n}}, \text{ with } \Gamma(x) = 1 - \sum_i (1 - \Gamma_i) \chi_i(x),$$

where $a(T) := \mathrm{A}_{\mathrm{rad}} \exp(\beta(0.5 - T))$, and $\chi_i(\cdot)$ are characteristic functions for individual plate boundaries, i.e., a function with value 1 at the (volumetrically modeled) plate boundary, and a value of 0 away from the plate boundary. The strength/weakness of the coupling along plate boundaries is controlled by the weakening factors $\Gamma_i > 0$. Plate decoupling occurs over long time scales within seismogenic zones, where great earthquakes typically occur. The degree of frictional resistance that occurs along the seismogenic zone is controlled by the factors Γ_i: small values of Γ_i give rise to weakly coupled plate boundaries, while larger values enforce stronger coupling. Plate boundaries require high spatial resolution in computational models, and the coupling factors Γ_i will act as parameters in the inversion.

An important aspect of the mantle rheology is dynamic weakening through shear thinning, in particular near hinge zones. Thus, we use a rheology that involves plastic yielding additionally to polynomial shear thinning. For computational reasons we also incorporate lower and upper viscosity bounds $0 < \eta_{\min} < \eta_{\max}$ in the rheology, such that the (effective) viscosity is

$$\eta(\dot{\varepsilon}_{\mathrm{II}}, \Gamma, n, \sigma_y) = \eta_{\min} + \min(\Gamma \min(\eta_{\max}, a(T)(\dot{\varepsilon}_{\mathrm{II}} - d)^{\frac{1}{2n}} \dot{\varepsilon}_{\mathrm{II}}^{-\frac{1}{2}}), \frac{1}{2}\sigma_y \dot{\varepsilon}_{\mathrm{II}}^{-\frac{1}{2}}). \quad (2.5)$$

Here, roots of negative quantities are considered to be zero; they do not play a role due to the viscosity bounds. The choice (2.5) for the effective viscosity corresponds to first applying the upper viscosity bound to the temperature and strain rate dependent viscosity. This is followed by the multiplication with $\Gamma(x)$, a function describing plate boundaries through low viscosity zones. Finally, the plastic yielding condition is imposed. Adding $\eta_{\min}$ enforces a lower bound on the viscosity, as well as a one-to-one correspondence between strain rate and stress in the case of plastic yielding. In (2.5), we use a shift $d \geq 0$—which is derived in Appendix .1—to ensure that $\eta_{\max}$ is incorporated in a way that the viscosity is continuously differentiable with respect to $\dot{\varepsilon}_{\mathrm{II}}$, and thus also with respect to the velocity. This differentiability is important as we target Newton-type methods for the solution of the nonlinear Stokes equations and also require derivatives in the inversion. Note however, that the continuous differentiability of the viscosity with respect to $\dot{\varepsilon}_{\mathrm{II}}$ does not hold when plastic yielding occurs.

There exists several areas in the mantle where dynamic weakening or the viscosity bounds are important. For instance, the condition $\eta_{\max} < \eta(\dot{\varepsilon}_{\mathrm{II}}, \Gamma, T, \sigma_y)$ primarily holds in the oceanic lithosphere where strain rate weakening plays a secondary role and the viscosity structure is dominated by the temperature. There are two possible cases: (i) the effective viscosity is $\eta_{\max} + \eta_{\min}$, if $\eta_{\max}$ is smaller than the yielding viscosity or, (ii) $\eta_{\mathrm{eff}} = \frac{1}{2}\sigma_y \dot{\varepsilon}_{\mathrm{II}}^{-1/2} + \eta_{\min}$, i.e., yielding occurs. While $\eta_{\max}$ is dominant in the lithosphere, in the asthenosphere the viscosity is primarily dominated by dislocation creep, i.e., $\eta(\dot{\varepsilon}_{\mathrm{II}}, \Gamma, T, \sigma_y) < \eta_{\max}$.

An important characterization of the system state, both within subduction zones and the whole model domain, is the viscous dissipation in a subdomain $\tilde{\Omega} \subset \Omega$ of interest given by

$$\Phi(\tilde{\Omega}) = \int_{\tilde{\Omega}} 2\eta(\dot{\varepsilon}_{\mathrm{II}}, \Gamma, n, \sigma_y)\dot{\boldsymbol{\varepsilon}}(\boldsymbol{u}) : \dot{\boldsymbol{\varepsilon}}(\boldsymbol{u}) d\tilde{\Omega}. \tag{2.6}$$

Viscous dissipation has been analyzed in models of subduction zones and related to the bending of plates (Conrad and Hager, 1999): as plates bend at subduction zones, a large amount of energy associated with dynamic weakening is released.

2.3 Bayesian inversion

A Bayesian approach to inverse problems allows one to infer the most likely parameters together with their uncertainties from a computational model, observational data, and prior knowledge on the parameters. In our problem, the parameters to be inferred are the plate coupling strength coefficients Γ_i and rheological parameters; the observational data are the observed plate velocities, and prior knowledge on the parameters can come, e.g., from laboratory experiments or inferences from other geophysical observations. The computational model describes our theory of how parameters and observations are related. In our case, this relation is given through the solution of the nonlinear Stokes equations discussed in Section 2.2. We collect all parameters in a vector $\boldsymbol{m} \in \mathbb{R}^p$, collect the plate velocity observations in a vector $\boldsymbol{u}_{\text{obs}}$, and denote the mathematical model that maps parameters to plate velocities by $\boldsymbol{f}(\boldsymbol{m})$. Note that for given parameters $\boldsymbol{m}$, the computation of $\boldsymbol{f}(\boldsymbol{m})$ is computationally costly, as it requires the solution of nonlinear Stokes equations, followed by extracting the corresponding plate velocities from the velocity field data. Additionally, even if the involved Stokes operator were linear, the parameter-to-observable map $\boldsymbol{f}(\cdot)$ is nonlinear as the Stokes flow depends nonlinearly on rheological parameters.

In our Bayesian inversion approach, we assume that observation and model errors follow a Gaussian distribution with zero mean and covariance matrix C_{noise}, i.e.,

$$\boldsymbol{f}(\boldsymbol{m}) - \boldsymbol{u}_{\text{obs}} = \mathcal{N}(0, C_{\text{noise}}).$$

Thus, the likelihood probability density function (pdf), which describes the likelihood of observations $\boldsymbol{u}_{\text{obs}}$ for given model parameters $\boldsymbol{m}$ is given by

$$\boldsymbol{\pi}_{\text{like}}(\boldsymbol{u}_{\text{obs}}|\boldsymbol{m}) \propto \exp\left(-\frac{1}{2}(\boldsymbol{f}(\boldsymbol{m}) - \boldsymbol{u}_{\text{obs}})^T C_{\text{noise}}^{-1}(\boldsymbol{f}(\boldsymbol{m}) - \boldsymbol{u}_{\text{obs}})\right),$$

where "$\propto$" denotes proportionality up to a (normalization) constant that makes $\boldsymbol{\pi}_{\text{like}}$ a proper density. Additionally, we assume a given prior pdf $\boldsymbol{\pi}_{\text{prior}}(\boldsymbol{m})$, which incorporates our prior knowledge on the parameters. Bayes' theorem states that the posterior probability distribution $\boldsymbol{\pi}_{\text{post}}(\boldsymbol{m})$, which is the solution of the Bayesian inverse problem, is given by (Tarantola, 2005; Kaipio and Somersalo, 2005)

$$\boldsymbol{\pi}_{\text{post}}(\boldsymbol{m}) \propto \boldsymbol{\pi}_{\text{like}}(\boldsymbol{u}_{\text{obs}}|\boldsymbol{m})\boldsymbol{\pi}_{\text{prior}}(\boldsymbol{m}). \tag{2.7}$$

Even if the prior is Gaussian, say with mean $\boldsymbol{m}_0$ and covariance matrix C_{prior}, i.e.,

$$\boldsymbol{\pi}_{\text{prior}}(\boldsymbol{m}) \propto \exp\left(-\frac{1}{2}(\boldsymbol{m} - \boldsymbol{m}_0)^T C_{\text{prior}}^{-1}(\boldsymbol{m} - \boldsymbol{m}_0)\right), \tag{2.8}$$

the posterior pdf given by (2.7) is, in general, non-Gaussian due to the nonlinearity of the parameter-to-observable map. Statistical estimators to explore and characterize the posterior pdf $\boldsymbol{\pi}_{\text{post}}$—and thus the solution of the Bayesian inverse problem—are discussed next.

Exploring the posterior distribution

Important statistical estimators for a distribution are the *maximum a posteriori (MAP)* point, the *mean* and the *covariance matrix*. We next briefly discuss these estimators and their approximations. For simplicity of the presentation, we assume a Gaussian prior given by (2.8), such that the posterior pdf has the form

$$\boldsymbol{\pi}_{\text{post}}(\boldsymbol{m}) \propto \exp(-\frac{1}{2}(\boldsymbol{f}(\boldsymbol{m})-\boldsymbol{u}_{\text{obs}})^T C_{\text{noise}}^{-1}(\boldsymbol{f}(\boldsymbol{m})-\boldsymbol{u}_{\text{obs}})-\frac{1}{2}(\boldsymbol{m}-\boldsymbol{m}_0)^T C_{\text{prior}}^{-1}(\boldsymbol{m}-\boldsymbol{m}_0)). \tag{2.9}$$

The parameter vector $\boldsymbol{m}$, where $\boldsymbol{\pi}_{\text{post}}$ takes its maximum is called the maximum a posteriori (MAP) point, $\boldsymbol{m}_{\text{MAP}}$. It can be found by maximizing $\boldsymbol{\pi}_{\text{post}}$, or equivalently, by minimizing the negative log of the posterior pdf, i.e.,

$$\min_{\boldsymbol{m}\in\mathbb{R}^p} \mathcal{J}(\boldsymbol{m}), \tag{2.10}$$

where

$$\mathcal{J}(\boldsymbol{m}) := \frac{1}{2}(\boldsymbol{f}(\boldsymbol{m}) - \boldsymbol{u}_{\text{obs}})^T C_{\text{noise}}^{-1}(\boldsymbol{f}(\boldsymbol{m}) - \boldsymbol{u}_{\text{obs}}) + \frac{1}{2}(\boldsymbol{m} - \boldsymbol{m}_0)^T C_{\text{prior}}^{-1}(\boldsymbol{m} - \boldsymbol{m}_0). \tag{2.11}$$

This problem has the form of the regularized least squares optimization problem occurring in deterministic inverse problems, with the term coming from the prior corresponding to the regularization used to cope with the ill-posedness common to inverse problems (Vogel, 2002; Tarantola, 2005). Effective minimization of (2.11) requires computation of derivatives of $\mathcal{J}$ with respect to the parameters $\boldsymbol{m}$. The computation of these derivatives is complicated by the fact that the parameter-to-observable map involves the solution of a partial differential equation. We use adjoint equations to make this computation efficient (see Section 2.3). Building on these derivatives, we use a Newton method for the solution of (2.10): Starting from an initial guess $\boldsymbol{m}^0$ for the parameters, for $k = 1, \ldots$ one computes a Newton update direction $\bar{\boldsymbol{m}}$ by solving

$$\mathcal{H}(\boldsymbol{m}^k)\bar{\boldsymbol{m}} = -\mathcal{G}(\boldsymbol{m}^k) \tag{2.12a}$$

and updates

$$\boldsymbol{m}^{k+1} = \boldsymbol{m}^k + \alpha\bar{\boldsymbol{m}}, \tag{2.12b}$$

where $\mathcal{G}$ and $\mathcal{H}$ denote the gradient and the Hessian with respect to $\boldsymbol{m}$, respectively. In (2.12a), $\alpha > 0$ is a step length, which is, starting from an initial step length of $\alpha = 1$ reduced using backtracking to ensure descent of the negative log likelihood $\mathcal{J}(\cdot)$ from the kth to the $(k + 1)$st iteration; see Nocedal and Wright (2006).

To explore the posterior pdf beyond the MAP estimate—and thus quantify the uncertainty in the parameter estimates—one can either characterize the posterior through sample statistics or construct an approximation to $\boldsymbol{\pi}_{\text{post}}$. We use both of these approaches and compare the results and their computational efficiency.

Sampling methods (Hastings, 1970; Gilks, 2005) allow the complete characterization of $\boldsymbol{\pi}_{\text{post}}$, but they often require a large number of evaluations of $\boldsymbol{f}(\boldsymbol{m})$, i.e., many nonlinear Stokes solves for different parameters. Sampling is particularly challenging for high-dimensional parameter vectors $\boldsymbol{m}$, as the posterior pdf is defined over a space of the dimension of the parameter vector; this difficulty for high-dimensional distributions is often referred to as *curse of dimensionality* (Tarantola, 2002; Tarantola, 2005).

An alternative to sampling is to construct a Gaussian approximation of $\boldsymbol{\pi}_{\text{post}}$, centered at the MAP point. For that purpose, we consider the linearization $\boldsymbol{F}$ of the parameter-to-observable map $\boldsymbol{f}(\cdot)$ at the MAP estimate $\boldsymbol{m}_{\text{MAP}}$:

$$\boldsymbol{f}(\boldsymbol{m}) \approx \boldsymbol{f}(\boldsymbol{m}_{\text{MAP}}) + \boldsymbol{F}(\boldsymbol{m} - \boldsymbol{m}_{\text{MAP}}). \tag{2.13}$$

Using this approximation for the parameter-to-observable map in (2.9) results—after rearranging terms—in a Gaussian approximation $\boldsymbol{\pi}_{\text{post}}^{G}$ of the posterior given by

$$\boldsymbol{\pi}_{\text{post}}^{G}(\boldsymbol{m}) \quad \propto \quad \exp\left(-\frac{1}{2}(\boldsymbol{m} - \boldsymbol{m}_{\text{MAP}})^{T}\left(\boldsymbol{F}^{T}C_{\text{noise}}^{-1}\boldsymbol{F} + C_{\text{prior}}^{-1}\right)(\boldsymbol{m} - \boldsymbol{m}_{\text{MAP}})\right).$$

Note that the mean of this Gaussian approximation $\boldsymbol{\pi}_{\text{post}}^{G}$ is $\boldsymbol{m}_{\text{MAP}}$, and the covariance matrix is the inverse of $(\boldsymbol{F}^{T}C_{\text{noise}}^{-1}\boldsymbol{F} + C_{\text{prior}}^{-1})$, which is the Hessian of $\mathcal{J}$ after linearization of the parameter-to-observable map.

The computation of the MAP point and of the Gaussian approximation of the posterior about the MAP point require derivatives of the negative log posterior $\mathcal{J}(\cdot)$ with respect to the parameter vector $\boldsymbol{m}$. As $\mathcal{J}(\cdot)$ depends on the solution of the nonlinear Stokes equations, we use adjoint methods to compute these derivatives efficiently, which is the topic of the next section.

Adjoint-based computation of derivatives

Adjoint equations allow one to efficiently compute derivatives of scalar-valued functions (such as $\mathcal{J}(\cdot)$) with respect to a large number of parameters by solving a single (linear) adjoint equation. Using finite differences (or forward sensitivities) is an alternative to the use of adjoint methods, but has the disadvantage that it requires the solution of an equation for each parameter, i.e., each component of $\boldsymbol{m}$. Hence, for a large number of parameters and expensive-to-solve forward models (as the nonlinear Stokes equations (2.1)), the use of adjoint methods to compute derivatives is crucial.

We choose a parameterization for the coupling factors Γ_i, the yield stress σ_y, and the strain rate exponent n that ensures their positivity by considering their logarithms as the inference parameter vector, i.e.,

$$\boldsymbol{m} = (\log(\Gamma_1), \log(\Gamma_2), \ldots, \log(\sigma_y), \log(n))^T. \tag{2.14}$$

The parameter-to-observable map $\boldsymbol{f}(\cdot)$ maps the parameters $\boldsymbol{m}$ to the Stokes velocity $\boldsymbol{u}$ (or some linear function $\mathcal{O}\boldsymbol{u}$ of the Stokes velocity) on the top boundary $\partial\Omega_t$ of Ω. The flow velocity observations can either be pointwise field observations, or observations of the average velocity of plate-like structures. Furthermore, the operator $\mathcal{O}$ extracts the velocities at points on the surface corresponding to the physical points of the observations. The latter models the type of geophysical observations that are mostly available, in which plates are considered rigid.

Using the form of the parameter-to-observable map to specify the negative log likelihood function (2.11) in the context of our target problem results in

$$\mathcal{J}(\boldsymbol{m}) = \frac{1}{2}(\mathcal{O}\boldsymbol{u}(\boldsymbol{m}) - \boldsymbol{u}_{\text{obs}})^T C_{\text{noise}}^{-1}(\mathcal{O}\boldsymbol{u}(\boldsymbol{m}) - \boldsymbol{u}_{\text{obs}}), \tag{2.15}$$

where $\boldsymbol{u}(\boldsymbol{m})$ denotes the solution of the nonlinear Stokes equations for the parameters $\boldsymbol{m}$. The function (2.15) represents the misfit of the observed surface velocities $\boldsymbol{u}_{\text{obs}}$ with surface velocities from simulations. For simplicity of the notation, in (2.15) we neglect the quadratic contribution coming from the prior, which is simple to differentiate.

We use a Lagrangian method (Tröltzsch, 2010) to compute derivatives of $\mathcal{J}$ with respect to the parameters $\boldsymbol{m}$. For that purpose, we define a Lagrangian functional as the sum of the objective (2.15), and the weak form of the Stokes equation (2.4). In the objective, we consider $\boldsymbol{m}$ and the Stokes velocity $\boldsymbol{u}$ as independent variables and thus write $\mathcal{J}(\boldsymbol{m}, \boldsymbol{u})$ rather than $\mathcal{J}(\boldsymbol{m})$. In the weak form of the Stokes equation (2.4), the test functions $\boldsymbol{v}$ and q take the role of Lagrange multiplier functions, which satisfy adjoint equations, which will be derived below. We thus refer to the Lagrange multipliers $\boldsymbol{v}$ and q as adjoint velocity and pressure, respectively. The Lagrangian functional is defined as follows:

$$\begin{aligned}\mathcal{L}(\boldsymbol{u}, p, \boldsymbol{v}, q, \boldsymbol{m}) = \mathcal{J}(\boldsymbol{m}, \boldsymbol{u}) + &\int_\Omega 2\eta(\dot{\varepsilon}_{\mathrm{II}}, \Gamma, n, \sigma_y)\dot{\boldsymbol{\varepsilon}}(\boldsymbol{u}) : \dot{\boldsymbol{\varepsilon}}(\boldsymbol{v}) d\Omega \\ - \int_\Omega p\nabla \cdot \boldsymbol{v} d\Omega - \int_\Omega q\nabla \cdot \boldsymbol{u} d\Omega &- \int_\Omega \mathrm{Ra}T\mathbf{e}_r \cdot \boldsymbol{v} d\Omega.\end{aligned} \tag{2.16}$$

Then, the gradient $\mathcal{G}(\boldsymbol{m})$ is given by the gradient of $\mathcal{L}$ with respect to $\boldsymbol{m}$, provided all variations of the Lagrangian with respect to $(\boldsymbol{u}, p)$ and $(\boldsymbol{v}, q)$ vanish, see (Tröltzsch, 2010). Thus, we next derive expressions for $\mathcal{L}$ with respect to $\boldsymbol{m}$ and derive the equations that must be satisfied if all other variations of the Lagrangian vanish.

Taking variations of the Lagrangian with respect to $\boldsymbol{m}$ results in the following expressions for the ith component of the gradient

$$\mathcal{G}(\boldsymbol{m})_i = \int_\Omega 2\eta_{,i}(\dot{\varepsilon}_{\mathrm{II}}, \Gamma, n, \sigma_y)\dot{\boldsymbol{\varepsilon}}(\boldsymbol{u}) : \dot{\boldsymbol{\varepsilon}}(\boldsymbol{v}) d\Omega, \tag{2.17}$$

where we have used that $\eta_{,i}(\dot{\varepsilon}_{\mathrm{II}}, \Gamma, n, \sigma_y)$ denotes the derivative of the viscosity η with respect to the parameter m_i. To compute derivatives of η with respect to m_i, we distinguish how the different parameters enter in the rheology. If $m_i = \log(\Gamma_i)$ is the log of the ith weak factor, this derivative is given by

$$\begin{aligned}&\eta_{,i}(\dot{\varepsilon}_{\mathrm{II}}, \Gamma, n, \sigma_y) \\ &\quad = \begin{cases} 0 & \text{in } \Omega_y, \\ \Gamma_i\chi_i \min(\eta_{\max}, a(T)(\dot{\varepsilon}_{\mathrm{II}} - d)^{\frac{1}{2n}}\dot{\varepsilon}_{\mathrm{II}}^{-\frac{1}{2}}) & \text{in } \Omega \setminus \Omega_y. \end{cases}\end{aligned}$$

where $\Gamma_i = \exp(m_i)$. Here, we denote by $\Omega_y \subset \Omega$ the points where yielding occurs, i.e., where $\eta(\dot{\varepsilon}_{\mathrm{II}}, \Gamma, n, \sigma_y) = \eta_{\min} + 1/2\sigma_y\dot{\varepsilon}_{\mathrm{II}}^{-1/2}$. At these points, the Stokes solution is not sensitive to m_i. Next, we consider the case that $m_i = \log(\sigma_y)$ and we obtain the derivative

$$\eta_{,i}(\dot{\varepsilon}_{\mathrm{II}}, \Gamma, n, \sigma_y) = \begin{cases} \frac{1}{2}\sigma_y\dot{\varepsilon}_{\mathrm{II}}^{-\frac{1}{2}} & \text{in } \Omega_y, \\ 0 & \text{in } \Omega \setminus \Omega_y. \end{cases}$$

Finally, if $m_i = \log(n)$, we obtain

$$\eta_{,i}(\dot{\varepsilon}_{\mathrm{II}}, \Gamma, n, \sigma_y) = \begin{cases} \Gamma a(T)\omega(\dot{\varepsilon}_{\mathrm{II}} - d)^{\frac{1}{2n}}\dot{\varepsilon}_{\mathrm{II}}^{-\frac{1}{2}} & \text{in } \Omega_w, \\ 0 & \text{in } \Omega \setminus \Omega_w, \end{cases}$$

where $\omega = \log((\dot{\varepsilon}_{\mathrm{II}} - d)^{-\frac{1}{2n}})$ and $\Omega_w \subset \Omega$ are the points where $\eta(\dot{\varepsilon}_{\mathrm{II}}, \Gamma, n, \sigma_y) = \eta_{\min} + a(T)(\dot{\varepsilon}_{\mathrm{II}} - d)^{1/(2n)}\dot{\varepsilon}_{\mathrm{II}}^{-1/2}$, and thus the viscosity depends on the strain rate exponent n. If we did not use the parameterization of $\log(\boldsymbol{m})$, but rather inverted for $\boldsymbol{m}$, then $\omega = \log((\dot{\varepsilon}_{\mathrm{II}} - d)^{-\frac{1}{2n^2}})$ which is similar to the procedure in Petra, Zhu, et al. (2012) and Worthen et al. (2014).

Requiring that variations of the Lagrangian with respect to the adjoint velocity and pressure $(\boldsymbol{v}, q)$ vanish is equivalent with the (weak form of) the forward Stokes equations. Setting all variations of the Lagrangian with respect to the forward velocity and pressure $(\boldsymbol{u}, p)$ to zero, and subsequent integration by parts leads to the adjoint equations, which characterize the adjoint velocity $\boldsymbol{v}$ in (2.17). These adjoint equations are given by

$$\begin{aligned} \nabla \cdot \boldsymbol{v} &= 0 \qquad \text{on } \Omega, \\ \nabla \cdot \hat{\boldsymbol{\sigma}}_{\boldsymbol{u}} &= 0 \qquad \text{on } \Omega, \end{aligned} \tag{2.18}$$

with boundary conditions

$$\begin{aligned} \boldsymbol{v} \cdot \mathbf{n} &= 0 \quad \text{on } \partial\Omega, \\ \mathbf{T}(\hat{\boldsymbol{\sigma}}_{\boldsymbol{u}}\mathbf{n}) &= \begin{cases} 0 & \text{on } \partial\Omega \setminus \partial\Omega_t, \\ -O^T C_{\text{noise}}^{-1}(O\boldsymbol{u} - \boldsymbol{u}_{\text{obs}}) & \text{on } \partial\Omega_t, \end{cases} \end{aligned}$$

where $\hat{\boldsymbol{\sigma}}_{\boldsymbol{u}} = \hat{\boldsymbol{\sigma}}_{\boldsymbol{u}}(\boldsymbol{v}, q)$ is the adjoint stress tensor defined by

$$\hat{\boldsymbol{\sigma}}_{\boldsymbol{u}} = 2\Big(\eta(\dot{\varepsilon}_{\mathrm{II}}, \Gamma, n, \sigma_y)\mathbb{I} + \frac{1}{2}\eta_{,\dot{\varepsilon}_{\mathrm{II}}}[\dot{\boldsymbol{\varepsilon}}(\boldsymbol{u}) \otimes \dot{\boldsymbol{\varepsilon}}(\boldsymbol{u})]\Big)\dot{\boldsymbol{\varepsilon}}(\boldsymbol{v}) - q\mathbf{I} \tag{2.19}$$

with $\mathbb{I}$ being the fourth-order identity tensor, and $\eta_{,\dot{\varepsilon}_{\mathrm{II}}}$ given by

$$\eta_{,\dot{\varepsilon}_{\mathrm{II}}} = \begin{cases} \min\Big(0, \Gamma a(T)(\dot{\varepsilon}_{\mathrm{II}} - d)^{\frac{1}{2n}} \dot{\varepsilon}_{\mathrm{II}}^{-\frac{1}{2}} \frac{\dot{\varepsilon}_{\mathrm{II}} - (\dot{\varepsilon}_{\mathrm{II}} - d)n}{\dot{\varepsilon}_{\mathrm{II}}(\dot{\varepsilon}_{\mathrm{II}} - d)n}\Big) & \text{in } \Omega \setminus \Omega_y \\ -\frac{1}{2}\sigma_y \dot{\varepsilon}_{\mathrm{II}}^{-\frac{3}{2}} & \text{in } \Omega_y. \end{cases} \tag{2.20}$$

Distinguishing between these two cases is necessary since the viscosity does not necessarily depend continuously on $\dot{\varepsilon}_{\mathrm{II}}$ at points where the yielding criterion is active. The anisotropic fourth-order tensor in (2.18) originates from the differentiation of the second invariant with respect to the velocity $\boldsymbol{u}$. In particular,

$$\begin{aligned} [\dot{\varepsilon}_{\mathrm{II}}]_{,\boldsymbol{u}}(\tilde{\boldsymbol{u}})\, \dot{\boldsymbol{\varepsilon}}(\boldsymbol{u}) &= [\dot{\boldsymbol{\varepsilon}}(\boldsymbol{u}) : \dot{\boldsymbol{\varepsilon}}(\tilde{\boldsymbol{u}})]\, \dot{\boldsymbol{\varepsilon}}(\boldsymbol{u}) \\ &= [\dot{\boldsymbol{\varepsilon}}(\boldsymbol{u}) \otimes \dot{\boldsymbol{\varepsilon}}(\boldsymbol{u})]\, \dot{\boldsymbol{\varepsilon}}(\tilde{\boldsymbol{u}}), \end{aligned}$$

where in the last equality we have used the identity $(\boldsymbol{a} : \boldsymbol{b})\boldsymbol{c} = (\boldsymbol{c} \otimes \boldsymbol{b})\boldsymbol{a}$ for second-order tensors $\boldsymbol{a}, \boldsymbol{b}, \boldsymbol{c}$, where $\otimes$ is the outer product between tensors. Note that the adjoint equation (2.18) is linear in its unknowns $(\boldsymbol{v}, q)$, and it is forced by the misfit in plate velocity data on the top surface $\partial\Omega_t$. The momentum equation involves an anisotropic stress tensor (2.19), which depends on the forward velocity $\boldsymbol{u}$.

Second derivatives (i.e., Hessians) are needed to compute the Newton update step for finding the MAP point, and for computing Gaussian approximations of the posterior distribution. This second derivative information can either be calculated through finite differences of gradients, or by taking second derivatives of the Lagrangian function (2.16) with respect to all variables (Tröltzsch, 2010; Petra, Zhu, et al., 2012). Both approaches only provide the application of the Hessian to vectors, and each of these Hessian-vector multiplications comes at the cost of two Stokes-like solves: Taking finite differences between gradients requires the computation of gradients for perturbed parameters, amounting to two (one nonlinear forward and one linear adjoint) PDE solves. Taking second variations of the Lagrangian results in two linear PDEs (sometimes called incremental equations or second-order adjoint) that must be solved to compute the application of the Hessian matrix to a vector. Such a Hessian-vector application is sufficient if the Newton system (2.12a) is solved using the conjugate gradient method. Moreover, it also allows the assembly of the Hessian column-by-column (through application on unit vectors) or, if the number of parameters is too large for this approach, the construction of a low-rank approximation of the Hessian (Bui-Thanh et al., 2013). The inverse of the resulting (approximation of the) Hessian matrix is then the covariance matrix of a Gaussian approximation of the posterior, as described in Section 2.3.

2.4 Model Setup and Numerical Solution

We setup a 2-D Cartesian problem with many of the principal tectonic elements that are thought to be relevant in driving and resisting plate motions. The model has three subducting plates with different amounts of slab penetration into the lower mantle. This variation is intended to span the range of slab penetration and expected coupling that may exist in the global distribution of plates with some slabs only partially penetrating the upper mantle and others fully embedded into the high viscosity lower mantle. Different sensitivities could exist depending on how much of the lower mantle is coupled into plate motions. One of the subduction zones has an overriding oceanic back-arc basin (with a small spreading center) which can result in trench-rollback. In a subduction zone with a back arc basin and rollback, our ability to infer mantle properties might differ from a margin without trench-rollback since the proportion of buoyancy force pulling the plate can differ significantly between these systems. Moreover, the seismic coupling between subduction zones that have trench rollback, versus those that do not, is central to the discussion on the occurrence of great earthquakes between subduction zones.

The thermal structure of the lithosphere is characterized by a half-space cooling model for the thermal boundary layer. The thermal structure for each slab is computed as follows. First, the top of the slab is identical with the weak zone interface (see below) projected to depth. We then define an initial thermal structure based on the half-space model with depth measured normal to the curving top of the slab. Finally, we diffuse this initial thermal structure for a time proportional to the transit time to arrive at that depth with the velocity of the subducting plate. This method results in thermal structures close to those obtained from the solution of the coupled flow and advection-diffusion problem with nonlinear viscosity (e.g., Billen and Hirth (2007)). The slabs conserve their buoyancy compared to the incoming plate, but have realistic thermal gradients, for example between the slab interior and the mantle wedge (Fig. 2.1c). The domain has a width of 12,000 km and depth of 1,500 km. The properties that we ascribe to the model are summarized in Table 2.1.

We assume that the effective viscosity has six orders of magnitude variation, 10^{18}–10^{24}Pa·s, across the model domain. The minimum effective viscosity ($\eta = 10^{18}$Pa·s) corresponds to η_{min}, while the maximum effective viscosity (η_{max}) is $10^{24}\text{Pa} \cdot \text{s}$. The smallest viscosities occur within subducting plate boundaries and mid-ocean ridges, while the largest occur within the interior of oceanic plates. We tie the effective viscosity η_{eff} within the upper mantle below stationary plates to the inferred value of the mantle viscosity from post-glacial rebound studies by adjusting the pre-exponent A_{rad} in the forward model. A discontinuity at 670 km depth is included, where a nonlinear viscosity (2.5) transitions to constant viscosity, i.e., a Newtonian rheology.

The characteristic functions $\chi_i(\cdot)$ for the weak zones modeling individual plate boundaries are parameterized with a Gaussian distribution about a centerline. The centerline of the weak zone (and hence the top surface of the initial thermal slab, as described above) is constructed such that it falls within the middle of slab profiles from the Slab 1.0 model (Hayes et al., 2012) of nearly all ocean-ocean and ocean-continent subduction zones (Fig. 2.1d). The weak zones consequently have a shallow dip (approximately 5 degrees) at the surface and represent a significant improvement over the parameterization we have used in the past (Stadler et al., 2010).

Our standard case has the following set of parameters: a stress-strain rate exponent,

Table 2.1: Physical quantities used in our tests.

Parameter	Value
Density (ρ)	3300 kg/m^3
Gravity (g)	9.81 m/s^2
Coefficient of Thermal expansion (α)	2×10^{-5}
Temperature Difference ΔT	1400 K
Depth of layer (D)	1500 km
Thermal Diffusivity (κ)	10^{-6} m^2/s
Reference Viscosity (η_{ref})	10^{20} Pa $\cdot$ s
Rayleigh Number (Ra)	3.06×10^7
Strain rate exponent in upper mantle (n)	3.0

n, of 3, a yield stress, σ_y, of 128.9 MPa and coupling factors, Γ_i, from left to right of $2 \cdot 10^{-5}$, 10^{-5} and $3 \cdot 10^{-5}$ so that the plate coupling varies with the middle plate boundary being the most decoupled and the right most plate boundary the most coupled. This model has a realistic strain rate exponent in the upper mantle, with a yield stress that allows plates to be strong while still being able to weaken as they subduct. The different degree of plate coupling at each subduction zone were set to mimic situations expected in a global model.

We discretize the Stokes equations and their adjoints using finite elements on a locally refined mesh of unstructured quadrilaterals. In particular, the mesh is refined around plate boundaries and hinge zones (to ~ 5 km resolution) and around the edges of slabs. It consists of 47,360 elements overall. We use Taylor-Hood finite elements (Elman et al., 2005), i.e., continuous second-order elements for the velocity components, and continuous first-order elements for the pressure. Our implementation is in `MATLAB`[1], and we use `COMSOL v3.5`[2] for meshing and for the assembly of finite element matrices, similar to the model problems in Petra and Stadler (2011).

Newton's method is used to solve the nonlinear state equation (2.1). We use the fact that the solution of (2.1) minimizes a viscous energy functional to ensure convergence of the Newton iteration by reducing the size of the update when the a Newton update step fails to reduce the viscous energy (Petra, Zhu, et al., 2012; Worthen et al., 2014). A commonly used alternative to Newton's method for the solution of nonlinear equations is the Picard fixed point method, which, however, often converges much slower than Newton's method. Additionally, because the linearization of the forward problem is self-adjoint, the operator in the adjoint

---

[1] `http://www.mathworks.com`

[2] `http://www.comsol.com`

equations is the same operator that arises in the Newton linearization for the forward Stokes problem. This means that any forward nonlinear Stokes solver based on a Newton method is already equipped with the operator needed to solve the adjoint Stokes problem. Our implementation uses a direct, factorization-based solver for the linear(ized) Stokes problems. In a large-scale framework, this direct solver must be replaced by an iterative Stokes solver, for instance a preconditioned Krylov method (Elman et al., 2005). We terminate the Newton iterations for the solution of the nonlinear Stokes equations when the nonlinear residual is reduced by four orders of magnitude.

Computing the MAP point amounts to solving the optimization problem (2.10), which can be written as an optimization problem with PDE constraints given by the nonlinear Stokes equations (2.1). Using derivatives computed through adjoint equations (see Section 2.3), we employ the (inexact) Newton method outlined in Section 2.3 for the solution of this PDE-constrained optimization problem. Here, inexactness refers to the fact that the Hessian system (2.12a) is not solved exactly, but iteratively through a conjugate gradient method (Nocedal and Wright, 2006). This approach only requires Hessian-vector applications rather than the assembled Hessian operator. Each Hessian-vector application requires two linear Stokes solves and assembling the Hessian matrix would require two linear Stokes solves for each parameter, which is infeasible for problems with a large number of parameters. In particular for these problems, solving (2.12a) using the conjugate gradient method can be a significant advantage compared to constructing the Hessian matrix. We use line search to ensure sufficient decent of the optimization functional and terminate the Newton iterations for the MAP point after the gradient has been reduced by four orders of magnitude.

2.5 Forward Model

With the distribution of temperature and weak zones as described for the standard case, we find that the resulting effective viscosity is characterized by strong plates and a weak asthenosphere (Fig. 2.1). Each of the three subducting oceanic plates move with velocities of 3-10 cm/yr and with the right most over-riding plate being nearly stationary while the other two over-riding plates roll-back with velocities of 1-2 cm/yr. The plates are strong away from plate boundaries and have piecewise constant surface velocities. Below the intersection of the faults (shear zones) with the surface, where the plate starts to bend within the hinge zone, the effective viscosity is reduced as these areas exceed the yield stress. The yield stress and

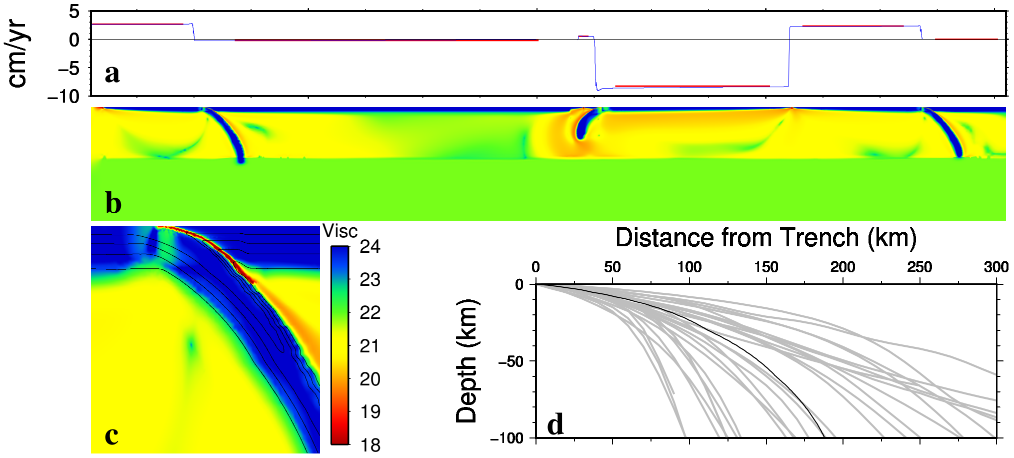

Figure 2.1: (a) Surface velocity from a forward calculation (thin blue line) and sub-sampling used to create the data for the inverse models (red lines). (b) $\log_{10}$ of the effective viscosity in Pa·s. (c) Detail of the effective viscosity for the left-most subduction zone overlaid by contours of temperature (in black). (d) Profile of the weak zone used in our dynamic model (black line) compared against a representative sample of global seismic coupling zones taken from the Slab 1.0 model (Hayes et al., 2012) (in grey).

prefactor to the viscosity law (for the given temperature field) were chosen to give these velocity and effective viscosity outcomes, which are similar to those found previously (Zhong, Gurnis, and Moresi, 1998; Billen and Hirth, 2005; Billen and Hirth, 2007)

Plate motions are sensitive to the strength of the plate margins; by plate margin strength we refer to the combination of the strength of the oceanic lithosphere and slab and the strength of the coupling (shear zone) between over-riding and subducting plates. As plate margins become progressively weaker, plate motion eventually becomes insensitive to resistive forces at plate boundaries (e.g. King and Hager (1990)). This can be seen in the limit when an individual coupling factor, Γ_i, or their average, $\langle\Gamma\rangle$, becomes small (Fig. 2.2a). Here and in the following, $\langle\Gamma\rangle$ is the arithmetic mean of the individual weak zone prefactors Γ_i. As the fault (shear zone) weakens ($\Gamma_i \rightarrow 0$) plates are free to slide by each other with the resistance coming from the effective viscosity of the slab and bending plate. As the coupling factor of a plate boundary approaches 10^{-10}, plate boundaries become very weak (Fig. 2.2); when the value approaches unity, plates become locked and the RMS of the surface velocity asymptotes to approximately 2.5 cm/yr. We will not further investigate the limit of fully locked plates. For our subsequent considerations, we refer to the region $10^{-8} < \langle\Gamma\rangle < 10^{-4}$ to be in the *sensitive* regime because variation in $\langle\Gamma\rangle$ leads to

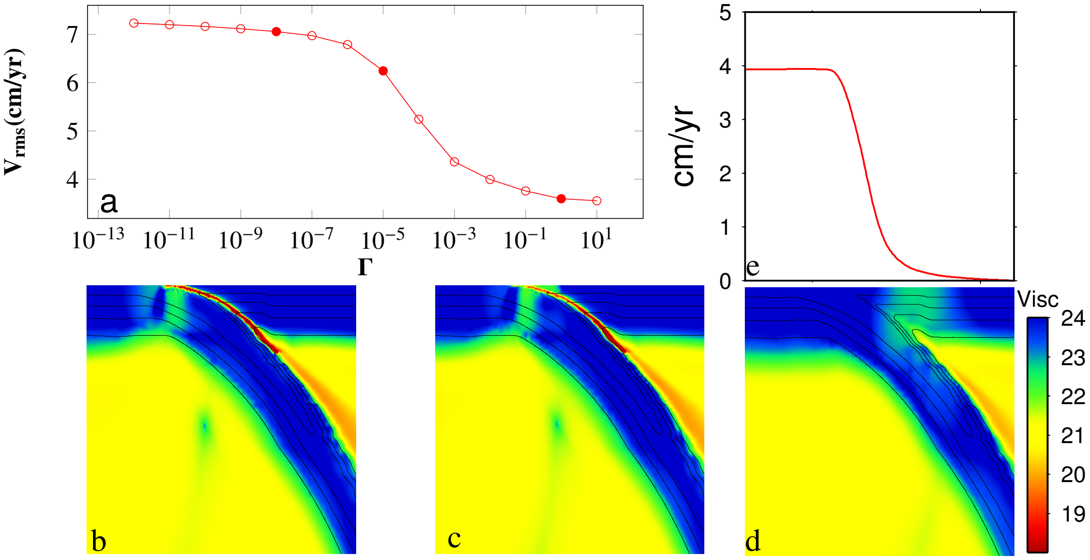

Figure 2.2: (a) Change in plate velocity (as RMS across the top surface) as a function of plate coupling $\langle\Gamma\rangle$ for a set of models in which all three plate margins have the same coupling factor. Filled symbols denote the cases shown in panels b-d. Viscosity structure in the vicinity of right most subduction zone for three values of coupling: (b) $\langle\Gamma\rangle = 10^{-8}$, (c) $\langle\Gamma\rangle = 10^{-5}$, and (d) $\langle\Gamma\rangle = 1$ (e) Surface velocity profile of right most subduction zone at $\langle\Gamma\rangle = 1$.

a substantial change in plate velocity, while the region $\langle\Gamma\rangle < 10^{-8}$ will be referred to as the *insensitive* regime. We choose $\langle\Gamma\rangle < 10^{-8}$ to be the insensitive region because the effective viscosity, η_{eff}, approaches the minimum effective viscosity limit. Note that the minimum viscosity η_{min}, however, is only attained exactly for $\Gamma_i = 0$ due to the form of the viscosity given in (2.5). In Fig. 2.2a, as $\langle\Gamma\rangle < 10^{-6}$, the RMS plate velocity approaches an asymptotic value slightly larger than 7 cm/year. Note that the effective viscosity is bounded from below by $\eta_{\text{min}} = 10^{-2}$; since the characteristic weak zone functions χ_i are Gaussians, they attain their minimum only at the center and choosing $\Gamma_i < 10^{-6}$ further weakens the plate coupling and thus effects the plate velocity.

As $\langle\Gamma\rangle$ increases, deformation within the over-riding plate increases as seen from the effective viscosity in the vicinity of the subduction zones (Fig. 2.2b-d). When the shear zone becomes locked, the deformation shifts from a combination of the bending plate and shear zone to spatially distributed deformation in the over-riding plate. The distributed deformation within the over-riding plate now occurs over a larger length scale. For a given average viscosity of the plates, we expect that there should be a tradeoff when inferring n, Γ, and σ_y from plate motions, as each of these parameters influence plate motions.

2.6 Inverse Model

In this and the next section, we study the extent to which we can reconstruct the parameters, and find their trade-offs and uncertainties from plate motion data. We use the surface velocities from forward models as synthetic data. To generate this synthetic data, we solve forward problems with known rheological parameters and plate coupling factors, and compute the resulting plate motions. To obtain plate velocity data similar to what is available from a global kinematic model, we generate synthetic data from the computed surface velocities by taking a single scalar average of the velocities away from plate margins. To be precise, we use overall 78% of the top surface to compute RMS values for six plates defined in red, amounting to a five-dimensional data vector (see the thick red lines in Fig. 2.1a). We do not add noise to these synthetic averaged measurements. The retained data is similar to what is available from a global kinematic model of plate motions, namely Euler poles and associated uncertainties (determined from fracture zone, magnetic lineation, seismic focal mechanism, and GPS data) for each plate. The single scalar value for each plate is the 1-D equivalent (over a 2-D mantle cross section) to an Euler pole. These data are indicative of plates that are rigid away from plate margins, but the margins are free to deform if the inferred rheological parameters allow them to. For subducting oceanic plates, we set the areas without surface velocity constraints to be much larger than the expected zone of yielding and bending such that the data do not impose this length scale. We assume uncorrelated observations with a standard deviation of 0.21 cm/yr, i.e., C_{noise} is the unit matrix scaled by 0.21^{-2}. The experiments in this section do not incorporate a prior, and thus the MAP point is the maximum likelihood point; for convenience, we still refer to it as the MAP point.

We apply the methods developed above to infer the MAP estimates for the weakening factors Γ_i, the yield stress σ_y and the strain rate exponent n. We also report the standard deviation σ (corresponding to the $\log(\boldsymbol{m})$) for the Gaussian approximation of the posterior at the MAP point, i.e., the diagonal entries in the posterior covariance matrix. In our experiments we vary not only the underlying properties of the mantle flow system, but also which quantities are considered known and thus kept fixed, and which are considered uncertain and inverted for (Table 2.2).

As initial guess for the computation of the MAP point we choose the weak factors Γ_i equal to 10^{-3}, which is, for most cases, larger than the actual values. This

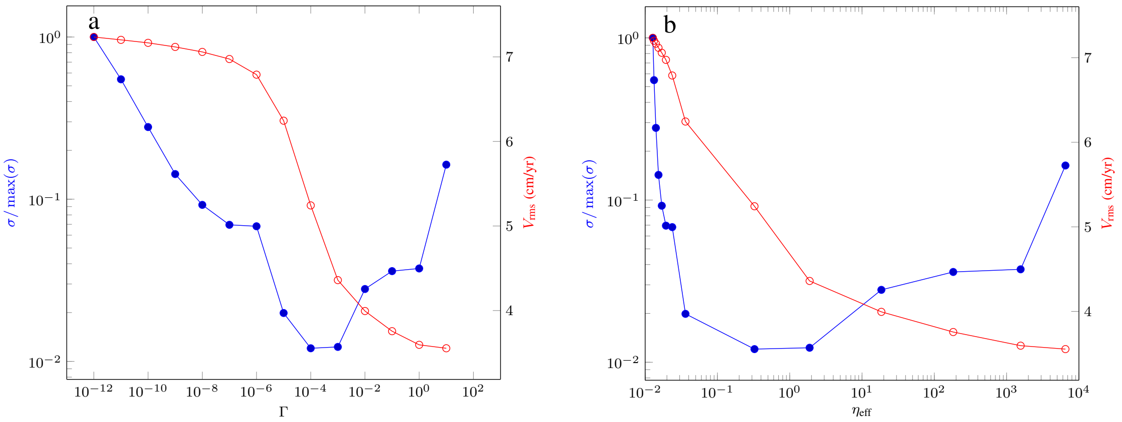

Figure 2.3: Relationship between the normalized standard deviation σ (in blue) and the average plate velocity V_{rms} (in red) as a function of the plate coupling factor $\Gamma(=\Gamma_1 = \Gamma_2 = \Gamma_3)$ (a), and as a function of the average effective viscosity η_{eff} within the weak zones (b).

would be a reasonable starting condition for a geophysical inversion as it makes no assumption about which margins are strong or weak, nor about the relative strength of plate coupling. We initialize the strain rate exponent with $n = 2.7$ and the yield stress with $\sigma_y = 84.4$MPa ($\sigma_y = 190$MPa in Case XIX). We observe in our numerical experiments that these initializations do not influence the recovered parameters, i.e., the optimization problem for the MAP point converges to the same solution independent of the initialization. This suggests that the negative log likelihood/posterior $\mathcal{J}(\cdot)$ does not have multiple local minima. For problems with two parameters, this is also suggested by the contour lines of the posterior pdfs shown later, as local minima in $\mathcal{J}(\cdot)$ would correspond to local maxima in the corresponding pdfs. We terminate the optimization problem when the norm of the gradient $\mathcal{G}$ has been decreased by a factor of 10^4.

Case	V_{rms} (%surf. cov./plate)	Γ_1 (left)	Γ_2 (middle)	Γ_3 (right)	σ_y (MPa)	n
I	78%	$2 \cdot 10^{-5}/2 \cdot 10^{-5}/0.470$	$10^{-5}/10^{-5}/0.1630$	$3 \cdot 10^{-5}/3 \cdot 10^{-5}/0.608$	(128.9)	(3.0)
II	78%	$2 \cdot 10^{-8}/2 \cdot 10^{-8}/4.65$	$10^{-8}/10^{-8}/2.35$	$3 \cdot 10^{-8}/3 \cdot 10^{-8}/6.36$	(128.9)	(3.0)
III	78%	$2 \cdot 10^{-5}/2 \cdot 10^{-5}/0.66$	$10^{-5}/10^{-5}/0.185$	$3 \cdot 10^{-5}/3 \cdot 10^{-5}/0.867$	128.9/128.9/0.0969	(3.0)
IV	78%	$2 \cdot 10^{-8}/2 \cdot 10^{-8}/6.19$	$10^{-8}/10^{-8}/2.72$	$3 \cdot 10^{-8}/3 \cdot 10^{-8}/9.66$	128.9/128.9/0.0833	(3.0)
V	78%	$2 \cdot 10^{-5}/2 \cdot 10^{-5}/0.553$	$10^{-5}/10^{-5}/0.310$	$3 \cdot 10^{-5}/3 \cdot 10^{-5}/0.0.610$	(128.9)	$3.0/3.0/2.67 \cdot 10^{-3}$
VI	78%	$2 \cdot 10^{-8}/2 \cdot 10^{-8}/5.94$	$10^{-8}/10^{-8}/9.24$	$3 \cdot 10^{-8}/3 \cdot 10^{-8}/6.51$	(128.9)	$3.0/3.0/4.31 \cdot 10^{-3}$
VII	78%	$(2 \cdot 10^{-5})$	(10^{-5})	$(3 \cdot 10^{-5})$	$128.9/128.9/8.05 \cdot 10^{-2}$	$3.0/3.0/1.83 \cdot 10^{-3}$
VIII	78%	$(2 \cdot 10^{-8})$	(10^{-8})	$(3 \cdot 10^{-8})$	$128.9/128.9/5.37 \cdot 10^{-2}$	$3.0/3.0/1.1 \cdot 10^{-3}$
IX	78%	$2.0 \cdot 10^{-5}/2 \cdot 10^{-5}/0.564$	$10^{-5}/10^{-5}/0.485$	$3.0 \cdot 10^{-5}/3 \cdot 10^{-5}/1.40$	128.9/128.9/0.338	$3.0/3.0/9.11 \cdot 10^{-3}$
X	78%	$2 \cdot 10^{-8}/2 \cdot 10^{-8}/3.29$	$10^{-8}/10^{-8}/5.16$	$3 \cdot 10^{-8}/3 \cdot 10^{-8}/5.72$	$128.9/128.9/9.34 \cdot 10^{-2}$	$3.0/3.0/3.12 \cdot 10^{-3}$
XI	All V	$2.0 \cdot 10^{-5}/2 \cdot 10^{-5}/0.926$	$10^{-5}/10^{-5}/0.429$	$3.0 \cdot 10^{-5}/3 \cdot 10^{-5}/1.37$	128.9/128.9/0.321	$3.0/3.0/8.5 \cdot 10^{-3}$
XII	78%	$2 \cdot 10^{-6}/2 \cdot 10^{-6}/1.64$	$10^{-5}/10^{-5}/0.998$	$3 \cdot 10^{-5}/3 \cdot 10^{-5}/1.97$	128.9/128.9/0.471	$3.0/3.0/1.41 \cdot 10^{-2}$
XIII	All V	$2 \cdot 10^{-6}/2 \cdot 10^{-6}/0.926$	$10^{-5}/10^{-5}/0.429$	$3 \cdot 10^{-5}/3 \cdot 10^{-5}/1.37$	128.9/128.9/0.321	$3.0/3.0/8.50 \cdot 10^{-3}$
XIV	78%/47%(right)	$1.965 \cdot 10^{-5}/2 \cdot 10^{-5}/0.40$	$10^{-5}/10^{-5}/0.70$	$2.793 \cdot 10^{-3}/3 \cdot 10^{-3}/0.839$	129.9/128.9/0.155	$3.0/3.0/5.27 \cdot 10^{-3}$
XV	78%/60%(right)	$1.30 \cdot 10^{-5}/2 \cdot 10^{-5}/0.404$	$1.07 \cdot 10^{-5}/10^{-5}/0.680$	$1.26 \cdot 10^{-3}/3 \cdot 10^{-3}/0.748$	154/128.9/0.156	$3.017/3.0/5.36 \cdot 10^{-2}$
XVI	78%/73.3%(right)	$3.32 \cdot 10^{-6}/2 \cdot 10^{-5}/0.454$	$1.37 \cdot 10^{-5}/10^{-5}/0.838$	$5.5 \cdot 10^{-4}/3 \cdot 10^{-3}/1.0$	266.1/128.9/0.788	$3.08/3.0/2.77 \cdot 10^{-2}$
XVII	78%/86.7%(right)	$1.59 \cdot 10^{-6}/2 \cdot 10^{-5}/0.592$	$1.71 \cdot 10^{-5}/10^{-5}/0.857$	$4.6 \cdot 10^{-4}/3 \cdot 10^{-3}/0.645$	517/128.9/0.769	$3.22/3.0/3.26 \cdot 10^{-2}$
XVIII	78%	$10^{-5}/10^{-5}/0.308$	$10^{-5}/10^{-5}/0.308$	$10^{-5}/10^{-5}/0.308$	$128.9/128.9/7.34 \cdot 10^{-2}$	$3.0/3.0/3.01 \cdot 10^{-3}$
XIX	78%	$2.79 \cdot 10^{-8}/2 \cdot 10^{-6}/9.4$	$1.26 \cdot 10^{-7}/10^{-5}/12.6$	$10^{-7}/3 \cdot 10^{-5}/6.91$	$66.5/53.3/2.52 \cdot 10^{-2}$	$2.99/3.0/8.93 \cdot 10^{-3}$

Table 2.2: Parameter estimation results for several test cases. Each entry for the prefactors, yield stress, and strain rate exponent are given as inferred/true/standard deviation ($\log(\boldsymbol{m})$). Quantities that are considered known and thus fixed in the inversion are shown in parentheses. The top surface velocity data is constant for each plate, and the percentage of the top surface with these constant velocity constraints is indicated in the second column.

In the first experiment (Table 2.2, Case I), we assume that the two global quantities, yield stress and strain rate exponent, are known, and we attempt to infer the plate boundary coupling factors, Γ_i, $i = 1, 2, 3$, for each weak zone in the sensitive regime. We recover the prefactors, and, as a consequence, the shear stresses within each plate boundary within one percent error after seven iterations. We correctly infer the different plate coupling strengths of each plate margin. This is important as the coupling strength for each subduction zone in a global geophysical inversion is expected to be different.

While the prefactors for Case I are in the sensitive regime, in Case II they are substantially smaller and thus lie in the insensitive regime. Again, the inferred MAP estimate coincides with the true prefactors. However, there is a substantial increase in the uncertainty of the recovered coupling factors compared to Case I (Table 2.2). In Fig. 2.3, we study the interplay between standard deviation and the coupling factors systematically. We perform experiments that are identical to Cases I and II, i.e., with fixed strain rate exponent and yield stress, but choose identical true coupling factors $\Gamma_1 = \Gamma_2 = \Gamma_3$ for each model calculation. We find that uncertainties are largest when plate couplings are small or when the plate margin is fully coupled (Fig. 2.3a), i.e., if the plate coupling factors are in the insensitive regime.

In the previous inversions, the yield stress and strain rate exponent were considered known. As the yield stress and strain rate exponent are also uncertain, we attempt to infer each one of them individually along with the prefactors in Cases III (inference of Γ_i, σ_y) and V (inference of Γ_i, n). In Cases III and V, we correctly infer the respective values. Although the uncertainty increases when the additional parameter is inferred, the computational cost remains approximately the same as we are able to determine the correct value within 1% after 7 iterations. Similarly, the correct values are inferred when $\langle\Gamma\rangle$ is in the insensitive region for the otherwise identical cases Cases IV and VI, although the uncertainty on the prefactors does increase within the insensitive compared to the sensitive regime.

We next attempt to infer the global constitutive parameters—the yield stress and strain rate exponent in the upper mantle—while assuming that the individual prefactors, Γ_i, are known for each plate boundary. Although inferring the global strain rate exponent and yield stress is not a realistic geophysical inversion as it assumes knowledge of the prefactors a priori, the case is illustrative of the tradeoffs likely to be seen in the full inversion of Γ, σ_y and n. We are able to infer the correct strain rate exponent and yield stress for each case after 8–9 iterations, both in the sensitive

(Case VII) and insensitive (Case VIII) regimes. There is no significant difference in the rate of convergence during the inversion of either n or σ_y when $\langle \Gamma \rangle$ is in the sensitive or insensitive regime.

We now consider a realistic situation where the plate boundary strengths, the yield stress and the strain rate exponent are all unknown, i.e., we infer five parameters. Cases IX and X represent inversions where we do not assume any of the rheological parameters in the constitutive relationship other than the activation energy. Despite the potential for tradeoffs in the rheological parameters, we are able to recover the true values even when all five parameters are uncertain. However, the uncertainty of the recovered prefactors and rheological parameters increases substantially compared to the earlier cases with fewer parameters left unconstrained. While the values of the parameters are recovered within 1%, it does take more forward–adjoint iterations to converge to the true value: Approximately 10 iterations in the five parameter estimation cases (IX and X) versus 5-6 iterations in the comparable three parameter cases (I,II). We attribute the larger computational cost to the larger number of parameters, and the resulting interplay between the rheological parameters where tradeoffs in plate coupling, strain rate weakening and yielding act to minimize the plate velocity misfit. These tradeoffs will be explored in the Bayesian inference context in the subsequent section.

With the cases above we showed that parameters (plate couplings, yield stress and strain rate exponent) of an unconstrained system can be inferred when the surface data is approximated with a single RMS value for each plate away from plate boundaries. However, there is an important untested assumption of the role played by approximating the surface velocities by a single RMS value for each plate. The influence of how the piecewise RMS velocity data is applied is demonstrated with additional calculations, in which we change the parts of the top surface that are assumed to move rigidly, and increase a coupling factor such that the plate motion causes deformation in the adjacent plate interior.

From Case IX with all of the standard parameters free and 78% of the surface covered with piecewise constant RMS values, we compare this against a calculation using all of the surface data without the piecewise constant assumption (XI). Here again, all of the parameters are recoverable except that their variance has been reduced by about a half (Table 2.2). As the influence and tradeoff that occurs in response to surface constraints can be better seen with a larger spread of the coupling factors, we consider Cases XII and XIII with the left most coupling factor reduced by 10.

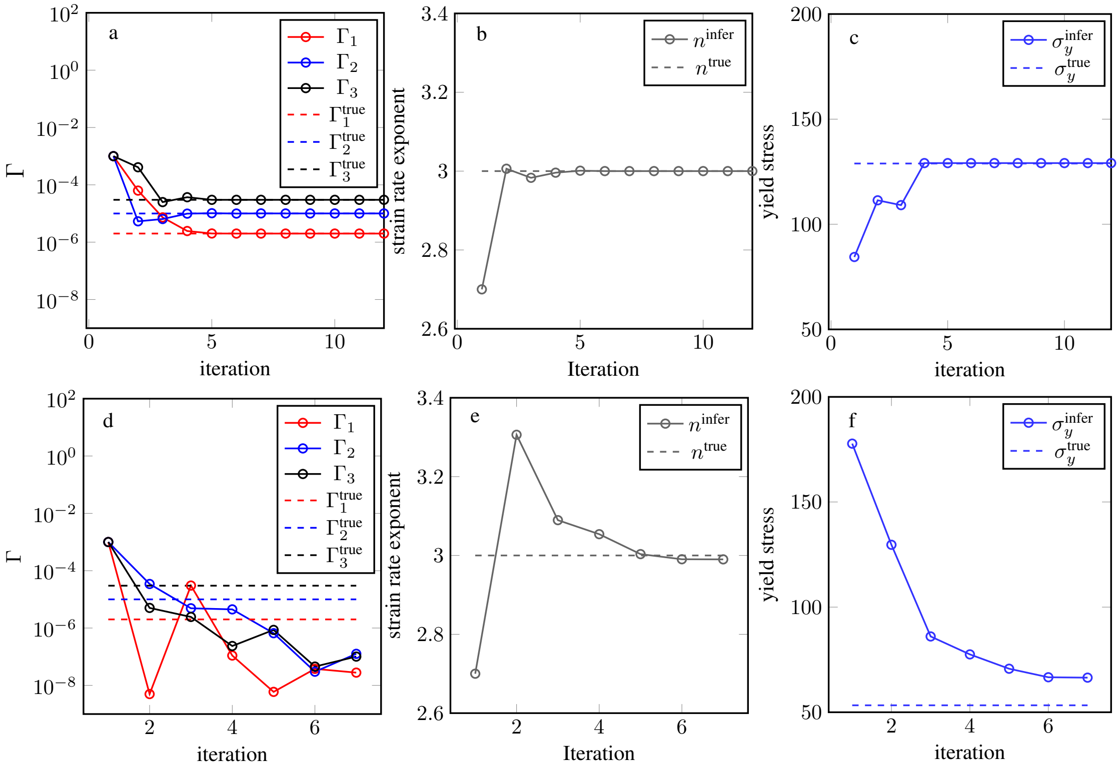

Figure 2.4: Convergence towards MAP points for Case XII (a–c) and for Case XIX (d–f). The plots show the convergence of Γ_i, n, and σ_y as function of the iteration. The open circles depict the iterates and the dashed horizontal lines show the values used to generate the synthetic data.

Again, all of the parameters are recoverable either with all surface velocities used as data or with 78% as RMS values within plate interiors (Fig. 2.4a-c). The variances are again reduced when using the more complete data. Now we retain the greater spread in coupling factors and strain rate exponent but decrease the yield stress from 129 MPa to 53 MPa (Case XIX), such that a larger fraction of the lithosphere yields. The plates become more deformable and the average strain rate within the plate interiors increases from $2.22 \cdot 10^{-16}\mathrm{s}^{-1}$ (Case I) to $6.77 \cdot 10^{-16}$ s^{-1} (Case XIX). Using only the RMS values over 78% of each plate, there is a strong tradeoff between parameters and only the global strain rate exponent is correctly recovered (Fig. 2.4e). In this case, the inversion responds to the imposed rigid plate motion data by recovering a larger yield stress (Fig. 2.4f). The larger yield stress allows the plates to stiffen, but in order to fit the overall magnitude of plate velocities, the MAP estimate has weaker plate margins (Fig. 2.4d).

The influence of the spatial extent of the imposed data is demonstrated with Cases XIV to XVII which are otherwise identical to Case IX, except that the coupling

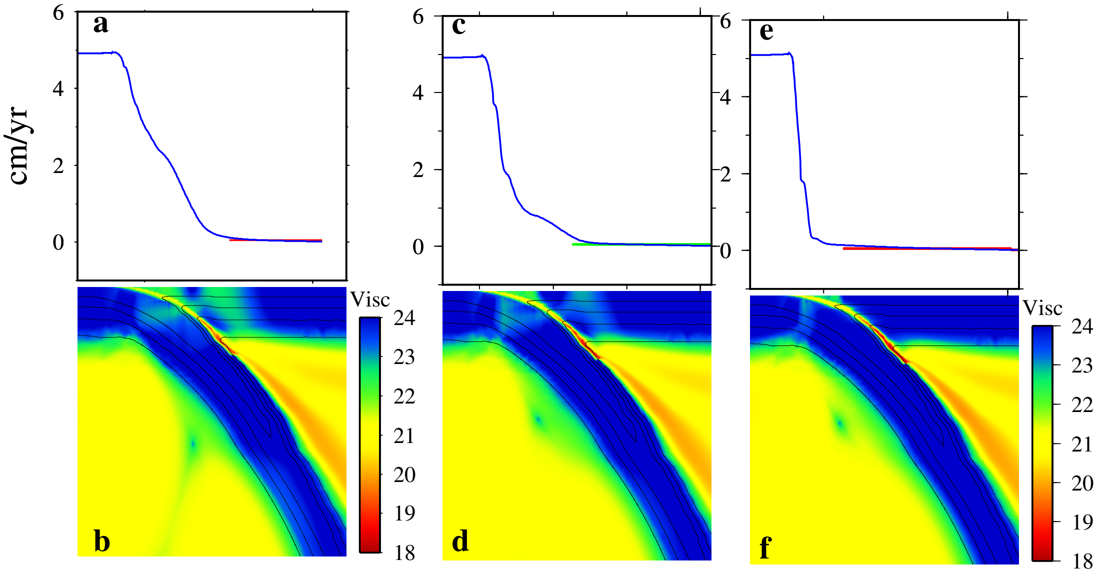

Figure 2.5: (a) Plate velocities from a forward calculation (blue curve) with a large coupling factor for right-most subduction zone. The distribution of velocities used to compute RMS velocities over 87% (pink line) and 47% (green line) over the right most plate. (b) Effective viscosity from the forward model. (c) Inverse with plate velocities (blue) of right-most subduction zone with green line denoting data. (d) Effective viscosity (Case XV). (e) Inverse with plate velocities (blue) and pink line denoting data over 87% of right most plate (Case XVII). (f) Effective viscosity (Case XVII).

factor for the right most subduction zone is increased from the standard value of 3×10^{-5} to 3×10^{-3} (Table 2.2). In this case, the margin broadens over a length-scale defined by the vertical projection of the weak zone to the surface (Fig. 2.5a). The RMS velocities are now determined over different fractions of the rightmost plate in this series of calculations. When 60% of the surface of the over riding plate is used (Fig. 2.5c), the MAP point “responds” by creating a more rigid plate with less yielding immediately below the extend of the imposed data, but adjacent to a zone of deformation (Fig. 2.5d). Since part of the motion of the subducting oceanic plate is being accommodated by deformation of the over-riding plate, the inversion estimates a coupling factor that is smaller than the factor used to generate the synthetic data. If the fraction of the imposed data is enlarged to now encompass nearly the entire surface area of the over riding plate, we infer an entirely rigid overriding plate with a much weaker plate margin (Fig. 2.5e-f). The recovered yield stress is substantially larger than the actual value so as to decrease the yield stress within the over riding plate. That decreased yield stress nearly eliminates the yielding with the hinge zone. The four cases show that the recovered values progressively deviate when an otherwise deformable plate is forced to be rigid in the inversion (Table 2.2). In general, the coupling factors decrease and the strain-rate exponent increases. However, when the area of the right most plate with the imposed RMS values is reduced to 47% (Case XIV), such that there is little rigid plate data applied within the deforming region, the prefactors for all three subduction zones (as well as the strain rate exponent and yield stress) can be recovered within about 1%, effectively reducing the tradeoffs between the inferred parameters.

Finally, we turn to the recovery of dissipation, Φ, (2.6), a measure of energy dissipated by deformation of a viscous material. As plates accumulate large stresses at subduction zones, there is dynamic weakening near the hinge zones and a concentration of dissipation as oceanic plates subduct into the mantle (Buffett and Becker, 2012; Stadler et al., 2010; Alisic, Gurnis, Stadler, Burstedde, and Ghattas, 2012; Buffett and Rowley, 2006). To better understand our ability to invert for dissipation, we compute the total dissipation in the whole domain and within the hinge and weak zones (Table 2.3). Dissipation was determined in those parts of the domain where yielding occurs (mostly in the hinge zones) in the left, middle and right subduction zone and are denoted by $\Omega_l^y, \Omega_m^y, \Omega_r^y$, respectively; for some extreme models given below, the nodes that yield can differ between forward and recovered models, such that these regions can likewise differ between forward and inverse. For comparison, we also determined the dissipation within low viscosity weak zones $\Omega_1^w, \Omega_2^w, \Omega_3^w$, respectively for the left, middle and right plate boundaries. We start with Case IX, where all of the standard parameters were left unconstrained and all were recovered on inversion. Since all of the velocities and viscosities were essentially identical between forward and the MAP point from the inversion, so too is the dissipation, both locally and through the whole domain (Table 2.3).

Recovery of parameters was degraded when deforming plates were approximated on recovery with piecewise constant RMS velocity data; likewise, recovery of the dissipation was degraded in these cases. When piecewise constant RMS velocity data is used over nearly the entire deforming rightmost plate (in response to the larger coupling factor in Case XVII, Fig. 2.5e-f), the dissipation is not well recovered locally. The recovery of the dissipation within the adjacent weak zone is particularly poor and, counter intuitively, the dissipation is over-estimated by a factor of two, despite the viscosity within the weak zone being much lower on recovery (Table 2.2.) However, the over riding plate is more rigid and the deformation (and hence dissipation) is shifted from within the plate to the weak zone between the

Table 2.3: Dissipation occurring locally and throughout the whole domain for selected cases. Values are shown as recovered/true. Symbols defined in text.

Dissipation	Case IX	Case XIV	Case XVII	Case XIX
$\Phi(\Omega_1^y)$	$9.30 \cdot 10^7/9.30 \cdot 10^7$	$1.03 \cdot 10^8/1.03 \cdot 10^8$	$7.71 \cdot 10^7/1.03 \cdot 10^8$	$9.16 \cdot 10^8/3.16 \cdot 10^9$
$\Phi(\Omega_2^y)$	$5.32 \cdot 10^8/5.32 \cdot 10^8$	$5.86 \cdot 10^8/5.86 \cdot 10^8$	$7.72 \cdot 10^8/5.86 \cdot 10^8$	$4.17 \cdot 10^8/1.67 \cdot 10^8$
$\Phi(\Omega_3^y)$	$1.46 \cdot 10^8/1.46 \cdot 10^8$	$1.12 \cdot 10^8/1.12 \cdot 10^8$	$9.18 \cdot 10^7/1.12 \cdot 10^8$	$6.77 \cdot 10^8/1.02 \cdot 10^9$
$\Phi(\Omega_1^w)$	$4.85 \cdot 10^7/4.85 \cdot 10^7$	$5.48 \cdot 10^7/5.50 \cdot 10^7$	$8.59 \cdot 10^7/5.50 \cdot 10^7$	$4.53 \cdot 10^7/2.81 \cdot 10^7$
$\Phi(\Omega_2^w)$	$9.20 \cdot 10^7/9.20 \cdot 10^7$	$7.63 \cdot 10^7/7.65 \cdot 10^7$	$2.84 \cdot 10^8/7.65 \cdot 10^7$	$4.57 \cdot 10^6/3.35 \cdot 10^6$
$\Phi(\Omega_3^w)$	$4.57 \cdot 10^7/4.57 \cdot 10^7$	$5.99 \cdot 10^7/4.47 \cdot 10^7$	$1.26 \cdot 10^8/4.47 \cdot 10^7$	$3.14 \cdot 10^7/1.12 \cdot 10^7$
$\Phi(\Omega)$	$4.16 \cdot 10^9/4.16 \cdot 10^9$	$4.15 \cdot 10^9/4.18 \cdot 10^9$	$4.15 \cdot 10^9/4.69 \cdot 10^9$	$4.70 \cdot 10^9/5.80 \cdot 10^9$

plates. Although, the dissipation is locally not well recovered in some plate boundaries, the total dissipation is only underestimated by 11%. We consider another extreme model with a lower yield stress and hence more deformable plate interiors (Case XIX). On inversion, with constant velocity data added to each plate interior, we found tradeoffs between the strength of the coupling factors and the yield stress (Fig. 2.5d-f). Here, we find that the dissipation of each plate boundary is recovered only within a factor of two, while the total dissipation is underestimated by nearly 40%. These problems can be largely avoided if we do not approximate deforming plates with constant velocity data. For example, partial recovery was achieved in Case XIV (Table 2.3) in which the deforming right-most plate was left mostly unconstrained, except in the far-field or several hundred km from the plate edge where the plate acts rigidly (Fig. 2.5). In this case, there is a slight tradeoff in the inferred values (smaller coupling on the right most plate boundary and an increase in yield stress), leading to a larger viscous dissipation in the hinge zone. However, all other measures of dissipation were reasonable well recovered.

2.7 Quantification of Uncertainty

Inferred parameters are uncertain due to noise in the surface velocity data, tradeoffs between rheological parameters, and modeling errors caused by the fact that the mathematical model is an idealized description of the real world. In this section, we explore these uncertainties and tradeoffs systematically, and go beyond the Gaussian approximation of the posterior distribution and use sampling to better characterize the posterior distribution.

As inference in a global geophysical system will likely require a large number of parameters while also involving expensive-to-evaluate parameter-to-observable maps, such a full sample-based characterization of the posterior distribution might not be feasible. A Gaussian approximation of the posterior, however, is often computationally tractable, as it usually only requires a number of PDE solves that is comparable to that needed for the computation of the MAP estimate. Naturally, the question arises how well the Gaussian distribution approximates the true posterior distribution. We will study this issue in our two-dimensional nonlinear Stokes flow problem with plates by comparing the Gaussian approximation—which is based on linearization of the parameter-to-observable map about the MAP point—to the true distribution, which is, in general, not Gaussian. To study this true distribution, we either use a regular parameter space grid, or Markov Chain Monte Carlo (MCMC) sampling (Gilks, 2005). For this comparison, we use a problem in which we infer three model parameters and compare two-dimensional conditional and marginal distributions. We interpret the distributions and study the tradeoffs between parameters physically.

The three parameters considered in this study are the strain rate exponent n, the yield stress σ_y and the strength of plate coupling Γ (we choose identical plate coupling factors, i.e., $\Gamma = \Gamma_1 = \Gamma_2 = \Gamma_3$). In some of our experiments we do not use prior knowledge for these parameters, in others we use prior distributions to incorporate likely ranges or ranges of interest for these parameters. For instance, strain rate exponents $n > 4$ are unlikely (Karato and Wu, 1993), as are coupling factors $\Gamma > 10^{-1}$, which would prevent realistic plate motion. Priors can also be used to express the fact that we are not particularly interested in certain parameter regimes, for instance in coupling factors $\Gamma < 10^{-8}$. Based on these considerations, we choose independent Gaussian distributions for the parameters given by $\boldsymbol{\pi}_{\Gamma}^{\text{prior}} = \mathcal{N}(10^{-5.5}, 3.43)$, $\boldsymbol{\pi}_{\sigma_y}^{\text{prior}} = \mathcal{N}(150\,\text{MPa}, 0.21)$, $\boldsymbol{\pi}_{n}^{\text{prior}} = \mathcal{N}(2.98, 0.0247)$, where σ_1, σ_2, and σ_3 are the standard deviations for the priors.

First, we study the two-dimensional conditional distributions shown in Figures 2.6 (no prior for parameters) and 2.7 (with Gaussian prior). Here, we have used a uniformly spaced grid to explore the true posterior distribution, which is clearly not feasible in higher parameter dimensions. In 2.6a, we observe a strong tradeoff between the magnitude of n and Γ. Models that fit the data with stronger plate coupling require a larger amount of strain weakening, giving an overall positive correlation between n and Γ. The distribution computed from the Hessian (red contours) approximates the true distribution (blue contours) within about one half of a standard deviation. However, as the plate margins become more strongly coupled, an even larger amount of weakening (larger n) than predicted by the Hessian is required, and causes the distribution to bend upward (Fig. 2.6a). In other words,

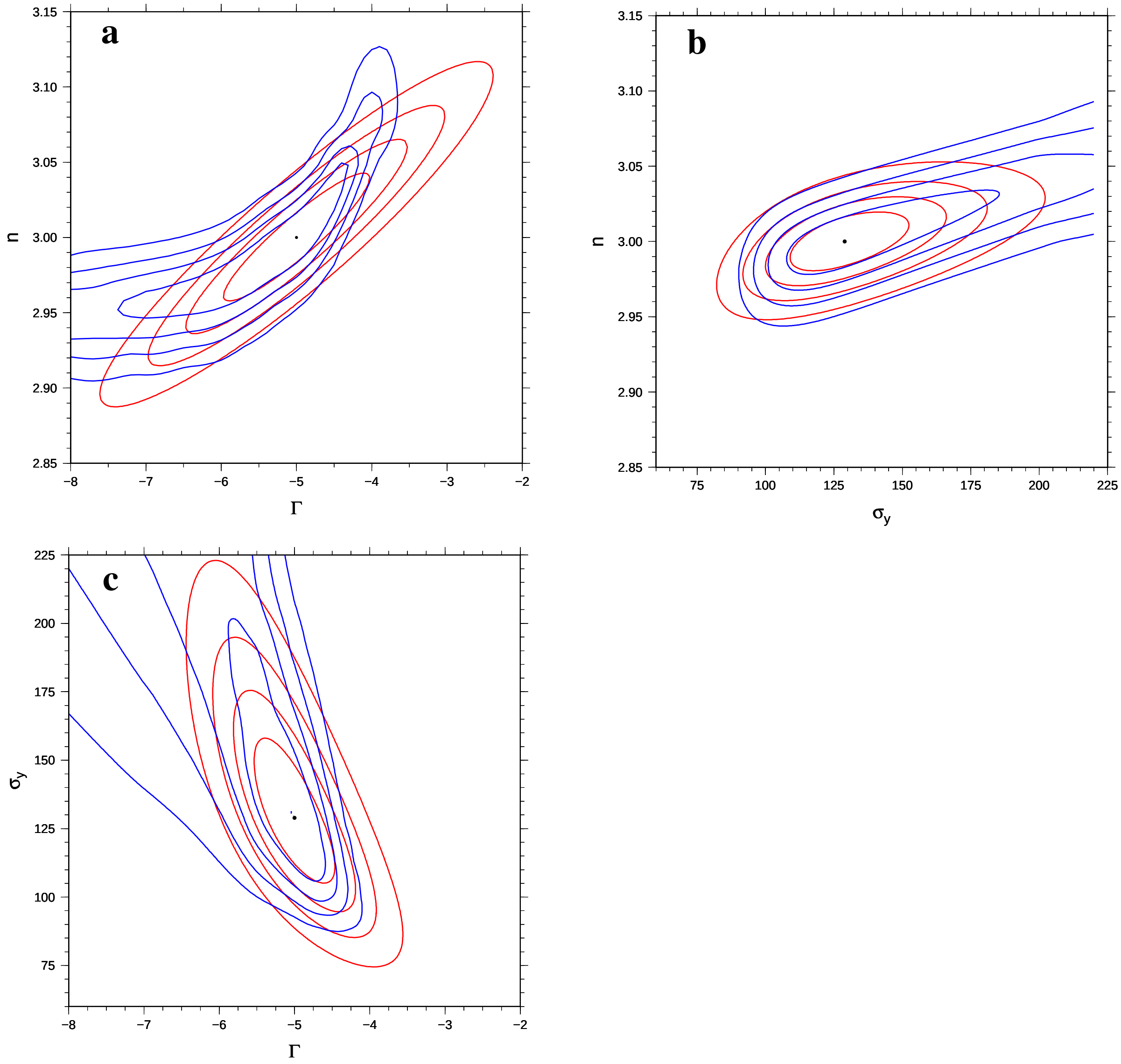

Figure 2.6: Comparison of two-dimensional conditional distributions for the three parameters n, Γ and σ_y. Contour lines (for 22%, 44%, 66%, 88%) corresponding to the Gaussian approximation at the MAP point for a setting without a prior are shown in red and for the true posterior distribution are shown in blue. For these conditionals, the parameters kept fixed are in (a) $\sigma_y = 128.9$ MPa, in (b) $\Gamma = 10^{-5}$, and in (c) $n = 3$. Note that due to the parameterization in (2.14), the contour lines of the Gaussian approximation do not appear as ellipses when plotted in the original n, Γ and σ_y system.

the model has a nonlinearity not accounted for by the linear assumption in (2.13). The calculation near $\Gamma = 10^{-4}$ and about $n = 3.1$ fits the surface velocity within $\approx 8\%$ but there is now more distributed deformation within both the over-riding and subducting plates. At the other end of the distribution, as the plate margins become weaker, plate motions become less sensitive to plate coupling. As parameters move from the sensitive to the insensitive regime as described previously (Fig. 2.2a), the best fitting models show a decrease in the strain rate exponent. The conditional distribution "flattens out" as the slope of the contours become horizontal—as Γ becomes small there are only small changes in the effective viscosity within the weak zone and hence similar data fits are achieved for different Γ (but the same n). This result is partly anticipated with both the insensitivity to plate velocity (Fig. 2.2a) and the increase in uncertainty (Fig. 2.3a) with small Γ.

Within the strain rate exponent-yield stress space, we find a conditional distribution from the Hessian near the MAP point that is locally a good approximation to the true conditional distribution (Fig. 2.6b). The yield stress trades-off with the strain rate exponent with a positive correlation as an increase in yield stress requires an increase in strain rate exponent so as to maintain plate velocities. However, the slope on the contours of n with respect to σ_y eventually flatten as there is no yielding when σ_y becomes too large. Within the space of yield stress and coupling factors, the conditional shows that the actual distribution is well predicted from the Hessian (Fig.2.6c). We find a negative correlation between the prefactor and the yield stress because as the coupling factor between plates increase, the plates need more yielding so as to fit the surface velocity data. The slopes of the contours become constant for small coupling factors when the yield stresses exceed the stresses in the system.

Finally, in Figure 2.8, we show two-dimensional marginals for the Gaussian approximation at the MAP point and compare with marginals of the true posterior distribution. The true distribution is explored using MCMC sampling, and in particular the Delayed Rejection Adaptive Metropolis (DRAM) method (Haario et al., 2006). We use 1177 samples computed through repeated forward solves. In Fig. 2.9, we plot the sample history for the prefactor Γ, which suggests that there is sufficient mixing. The integrated autocorrelation time for the chain τ given by

$$\tau = 1 + 2 \sum_{i=1}^{\infty} \rho_k, \tag{2.21}$$

where $\rho_k = \frac{\mathrm{Cov}[X_t, X_{t+k}]}{\mathrm{Var}[X_t]}$ is the autocorrelation at lag k, with X_t denoting the value of an observed state at time t. The integrated autocorrelation times for each parameters

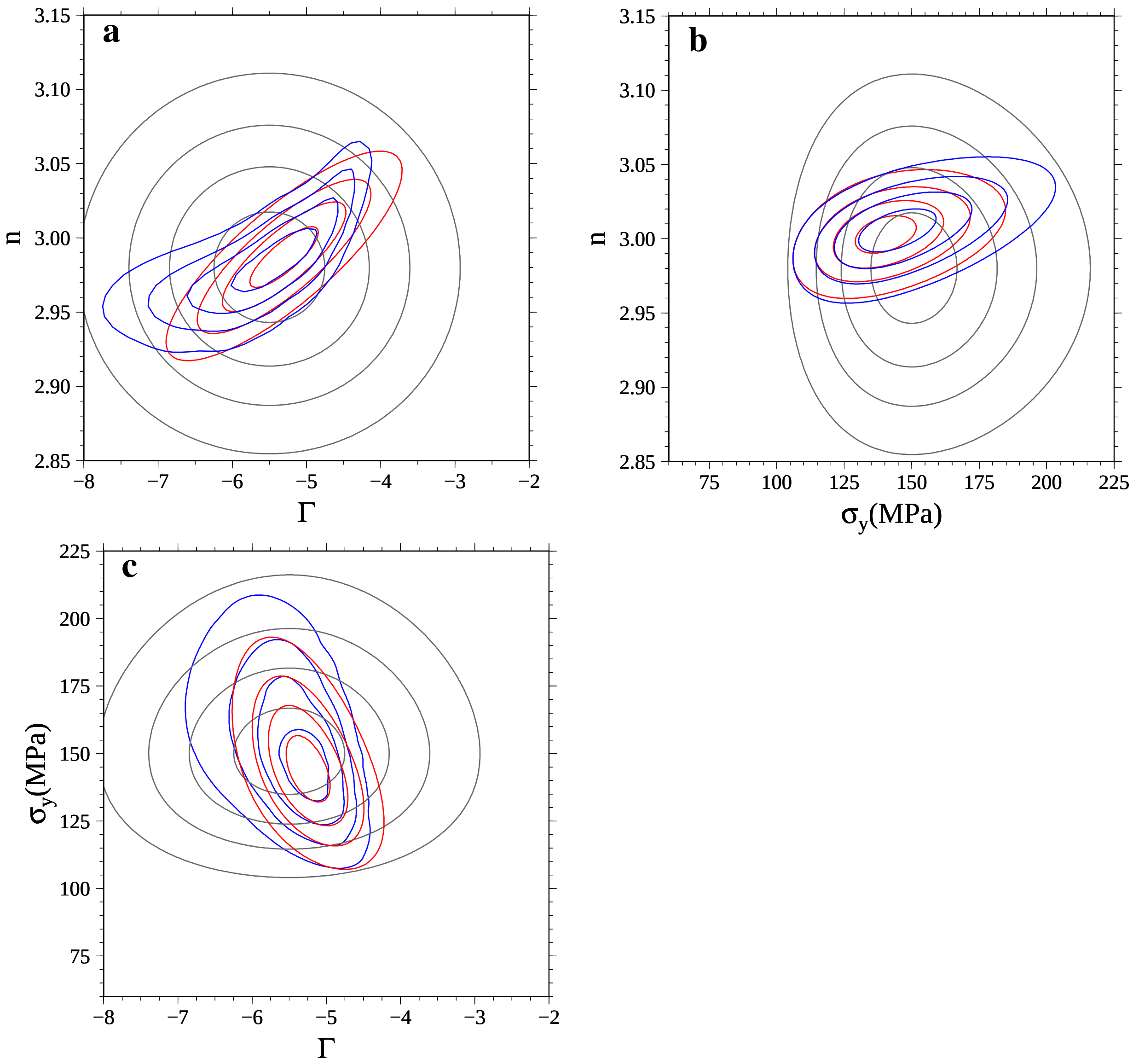

Figure 2.7: Comparison of two-dimensional conditional distributions (with Gaussian priors) for the uncertain parameters n, Γ and σ_y. Shown are contour lines (22%, 44%, 66%, 88%) corresponding to the Gaussian approximation at the MAP point (in red), contour lines for the actual posterior distribtion (in blue) and contour lines for the prior distributions (grey). For these conditionals, the parameters kept fixed are in (a) $\sigma_y = 128.9$, in (b) $\Gamma = 10^{-5}$, and in (c) $n = 3$.

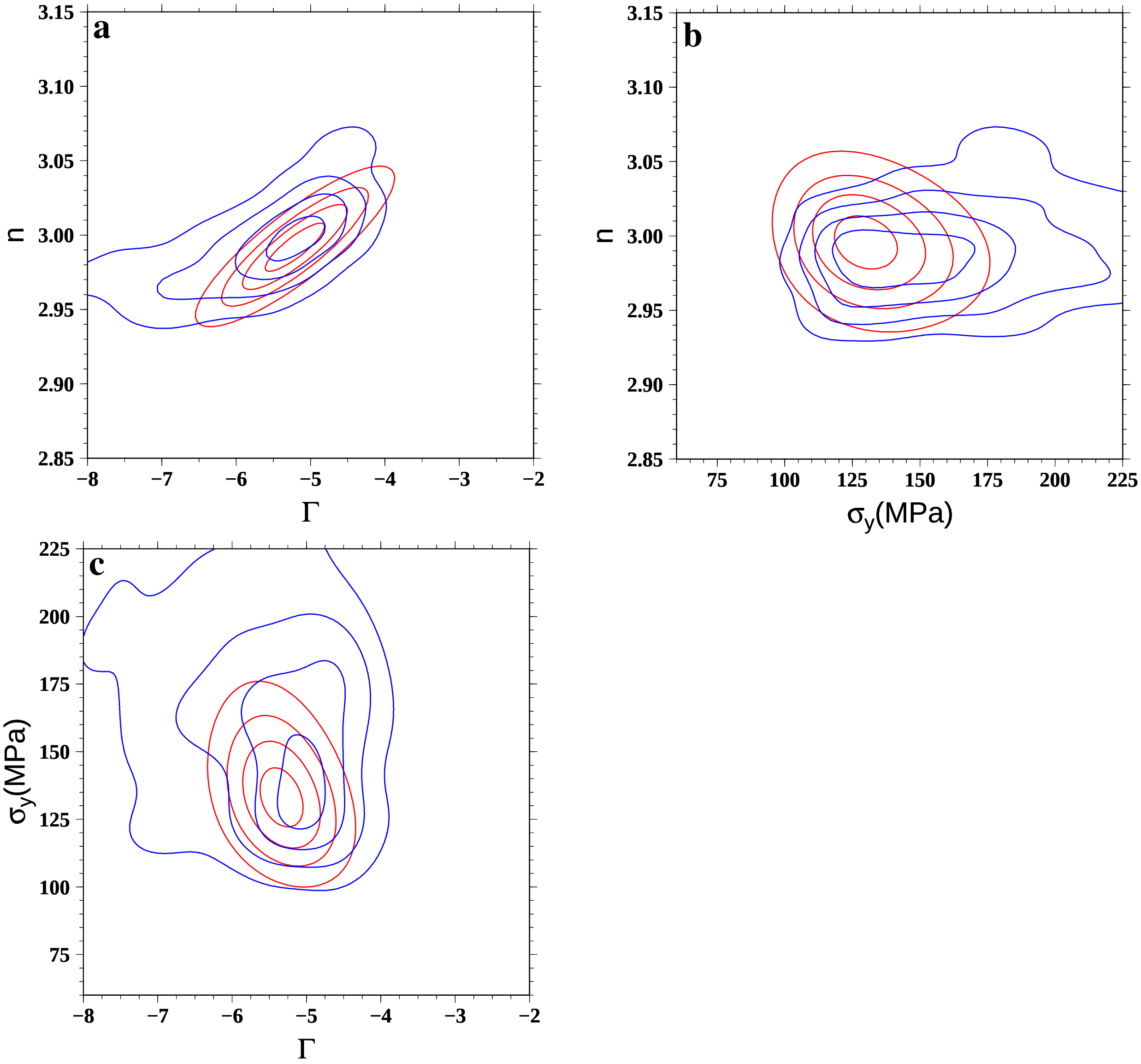

Figure 2.8: Comparison of two-dimensional marginal distributions for the unknown parameters n, Γ and σ_y. Contour lines (for 22%, 44%, 66%, 88%) for the marginals from the Gaussian approximation of the posterior distribution are shown in red. Contour lines for the marginals of the true postrior distribution, obtained from an MCMC sampling approach are shown in blue. (a) Marginals distributions for Γ vs. n (b) Marginal Distributions for σ_y vs. n (c) Marginal distributions for Γ vs. σ_y.

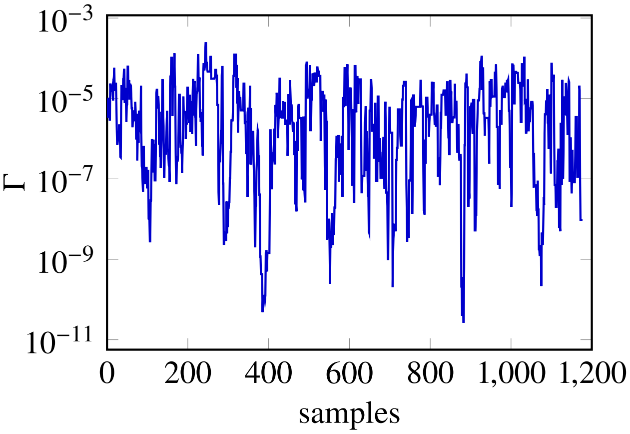

Figure 2.9: Chain history for weak zone factor Γ.

are $\tau_\Gamma = 7.46, \tau_{\sigma_y} = 4.68, \tau_n = 8.18$. The autocorrelation provides an estimate of the statistical dependence of the samples in the chain. It indicates that about every 5–8th sample in our chain is statistically independent (Robert and Casella, 2004). The autocorrelation times should be small (as they are here) so that there are large mean squared jumps, indicating effective mixing and a well sampled posterior distribution.

Next, we qualitatively compare the contours of the two-dimensional marginals of the Gaussian approximation and the posterior distributions (Fig. 2.8). Note that the approximation is reasonable, since the most important tradeoffs and correlations found in the posterior and its Gaussian approximation coincide. Compared to the conditionals, however, the difference between the Gaussian approximation of the posterior distribution and the posterior distribution is more pronounced. As to be expected, the marginal of the MAP point does not always coincide with the most likely point of the two-dimensional marginal. Like the conditionals, the marginals show a positive correlation between Γ and n (Fig. 2.8a). In all cases, the shifts in the actual distributions away from the Gaussian distributions are caused by (the lack of) yielding for large values of σ_y.

2.8 Discussion and Conclusions

In model problems, we have shown that nonlinear constitutive parameters and individual coupling factors between subducting and over riding plates can be inferred along with estimates of uncertainty and the tradeoffs between them. Although idealized, the forward models are functionally equivalent to existing highly resolved (1-km where needed) global models (Stadler et al., 2010; Alisic, Gurnis, Stadler, Burstedde, Wilcox, et al., 2010; Alisic, Gurnis, Stadler, Burstedde, and Ghattas, 2012), such that the methods developed here will be applicable to parameter inference with quantified uncertainties for the global mantle flow and plate motion problem. Our primary goal here is to discuss present results in terms of their applicability to the geophysical problem.

We use adjoint variables to efficiently compute first and second derivatives of the negative log likelihood function. This requires the solution of the adjoint Stokes equations (2.18), which have an anisotropic viscosity but are linear in the adjoint variables. Due to the self-adjointness of the Stokes equations, this adjoint operator coincides with the linear operator required in the Newton method. Hence, a forward nonlinear Stokes solver for (2.1) based on a Newton method is already equipped with the operator needed to solve the adjoint Stokes problem and only the computation of the adjoint system right hand side must be implemented additionally. Note that the computation of the gradient using adjoints requires a *single* linear (adjoint) solve *independently* of the number of parameters.

As an alternative to computing derivatives through adjoints, finite differentiating for the parameters can be used. In the present problem, this amounts to solving a *nonlinear* Stokes equation *for each parameter* to compute the gradient. While for the small number (at most five) of parameters considered in this paper this finite difference approach is certainly practicable, it becomes infeasible for problems with a larger number of parameters, or for problems where a (discretized) parameter field is inferred. Here, we have employed finite differences to verify the implementation of the adjoint-based derivatives.

We described two regimes of subduction-driven plate motion, a sensitive and an insensitive regime, determined from the change in plate motion with respect to coupling factors (e.g., Fig. 2.2), a relationship known for some time (King and Hager, 1990). The distinction between these regimes became evident through individual inversions where we found that the uncertainty was minimized in the sensitive regime and increased with both larger and smaller coupling factors (in the insensitive regime). This suggests that in a global inversion, like in the 2-D test problem, recovery of coupling factors between plate pairs within the sensitive regime should be better determined than factors at plate margins which are either fully uncoupled or fully coupled. It must be emphasized that there will be global interaction between the coupling factors.

The MAP point accurately recovers the coupling factors for each plate boundary in problems where we either assume that the parameters acting over the entire domain (a strain rate exponent and yield stress) are known or when these parameters are inferred simultaneously. The question arising for the global geophysical inversion is whether coupling factors can be inferred in a relative sense (for example, Chile is five times more coupled than the Marianas) or an absolute sense (for example, Chile has a stress of 100 MPa while the value for the Marianas is less than 20 MPa). The method looks promising in both regards. In cases when the plates are not yielding away from plate boundaries, the relative order of plate coupling and their absolute values are recoverable (e.g., Fig. 2.4a-c). We found that the inferred MAP values were insensitive to how we choose the initial guess for the inversion, that is by using larger or smaller constant guesses than the actual values lead to the correct inference of the relative degree of coupling and absolute values of plate coupling. If prior knowledge on either the strain rate exponent or yield stress are added—either by eliminating the parameters from the inversion or by using a smaller variance on the prior—the coupling factors are better constrained. In a global inversion, we could find that the use of a single, constant yield stress might be limiting and disguises the variability in the degree of yielding between subduction zones, perhaps reflected in variable strengths inferred for the bending oceanic lithosphere (Arredondo and Billen, 2012). In other words, variability that actually occurs from one bending plate to another (due say to different plate strengths) could be mapped into coupling coefficients. This should be a small effect in a global inversion that uses detailed prior constraints on the thickness of plates, as incorprated into present forward models (Stadler et al., 2010; Alisic, Gurnis, Stadler, Burstedde, Wilcox, et al., 2010; Alisic, Gurnis, Stadler, Burstedde, and Ghattas, 2012).

Moreover, as only an instantaneous Stokes flow model is used, this approach could hide the possibility that the development of weakening within a bending plate is a cumulative and not an instantaneous phenomenon. There is nothing inherent in the adjoint-based inference approach that enforces the recovery of only a single, global strain rate exponent n, but our suspicion is that we do not yet have data constraints to sufficiently constrain variations in n. The strain rate exponent, as well as other constitutive parameters may also be variable due to putative variations in major element composition or water content.

How the surface velocity data is used as constraints has an important influence on how close the inverted MAP estimate is to the true parameters, and also influences the tradeoffs between parameters. If the horizontal velocity field along the entire surface is used, a complete recovery is possible for the globally acting parameters (yield stress and strain rate exponent) and local parameters (coupling factors). This finding is consistent with the results in Worthen et al. (2014) who attempted to recover spatially variable parameters in a nonlinear constitutive relationship. Although in this study and in Worthen et al. (2014) only the lateral component(s) of the velocity vector along the top are used, this surface velocity field contains powerful information on the absolute value of plate motions and how rapidly and over what length scales plates are deforming. This is particularly useful to constrain the internal deformation of the bending plate. Unfortunately, such pointwise velocity data does not uniformly exist globally, and where is does, for example over continental margins (from dense networks of continuous GPS-stations), the velocity vectors reflect a combination of co- and post-seismic transients and long-term deformation over and adjacent to plate boundaries (Wells and McCaffrey, 2013; McCaffrey et al., 2013). Below, we discuss how such data could be used in a geophysical inversion. Our new study here deviates from Worthen et al. (2014) in that we use limited and piecewise constant plate velocity data, making this study closer to a global problem in which mostly rigid plate motion data are available.

Available plate motion data has passed through a plate motion inversion (Argus and Gordon, 1991) such that there is no strain within the plates. Our inversion needs to be sufficiently flexible so as not to impose the length scale or degree of deformation near plate margins, which we have attempted by limiting (in our standard case) to constant velocities from data only over about 80% of the surface within plate interiors. We find that by restricting an inversion to only this data, we are able to recover all of the uncertain parameters to nearly the same degree as when we use the full set of data (for example, compare Cases IX and XI in Table 2.2). This high degree of recovery was achieved when the plates were essentially rigid within their interiors, which is generally a good assumption for most plates. If the plates are not rigid, then we find a strong tradeoff between the coupling factors and the parameters governing the nonlinearity over the entire model domain. Determining the correct stencil, e.g. the area over which plate motion data are prescribed, will be important because some plates, especially the Indian Plate, have present-day internal, but diffuse, deformation (Gordon and Stein, 1992; Gordon, DeMets, et al., 1998). Based on the 2-D test problems, if we assume that the entire Indian plate were rigid, then we suspect that we would infer incorrect coupling factors or yield stress.

More extreme levels of plate deformation occur closer to plate margins usually within continental areas, such as the Himalayas, Andes, and western North America. In the latter region, plate deformation is particularly well constrained from continuous GPS data, and shows a mixture of distributed deformation associated with plate divergence, transcurrent motion and plate convergence (C. W. Kreemer et al., 2012). In some 2-D test inverse models, we approximated a plate margin, otherwise deforming over a length scale of several hundred kilometers, with a single constant velocity (akin to a single Euler pole). In such cases, a strong tradeoff was found between the inferred coupling factors, both for the adjacent margin and more distant margins, and the degree of yielding through the entire domain. There are likely to be at least two ways of addressing this tradeoff in a geophysical inference. First, one could avoid constraining the deforming areas entirely by using a tailored stencil that avoids the deforming areas. Here we should be able to recover the yield stress and strain rate exponent as well as the coupling factors for most plate margins. Another direction would be to attempt an inverse model which combines the recovery of the discrete parameters corresponding to the rigid motion of the plate interiors, as we have done here, with a recovery of a continuous field, like effective viscosity (Worthen et al., 2014). This latter method would benefit from the use of distributed velocity constraints. It may now be possible to use such data for western North America using the results of studies which have attempted to deconvolve the short term cycling associated with co- and post-seismic phenomena from long term deformation (Wells and McCaffrey, 2013; McCaffrey et al., 2013).

In global inversions, the ratio between the number of parameters and the number of independent observations will influence the degree of ill-posedness of the inversion, and it will influence the importance of incorporating prior knowledge for the parameters. The observational data will consist of Euler poles for both major plates, like the Pacific Plate, and minor plates, such as those that make up back-arc basins; consequently we would expect about 12–20 mostly independent observations in a global inversion that was like the test cases described here. Additionally, one could incorporate topography of oceanic trenches, essentially regionally distributed data, that would add to the amount of available observations. This, however, would require some modification to (2.18) and (2.19). The uncertain parameters will primarily be the coupling factors for each of the major subductions zones, as well as a small number of globally defined constitutive parameters, which could add up to overall about 20–30 inversion parameters. Note that the nonlinearity of the parameter-to-observable map makes it difficult to use the number of parameters and observations directly to judge if the problem is over- or under-determined—this is the case even if the prior and noise covariance operators are diagonal.

By comparing conditional and marginal distributions, we have observed that Gaussian approximations of the posterior parameter distribution based on the Hessian of the negative log posterior, are useful approximations of the true posteriors, which we explored using MCMC sampling. For global geodynamics inversions, each model evaluation requires significant computational resources and, thus, sampling-based methods, which can require tens of thousands of forward solves even for a moderate number of parameters (Baumann et al., 2014), are out of the question. For these problems, a Hessian-based approximation that uses adjoints to compute derivatives is an attractive option to study tradeoffs and the interplay between parameters. In particular, Gaussian approximations to conditional and marginal distributions will be important for inversions in global, highly resolved mantle flow models, for instance in the inversion of plate coupling between different subduction zones, which can provide an explanation of how one subduction zone influences another one.

2.9 Acknowledgments

Supported by the National Science Foundation through EAR-1247022, EAR-1118239, and CMMI-1028978. We thank Noemi Petra and Johann Rudi for valuable discussions.

.1 Integration of viscosity bounds in rheology

The classical Newton method requires continuous differentiability of the nonlinear equation it is applied to. Thus, we incorporate the viscosity bounds into the strain-rate weakening viscosity such that the map from the second invariant of the strain rate (and thus from the velocity) to the stress tensor is differentiable. We do so by choosing the shift d in (2.5) appropriately. The strain rate $\hat{\dot{\varepsilon}}_{\mathrm{II}}$, where the upper viscosity bound $\eta_{\max}$ becomes active is characterized by

$$\eta_{\max}\dot{\boldsymbol{\varepsilon}}(\boldsymbol{u}) = a(T)(\dot{\varepsilon}_{\mathrm{II}} - d)^{\frac{1}{2n}}\dot{\varepsilon}_{\mathrm{II}}^{-\frac{1}{2}}\dot{\boldsymbol{\varepsilon}}(\boldsymbol{u}),$$

which implies that

$$\eta_{\max}\hat{\dot{\varepsilon}}_{\mathrm{II}}^{\frac{1}{2}} = a(T)(\hat{\dot{\varepsilon}}_{\mathrm{II}} - d)^{\frac{1}{2n}}. \tag{22}$$

Solving for the shift d, this results in

$$d = \hat{\dot{\varepsilon}}_{\mathrm{II}} - \left(\frac{\eta_{\max}}{a(T)}\right)^{2n}\hat{\dot{\varepsilon}}_{\mathrm{II}}^{n}. \tag{23}$$

To ensure differentiability of the stress tensor with respect to the second invariant of the strain rate, we will choose the shift d such that the first derivatives of both sides in (22) coincide at $\hat{\dot{\varepsilon}}_{\mathrm{II}}$, i.e.,

$$\frac{1}{2}\eta_{\max}\hat{\dot{\varepsilon}}_{\mathrm{II}}^{-\frac{1}{2}} = a(T)\frac{1}{2n}(\hat{\dot{\varepsilon}}_{\mathrm{II}} - d)^{\frac{1-2n}{2n}}.$$

Using (22), this implies that

$$\hat{\dot{\varepsilon}}_{\mathrm{II}}^{-1} = \frac{1}{n}(\hat{\dot{\varepsilon}}_{\mathrm{II}} - d)^{-1},$$

and thus necessarily that $\hat{\dot{\varepsilon}}_{\mathrm{II}} \geq d$. Hence,

$$d = \frac{n-1}{n}\hat{\dot{\varepsilon}}_{\mathrm{II}}. \tag{24}$$

Substituting d from (23) into (24) yields

$$\left(\frac{\eta_{\max}}{a(T)}\right)^{2n}\hat{\dot{\varepsilon}}_{\mathrm{II}}^{n} = \frac{1}{n}\hat{\dot{\varepsilon}}_{\mathrm{II}},$$

resulting in

$$\hat{\dot{\varepsilon}}_{\mathrm{II}} = n^{\frac{1}{1-n}}\left(\frac{\eta_{\max}}{a(T)}\right)^{\frac{2n}{1-n}} \tag{25}$$

Substituting $\hat{\dot{\varepsilon}}_{\mathrm{II}}$ into (23) gives the desired expression for d, which is independent of the strain rate:

$$d = (n-1)n^{\frac{n}{1-n}}\left(\frac{\eta_{\max}}{a(T)}\right)^{\frac{2n}{1-n}}.$$

Chapter 3

THE INVERSE OF MANTLE FLOW WITH VELOCITY AND TOPOGRAPHY CONSTRAINTS

ABSTRACT

Constraining rheological parameters of the mantle is essential for not only estimating the broad-scale forces driving mantle flow, but also for estimating shear and normal stresses at plate boundaries. Inferring constitutive parameters requires minimizing a misfit between model output and observations, such as plate motions. However, as a constraint, plate velocities, sensitive to reference frames and an assumption of plate rigidity, are limiting and some form of surface deformation data needs to be incorporated into a misfit to better infer plate coupling. Dynamic topography, vertical deformation at the surface, such as oceanic trench topography, aids in partially overcoming this limitation. We formulate the cost function and derive the adjoint system with surface velocity and dynamic topography as joint constraints. We derive the adjoint forcing term with surface velocity and surface normal stress. We analyze the simple case of a sinking mass while inferring rheological parameters (layer prefactors, strain rate exponent and activation energy) and then discuss the advantages and limitations of the method in reference to subduction zones.

3.1 Introduction

Slab pull is likely the primary force driving plate motions (Forsyth and Uyeda, 1975; Chapple and Tullis, 1977) and is estimated to account for approximately 70% of this force (Conrad and Lithgow-Bertelloni, 2002). An important target for models is reproducing the asymmetric motion at subduction zones, a phenomena which is particularly sensitive to rheology and coupling of plates to the surface. Without strong coupling of slabs to the subducting plate, convergence at subduction zones would be symmetrical (Conrad and Lithgow-Bertelloni, 2002). While slab pull is the dominant force, ridge push can be consequential as it acts as a 'push force'. Key resisting forces include a bending subduction and plate motions include the bending of slabs when they first subduct and the frictional resistance from faults. Slabs may act as stress-guides (Stadler et al., 2010), allowing stresses to propagate from the lower mantle to the oceanic lithosphere; as stress guides slabs can both couple in additional resistance and driving to the plates. Nevertheless, the degree to which slabs are stronger compared to ambient mantle remains open.

Accurately estimating broad-scale forces requires models that contain the salient physics in addition to the necessary resolution to resolve the fine scale features of mantle flow. The correct rheology would incorporate shear thinning due to dislocation creep in the upper mantle (Karato and Wu, 1993) and dynamic weakening, which is controlled by the yield stress (Stadler et al., 2010; Alisic, Gurnis, Stadler, Burstedde, and Ghattas, 2012; Alisic, Gurnis, Stadler, Burstedde, Wilcox, et al., 2010; Billen and Hirth, 2007; Billen and Hirth, 2005). Each of the rheological parameters (strain rate exponent, yield stress and plate coupling), plays a key role in the amount of viscous dissipation in the mantle. Viscous dissipation occurs as plates overcome the bending force and is also tied to slab strength (weak slabs promote less dissipation compared to strong slabs).

In addition to a non-Newtonian rheology, thermal boundary layers, slabs and fault zones need to have the appropriate resolution. Properly resolving models needs requires either refining with a uniform mesh, which can be very costly, or using adaptive mesh refinement (AMR). Recently, with the use of adaptive mesh refinement (AMR), there have been spherical models that incorporate non-Newtonian rheology along with fine-scale resolution of fault zones and slabs (Stadler et al., 2010; Alisic, Gurnis, Stadler, Burstedde, and Ghattas, 2012) which can produce the complex motions of both large-scale and micro plates.

While high-resolution models with reasonable rheologies are important to constraining broad-scale forces, they still fall short due to a mismatch in predicted plate motion and observed motion. To minimize the misfit between models and observations requires solving an optimization problem with plate motion data (Ratnaswamy et al., 2015) where the constitutive parameters are inferred. When using plate motion data, model parameters such as the plate couplings, strain rate exponent and yield stress, can be constrained in an optimization. However, there is a limit to the amount of information that can be gleaned from plate motions (Ratnaswamy et al., 2015) due to sensitivity between rheological parameters and plate motion.

Using plate motion data can give limits on mantle rheology since there is a first order relationship between plate motions and the rheology. However, plate motion data is not unique with regard to reference frames (Gripp and Gordon, 1990; Argus, Gordon, and DeMets, 2011) and can potentially change the inference of parameters. A caveat of using plate motion data is the assumption of rigid plates, that is there is no deformation (strain rate is negligible), which implies that plate motion data cannot be used near trenches since there is significant deformation there (C. Kreemer et al., 2003). Using plate motion data can potentially lead to poorly constrained plate couplings (Ratnaswamy et al., 2015).

While plate motions fall short of fully constraining plate coupling, other observations such as dynamic topography, free-air gravity anomalies, and plate strain, might be useful. Dynamic topography, a key manifestation of convection, is correlated with density anomalies such as plumes and slabs (Hager, Clayton, et al., 1984), and at very long wavelengths, has an amplitude of about 1 km and positively correlates with the geoid, but is very wavelength dependent (Flament et al., 2013). Using dynamic topography as a constraint, studies have focus on minimizing the misfit between dynamic topography predictions and it's observational conterpart, residual topography (Yang and Gurnis, 2016).

Both the correct density distribution (of slabs) and the effective viscosity structure are both essential to constrain plate coupling factors. Consequently, the incorporation of both radial and lateral variations in viscosity is necessary reproccurately predict the dynamic topography (Moresi and Gurnis, 1996a; Kaufmann and Lambeck, 2000). There have been studies to constrain the short-wavelength signal at subduction zones and have done so by using a weak mantle wedge (Billen and Gurnis, 2001). Another way to have a weak upper mantle is to have shear thinning, where the the strain rate exponent controls how weak the (upper) mantle is (Karato and Wu, 1993); however, there have not been many studies using nonlinear, (well-resolved), models to constrain the dynamic topography. Recently, there have been advances in numerical solutions that incorporate rheology with the salient physics and they are able to produce they dynamic weakening at hinge zones and shear thinning in the upper mantle. However, with the correct physics, the mantle properties have not been constrained (Stadler et al., 2010; Alisic, Gurnis, Stadler, Burstedde, and Ghattas, 2012) which leads to data misfit in both plate motions and dynamic topography.

Strides have been made to methods meant to constrain mantle rheology using data in an optimization framework (Worthen et al., 2014; Ratnaswamy et al., 2015) to recover the rheological parameters. Plate motion helps to strongly constrain the rheology such as the strain rate exponent and yield stress; however, there is a limit as to how well the coupling between plates can be constrained (Ratnaswamy et al., 2015). Therefore, the incorporation of dynamic topography is an important constraint as it better reflects the surface deformation at trenches than plate motion. Constraining plate coupling with higher fidelity is important as these estimates can contribute to a better understanding of coupling and where great earthquakes occur (Scholz and Campos, 2012)

In this chapter, we will derive the adjoint system with plate velocities and surface normal stress data. We will implement this new adjoint systems for a simple test case of a sinking mass anomaly where there is a smooth surface normal stress signal. We will present examples of the recovery of the strain rate exponent,pre-exponent to the constitutive relation and activation energy. We will show that the gradients for this new adjoint formulation are consistent and can thus be used for consistent plate coupling inferences. Lastly, we will present the current limitation of applying this method to realistic subduction zone models.

3.2 Forward Model

Earlier (Chapter 2), we inferred global parameters in the rheological relationship for the mantle with an adjoint optimization in which the viscosity is defined as,

$$\eta(\dot{\varepsilon}_{\mathrm{II}}, \sigma_y) = \eta_{\mathrm{min}} + \min(\Gamma_i \min(\eta_{\mathrm{max}}, a(T)(\dot{\varepsilon}_{\mathrm{II}} - d)^{\frac{1}{2n}} \dot{\varepsilon}_{\mathrm{II}}^{-\frac{1}{2}}), \frac{1}{2}\sigma_y \dot{\varepsilon}_{\mathrm{II}}^{-\frac{1}{2}}) \qquad (3.1)$$

where η_{min} is the minimum effective viscosity, σ_y is the yield stress, $a(T)$ is the temperature dependent component of viscosity, n is the strain rate exponent and d is a parameter included to regularize the solution. While some of the parameters, weakfactor Γ, do not have physical units and arise in the geophysical problem, the parameters n and σ_y can be partially inferred from laboratory experiments(Korenaga and Karato, 2008). We assume that the flow is goverend by (3.2)

$$\begin{aligned} \nabla \cdot \boldsymbol{u} &= 0 \\ \nabla \cdot \boldsymbol{\sigma} &= -\mathrm{Ra}T \end{aligned} \tag{3.2}$$

with $\boldsymbol{\sigma} = 2\eta(\dot{\varepsilon}_{\mathrm{II}}, \Gamma, n, \sigma_y)\dot{\boldsymbol{\varepsilon}}) - p\mathbf{I}$, the stress tensor. Solving the equations of conservation of mass and momentum (3.2), yields the velocity and pressure distribution ($\boldsymbol{u}$, p). Solutions to (3.2) and allow us to compare model results to surface observables, namely surface velocities and the total normal stress, $\boldsymbol{\sigma}_{rr}$,

$$h = \frac{\boldsymbol{\sigma}_{rr}}{\rho g} \tag{3.3}$$

where h is the dynamic topography, g gravity, and ρ the density.

3.3 Bayesian Inverse Problem

With the addition of the cost function for surface normal stress, we can also formulate the Bayesian Inverse problem as:

$$\boldsymbol{\pi}_{\text{post}} \propto \boldsymbol{\pi}_{\text{likelihood}} \boldsymbol{\pi}_{\text{prior}} \tag{3.4}$$

with the likelihood distribution,

$$\begin{aligned} \boldsymbol{\pi}_{\text{likelihood}} \propto & \exp(-\mathcal{J}) \\ & \exp\{-\frac{1}{2}\int_{\Omega_1} (\boldsymbol{O}\boldsymbol{u} - \boldsymbol{u}_{\text{obs}})^T C_{vel}^{-1} (\boldsymbol{O}\boldsymbol{u} - \boldsymbol{u}_{\text{obs}}) d\Omega_1 \\ & + \frac{1}{2}\int_{\Omega_2} (\boldsymbol{O}\boldsymbol{\sigma}_n - \boldsymbol{\sigma}_{\text{obs}})^T C_{stress}^{-1} (\boldsymbol{O}\boldsymbol{\sigma} - \boldsymbol{\sigma}_{\text{obs}}) d\Omega_2\} \end{aligned} \tag{3.5}$$

while the prior distribution $\boldsymbol{\pi}_{\text{prior}}$ is

$$\boldsymbol{\pi}_{\text{prior}} \propto \exp\{-\frac{1}{2}(\boldsymbol{m} - \boldsymbol{m}_0)^T C_{\text{prior}}^{-1} (\boldsymbol{m} - \boldsymbol{m}_0)\}. \tag{3.6}$$

Typically, $\boldsymbol{m}_0$ is the mean value, usually chosen as a reasonable parameter value, while C_{prior}^{-1} is the covariance distribution of each parameter. In most cases (including the inversions presented in this chapter), the prior term is a Gaussian distribution due to the ease of drawing samples and the smoothness of the distribution. An important aspect of the likelihood model is the incorporation of noise in the data or,

$$\boldsymbol{f} = \boldsymbol{u}_{obs} + \mathcal{N}(0, C_{noise}) \tag{3.7}$$

where we assume a normal distribution for the noise in the data (zero mean and covariance C_{noise}). Our data misfit function will now include both plate velocities and surface normal stresses, with a cost function

$$\begin{aligned}
\mathcal{J}(\boldsymbol{u},\boldsymbol{m},p) &:= \mathcal{J}_{\boldsymbol{u}} + \mathcal{J}_{\sigma} \\
\mathcal{J}(\boldsymbol{u},\boldsymbol{m},p) &:= \frac{1}{2}\int_{\partial\Omega_1} (\mathcal{O}\boldsymbol{u} - \boldsymbol{u}_{\text{obs}})^T C_{vel}^{-1} (\mathcal{O}\boldsymbol{u} - \boldsymbol{u}_{\text{obs}}) d\partial\Omega_1 \\
&\quad + \frac{1}{2}\int_{\partial\Omega_2} (\mathcal{O}\boldsymbol{\sigma}_n - \boldsymbol{\sigma}_{\text{obs}})^T C_{stress}^{-1} (\mathcal{O}\boldsymbol{\sigma} - \boldsymbol{\sigma}_{\text{obs}}) d\partial\Omega_2
\end{aligned} \tag{3.8}$$

where first term on the right hand side is the surface velocities misfit as previously used in (Ratnaswamy et al., 2015). The cost function for the second term on the right hand side is for surface normal stress with $\boldsymbol{\sigma}_n = \mathbf{n}(\boldsymbol{\sigma}\mathbf{n})$ being the normal stress, and $\mathcal{O}$ is the observation operator ($\mathcal{O}$ retrieves the model observations at physical points in space). For our test problems, $\mathcal{O}$ is the same for $\boldsymbol{u}$ and σ_{rr}; however, this is not necessarily the case for geophysical problems, as they could be different.

We have shown that constraining plate motion can give a strong constraint on the rheological properties of the mantles such as the strain rate exponent, yield stress and plate couplings. However, the surface normal stress at trenches might provide refined estimates as velocity data was not included in the deforming regions near the trench. To constrain the rheological parameters, we first solve for the maximum a posteriori point (MAP) by solving the PDE-constrained optimization problem,

$$\min_{\boldsymbol{m}} \mathcal{J}(\boldsymbol{u},\boldsymbol{m},p) \tag{3.9}$$

subject to (3.2). We first construct the Lagrangian,

$$\begin{aligned}
\mathcal{L}(\boldsymbol{u},p,\boldsymbol{v},q,\boldsymbol{m}) = \mathcal{J}(\boldsymbol{u},\boldsymbol{m},p) &+ \int_{\Omega} 2\eta(\dot{\varepsilon}_{\text{II}},\Gamma,n,\sigma_y)\dot{\boldsymbol{\varepsilon}}(\boldsymbol{u}) : \dot{\boldsymbol{\varepsilon}}(\boldsymbol{v}) d\Omega \\
&+ \int_{\Omega} p\nabla\cdot\boldsymbol{v}d\Omega - \int_{\Omega} q\nabla\cdot\boldsymbol{u}d\Omega - \int_{\Omega} \text{Ra}T\mathbf{e}_r\cdot\boldsymbol{v}d\Omega.
\end{aligned} \tag{3.10}$$

Taking variations of (3.10) with respect to the adjoint variables ($\boldsymbol{v}$, q) recovers the forward problem, while derivatives with respect to the forward variables ($\boldsymbol{u}$,p) yields the adjoint equations,

$$\begin{aligned}
\nabla\cdot\boldsymbol{v} &= 0 \qquad \text{on } \Omega, \\
\nabla\cdot\hat{\boldsymbol{\sigma}}_{\boldsymbol{u}} &= 0 \qquad \text{on } \Omega,
\end{aligned} \tag{3.11}$$

with boundary conditions

$$\begin{aligned}
\boldsymbol{v}\cdot\mathbf{n} &= 0 \quad \text{on } \partial\Omega, \\
\mathbf{T}(\hat{\boldsymbol{\sigma}}_{\boldsymbol{u}}\mathbf{n}) &= \begin{cases} 0 & \text{on } \partial\Omega\setminus\partial\Omega_t, \\ -\mathcal{O}^T C_{\text{noise}}^{-1}(\mathcal{O}\boldsymbol{u} - \boldsymbol{u}_{\text{obs}}) & \text{on } \partial\Omega_t, \end{cases}
\end{aligned}$$

where $\hat{\boldsymbol{\sigma}}_{\boldsymbol{u}} = \hat{\boldsymbol{\sigma}}_{\boldsymbol{u}}(\boldsymbol{v}, q)$ is the adjoint stress tensor defined by

$$\hat{\boldsymbol{\sigma}}_{\boldsymbol{u}} = 2\Big(\eta(\dot{\varepsilon}_{\mathrm{II}}, \Gamma, n, \sigma_y)\mathbb{I} + \frac{1}{2}\eta_{,\dot{\varepsilon}_{\mathrm{II}}}[\dot{\boldsymbol{\varepsilon}}(\boldsymbol{u}) \otimes \dot{\boldsymbol{\varepsilon}}(\boldsymbol{u})]\Big)\dot{\boldsymbol{\varepsilon}}(\boldsymbol{v}) - q\mathbf{I} \tag{3.12}$$

with $\mathbb{I}$ being the fourth-order identity tensor, and $\eta_{,\dot{\varepsilon}_{\mathrm{II}}}$ given by

$$\eta_{,\dot{\varepsilon}_{\mathrm{II}}} = \begin{cases} \min\Big(0, \frac{1}{2}\Gamma a(T)(\dot{\varepsilon}_{\mathrm{II}} - d)^{\frac{1}{2n}}\dot{\varepsilon}_{\mathrm{II}}^{-\frac{1}{2}}\frac{\dot{\varepsilon}_{\mathrm{II}} - (\dot{\varepsilon}_{\mathrm{II}} - d)n}{\dot{\varepsilon}_{\mathrm{II}}(\dot{\varepsilon}_{\mathrm{II}} - d)n}\Big) & \text{in } \Omega \setminus \Omega_y \\ -\frac{1}{2}\sigma_y\dot{\varepsilon}_{\mathrm{II}}^{-\frac{3}{2}} & \text{in } \Omega_y. \end{cases} \tag{3.13}$$

Incorporating surface normal stress into the adjoint formulation requires taking variations of (3.14) with respect to ($\boldsymbol{u}$, p) would add an extra forcing term to the adjoint system since there is a misfit in surface normal stress that needs to be minimized.

$$\mathcal{J}_\sigma := \frac{1}{2}(O\boldsymbol{\sigma}_n - \boldsymbol{\sigma}_{obs})^T C_{topog}^{-1}(O\boldsymbol{\sigma}_n - \boldsymbol{\sigma}_n). \tag{3.14}$$

The derivative of (3.14) is

$$\frac{\partial \mathcal{J}_\sigma}{\partial(\boldsymbol{u}, p)} = O^T \frac{\partial \boldsymbol{\sigma}_n}{\partial(\boldsymbol{u}, p)}(O\boldsymbol{\sigma}_n - \boldsymbol{\sigma}_{obs}) \tag{3.15}$$

The gradient of (3.14) w.r.t. $\boldsymbol{u}$in a direction $\tilde{\boldsymbol{u}}$ is,

$$\begin{aligned} \frac{\partial \mathcal{J}_\sigma}{\partial \boldsymbol{u}}\tilde{\boldsymbol{u}} &= 2[\eta\dot{\boldsymbol{\varepsilon}}(\tilde{\boldsymbol{u}}) + \frac{\partial \eta}{\partial \boldsymbol{u}}\dot{\boldsymbol{\varepsilon}}(\boldsymbol{u})\tilde{\boldsymbol{u}}] \\ &= 2\Big(\eta(\dot{\varepsilon}_{\mathrm{II}}, \Gamma, n, \sigma_y)\mathbb{I} + \frac{1}{2}\eta_{,\dot{\varepsilon}_{\mathrm{II}}}[\dot{\boldsymbol{\varepsilon}}(\boldsymbol{u}) \otimes \dot{\boldsymbol{\varepsilon}}(\boldsymbol{u})]\Big)\dot{\boldsymbol{\varepsilon}}(\tilde{\boldsymbol{u}}) \end{aligned} \tag{3.16}$$

while the gradient of (3.14) w.r.t. the forward pressure (p) in the direction $\tilde{p}$ is,

$$\frac{\partial \mathcal{J}_\sigma}{\partial p}(\tilde{p}) = -\tilde{p}\mathbf{I} \tag{3.17}$$

and

$$\frac{\partial \mathcal{J}_\sigma}{\partial(\boldsymbol{u}, p)}(\tilde{\boldsymbol{u}}, \tilde{p}) = 2\Big(\eta(\dot{\varepsilon}_{\mathrm{II}}, \Gamma, n, \sigma_y)\mathbb{I} + \frac{1}{2}\eta_{,\dot{\varepsilon}_{\mathrm{II}}}[\dot{\boldsymbol{\varepsilon}}(\boldsymbol{u}) \otimes \dot{\boldsymbol{\varepsilon}}(\boldsymbol{u})]\Big)\dot{\boldsymbol{\varepsilon}}(\tilde{\boldsymbol{u}}) - \mathbf{I}\tilde{p} \tag{3.18}$$

We will make use of the following identities:

$$\begin{gathered} \mathbb{I} \cdot \mathbf{n} = \mathbf{n} \\ \mathbf{n}(\mathbb{I} \cdot \mathbf{n}) = \mathbf{n} \cdot \mathbf{n} \\ (\mathbf{A} \otimes \mathbf{B})\mathbf{n} = \mathbf{A}(\mathbf{B}\mathbf{n}) \\ \mathbf{n}(\mathbf{A} \otimes \mathbf{B})\mathbf{n} = (\mathbf{n}\mathbf{A}) \cdot (\mathbf{B}\mathbf{n}) \end{gathered} \tag{3.19}$$

where $\mathbb{I}$ is the fourth order Identity tensor, **A and B** are second order tensors and $\mathbf{n}$ is a vector. Thus, $\mathbf{n}\frac{\partial \sigma}{\partial \boldsymbol{u},p}\mathbf{n}$ is,

$$\begin{aligned} \mathbf{n}\frac{\partial \boldsymbol{\sigma}}{\partial \boldsymbol{u},p}\mathbf{n} &= \mathbf{n}[2\Big(\eta(\dot{\varepsilon}_{\mathrm{II}},\Gamma,n,\sigma_y)\mathbb{I} + \frac{1}{2}\eta_{,\dot{\varepsilon}_{\mathrm{II}}}[\dot{\boldsymbol{\varepsilon}}(\boldsymbol{u})\otimes\dot{\boldsymbol{\varepsilon}}(\boldsymbol{u})]\Big) - \mathbf{I}]\mathbf{n} \\ &= 2\Big(\eta(\dot{\varepsilon}_{\mathrm{II}},\Gamma,n,\sigma_y)\mathbf{n}\cdot\mathbf{n} + \frac{1}{2}\eta_{,\dot{\varepsilon}_{\mathrm{II}}}\mathbf{n}[\dot{\boldsymbol{\varepsilon}}(\boldsymbol{u})\otimes\dot{\boldsymbol{\varepsilon}}(\boldsymbol{u})]\mathbf{n}\Big) - \mathbf{n}\cdot\mathbf{n} \\ &= 2\Big(\eta(\dot{\varepsilon}_{\mathrm{II}},\Gamma,n,\sigma_y)\mathbf{n}\cdot\mathbf{n} + \frac{1}{2}\eta_{,\dot{\varepsilon}_{\mathrm{II}}}(\mathbf{n}\dot{\boldsymbol{\varepsilon}}(\boldsymbol{u}))\cdot(\dot{\boldsymbol{\varepsilon}}(\boldsymbol{u})\mathbf{n})\Big) - \mathbf{n}\cdot\mathbf{n} \\ &= 2\Big([\eta(\dot{\varepsilon}_{\mathrm{II}},\Gamma,n,\sigma_y) - \frac{1}{2}]\mathbf{n}\cdot\mathbf{n} + \frac{1}{2}\eta_{,\dot{\varepsilon}_{\mathrm{II}}}(\mathbf{n}\dot{\boldsymbol{\varepsilon}}(\boldsymbol{u}))\cdot(\dot{\boldsymbol{\varepsilon}}(\boldsymbol{u})\mathbf{n})\Big) \end{aligned} \tag{3.20}$$

Note, $\mathbf{n}\frac{\partial \sigma}{\partial \boldsymbol{u},p}\mathbf{n}$ is a 0^{th} order tensor (scalar). Therefore the adjoint with the misfit in surface normal stresses is,

$$\begin{aligned} \boldsymbol{v}\cdot\mathbf{n} &= 0 \quad \text{on } \partial\Omega, \\ \mathbf{T}(\hat{\boldsymbol{\sigma}}_{\boldsymbol{u}}\mathbf{n}) &= \begin{cases} 0 & \text{on } \partial\Omega\setminus\partial\Omega_t, \\ -O^T C_{\text{noise}}^{-1}(O\boldsymbol{u} - \boldsymbol{u}_{\text{obs}}) & \text{on } \partial\Omega_t, \end{cases} \\ \mathbf{n}(\hat{\boldsymbol{\sigma}}_{\boldsymbol{u}}\mathbf{n}) &= \begin{cases} 0 & \text{on } \partial\Omega\setminus\partial\Omega_t, \\ -O^T C_{noise}^{-1}\mathbf{n}\frac{\partial\boldsymbol{\sigma}}{\partial(\boldsymbol{u},p)}\mathbf{n}(O\boldsymbol{\sigma}_n - \boldsymbol{\sigma}_{obs}) & \text{on } \partial\Omega_t, \end{cases} \end{aligned}$$

With the addition of of the misfit in the surface normal stresses, we now have an additional contribution to the gradient with the misfit in the surface velocities.

$$\mathcal{G}(\boldsymbol{m})_i = \int_\Omega 2\eta_{,i}(\dot{\varepsilon}_{\mathrm{II}},\Gamma,n,\sigma_y)\dot{\boldsymbol{\varepsilon}}(\boldsymbol{u}) : \dot{\boldsymbol{\varepsilon}}(\boldsymbol{v})d\Omega + \int_{\partial\Omega} O^T C_{noise}^{-1}\mathbf{n}\frac{\partial\boldsymbol{\sigma}}{\partial\boldsymbol{m}_i}\mathbf{n}(O\boldsymbol{\sigma}_n - \boldsymbol{\sigma}_{obs}), \tag{3.21}$$

where $\boldsymbol{m} = \log(\Gamma)$

$$\eta_{,i}(\dot{\varepsilon}_{\mathrm{II}},\Gamma,n,\sigma_y) = \min(\Gamma_i\chi_i\min(\eta_{\max}, a(T)(\dot{\varepsilon}_{\mathrm{II}} - d)^{\frac{1}{2n}}\dot{\varepsilon}_{\mathrm{II}}^{-\frac{1}{2}}), 0) \tag{3.22}$$

while $\boldsymbol{m} = \log(n)$ is given by,

$$\eta_{,i}(\dot{\varepsilon}_{\mathrm{II}},\Gamma,n,\sigma_y) = \begin{cases} \Gamma a(T)\omega(\dot{\varepsilon}_{\mathrm{II}} - d)^{\frac{1}{2n}}\dot{\varepsilon}_{\mathrm{II}}^{-\frac{1}{2}} & \text{in } \Omega_w, \\ 0 & \text{in } \Omega\setminus\Omega_w, \end{cases}$$

where $\omega = \log((\dot{\varepsilon}_{\mathrm{II}} - d)^{-\frac{1}{2n^2}})$. The derivative corresponding to the yield stress is,

$$\eta_{,i}(\dot{\varepsilon}_{\mathrm{II}},\Gamma,n,\sigma_y) = \min(0, \frac{1}{2}\sigma_y\dot{\varepsilon}_{\mathrm{II}}^{-\frac{1}{2}}). \tag{3.23}$$

For the contribution from the dynamic topography (namely the total surface normal stresses), we need the derivative, $\frac{\partial \boldsymbol{\sigma}}{\partial \boldsymbol{m}}$ given below.

$$\frac{\partial \boldsymbol{\sigma}}{\partial \boldsymbol{m}} = 2\eta_{,i}(\dot{\varepsilon}_{\mathrm{II}}, n, \Gamma, \sigma_y)\dot{\boldsymbol{\varepsilon}}(\boldsymbol{u}) \tag{3.24}$$

where $\eta_{,i}(\dot{\varepsilon}_{\mathrm{II}}, n, \Gamma, \sigma_y)$ is given in (3.31) to (3.32). Furthermore,

$$\mathbf{n}\frac{\partial \boldsymbol{\sigma}}{\partial \boldsymbol{m}}\mathbf{n} = 2\eta_{,i}(\dot{\varepsilon}_{\mathrm{II}}, n, \Gamma, \sigma_y)\mathbf{n}(\dot{\boldsymbol{\varepsilon}}(\boldsymbol{u})\mathbf{n}) \tag{3.25}$$

Previously, we computed the Gauss-Newton version of the Hessian of the misfit. We will formally derive the Hessian system, which involves taking the second order variations with respect to the Lagrangian, using the surface velocities (plate motion data) and surface normal stresses. The Hessian system is given,

$$\mathcal{H} = \begin{bmatrix} \mathcal{L}_{\boldsymbol{uu}} & \mathcal{L}_{\boldsymbol{um}} & \mathcal{L}_{\boldsymbol{uv}} \\ \mathcal{L}_{\boldsymbol{mu}} & \mathcal{L}_{\boldsymbol{mm}} & \mathcal{L}_{\boldsymbol{mv}} \\ \mathcal{L}_{\boldsymbol{vu}} & \mathcal{L}_{\boldsymbol{vm}} & 0 \end{bmatrix} \tag{3.26}$$

To solve the incremental forward equations, we look at the third (last row). The first term is formally the adjoint operator. The strong form of the adjoint equatoin is

$$\begin{aligned} \nabla \cdot \boldsymbol{u} &= 0 \\ \nabla \cdot \boldsymbol{\sigma}_u &= -\nabla \cdot \tau_u \end{aligned} \tag{3.27}$$

The incremental adjoint equations is given by solving the first row of the Hessian,

$$\begin{aligned} \nabla \cdot \boldsymbol{v} &= 0 \\ \nabla \cdot \boldsymbol{\sigma}_v &= -\nabla \cdot \Psi \end{aligned} \tag{3.28}$$

with BC's,

$$\begin{aligned} \tilde{\boldsymbol{v}} &= 0 \\ \mathbf{T}\boldsymbol{\sigma}_{\boldsymbol{u}}\mathbf{n} &= -\mathcal{O}^T C_{\text{noise}}^{-1}\mathcal{O}\tilde{u} - \mathbf{T}(\Psi\mathbf{n}) \end{aligned} \tag{3.29}$$

The action of the Hessian on a direction $\tilde{\boldsymbol{m}}$ is

$$\mathcal{H}\tilde{\boldsymbol{m}} = 2\eta_{,\text{ßß}}[\dot{\boldsymbol{\varepsilon}}(\boldsymbol{u})\dot{\boldsymbol{\varepsilon}}(\boldsymbol{v}) + \dot{\boldsymbol{\varepsilon}}(\boldsymbol{u})\dot{\boldsymbol{\varepsilon}}(\tilde{\boldsymbol{v}}) + \dot{\boldsymbol{\varepsilon}}(\tilde{\boldsymbol{u}})\dot{\boldsymbol{\varepsilon}}(\boldsymbol{v})]\tilde{\boldsymbol{m}} \tag{3.30}$$

where $\boldsymbol{m} = \log(\Gamma)$

$$\eta_{,i}(\dot{\varepsilon}_{\text{II}}, \Gamma, n, \sigma_y) = \min(\Gamma_i \chi_i \min(\eta_{\max}, a(T)(\dot{\varepsilon}_{\text{II}} - d)^{\frac{1}{2n}} \dot{\varepsilon}_{\text{II}}^{-\frac{1}{2}}), 0) \tag{3.31}$$

while $\boldsymbol{m} = \log(n)$ is given by,

$$\eta_{,i}(\dot{\varepsilon}_{\text{II}}, \Gamma, n, \sigma_y) = \begin{cases} \Gamma a(T)[\omega_1^2 + \omega_2](\dot{\varepsilon}_{\text{II}} - d)^{\frac{1}{2n}} \dot{\varepsilon}_{\text{II}}^{-\frac{1}{2}} & \text{in } \Omega_w, \\ 0 & \text{in } \Omega \setminus \Omega_w, \end{cases}$$

where $\omega_1 = \log((\dot{\varepsilon}_{\text{II}} - d)^{-\frac{1}{2n}})$ and $\omega_2 = \log((\dot{\varepsilon}_{\text{II}} - d)^{\frac{1}{2n}})$. The derivative corresponding to the yield stress is,

$$\eta_{,i}(\dot{\varepsilon}_{\text{II}}, \Gamma, n, \sigma_y) = \min(0, \frac{1}{2}\sigma_y \dot{\varepsilon}_{\text{II}}^{-\frac{1}{2}}). \tag{3.32}$$

3.4 Model Setup

We consider a simple system with a sinking thermal anomaly (Fig.3.1A); with a forward solution of the equations, we find the surface velocity and normal stress along the top boundary (Fig.3.1B). The predicted forward velocity and topography, with the addition of noise (4%) is used as "data" in the inverse method. The forward and inverse models both use temperature- and strain-dependent viscoity, however, it lacks dynamic weakening because we do not include plates idealized as thermal boundary layers. An advantage of not using a subduction zone model is the smoothness of the surface normal stress that is normally not present at the trenches.

We will solve the forward problem using a finite element code that is highly scalable that makes use of adaptive mesh refinement (AMR) (Rudi et al., 2015). Furthermore, we use Q2 elements for velocity while using first order discontinuous elements for pressure, to solve the Stokes flow problem.

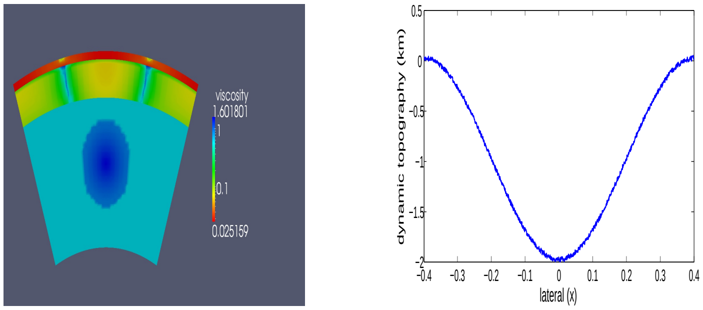

Figure 3.1: (a)Effective viscosity (b)Dynamic topography (km) with 4 % noise

3.5 Results

For the inversions, we investigate how well we can recover the parameters with a combination of surface normal stress data and surface velocity shown in Table 4.5.

To test how well the new adjoint formulation of surface normal stress data works with respect to the recovery of the rheological parameters, we first focus on a single parameter, (weak layer prefactor, strain rate exponent). In Case 1, we infer the weakfactor of the top layer of the system, while keeping the other parameters fixed (strain rate exponent, yield stress and activation energy). We find that we are able to infer the correct weak layer prefactor within 2 iterations. Furthermore, we test the independence of the initial guess to see if the inferred parameter is the same in Case 2. We find, similar to Case 1, that the recovered weak factor is 10^{-1}, while the convergence to the true (synthetic value) is also 2 iterations (Fig.3.2a), suggesting that the physics of the system prefers this weakfactor.

We repeat similar case studies for the strain rate exponent, and activation energy. In Case 3, we keep the weak factor and activation energy fixed (effectively conditioning on the weak factor and activation energy), and find that we infer the correct strain rate exponent of 3.0 within 3 iterations, similar to the weafactor in Cases 1-2. Similarly, we test the independence of the initial guess of the strain rate exponent. We test two different guesses ($n = 2.0, 3.5$) that are smaller and larger than the initial guess of Case 3, and find in both Cases 4 and 5 that we can recover the true strain rate exponent within 3-4 iterations (Fig.3.2b), also suggesting that this particular model has a preferential amount of shear thinning needed to constrain the surface normal stress signal.

A parameter that we have not investigated in (Ratnaswamy et al., 2015) was the activation energy, which controls the amount of temperature dependence in the effective viscosity. We similarly follows the similar approach as we did for the weak factor and strain rate exponent (Cases 1-5) and infer the activation energy (as well as the independence) of that initial guess. We find in Case 6 (only inferring the activation energy), that we are able to infer the activation energy, regardless of the in initial guess (Case 7) within 4 iterations (Fig.3.2c).

While we were able to accurately infer the rheological parameters by themselves, it is important that we see how well this new adjoint formulation does when it comes to inferring multiple parameters using only surface normal stress data. We do so in Case 9 where we infer the strain rate exponent, activation energy and weakfactor and find that we can infer all three parameters within 7 iterations, which possibly

Table 3.1: Case study summary for inversions for multiple parameters with different pieces of data used. Note *T* means topography, while *v* means velocity data used.

Case	n (Guess/Recov.)	γ (Guess/Recov.)	Activ. Energy (Guess/Recov.)	Iter.	Data
1	3.0	$10^{-2}/10^{-1}$	1.0	2	T
2	3.0	$10^{-3}/10^{-1}$	1.0	2	T
3	2.85/3.0	10^{-1}	1.0	3	T
4	2.0/3.0	10^{-1}	1.0	5	T
5	3.5/3.0	10^{-1}	1.0	3	T
6	3.0	10^{-1}	0.1/1.0	4	T
7	3.0	10^{-1}	0.4/1.0	4	T
8	2.0/3.0	$10^{-3}/10^{-1}$	0.1/1.0	3	T
9	2.8/3.0	10^{-1}	1.0	3	T & v
10	3.0	$10^{-2}/10^{-1}$	1.0	3	T & v
11	3.0	10^{-1}	0.1/1.0	3	T & v
12	2.0/3.0	$10^{-3}/10^{-1}$	1.0	3	T & v
13	2.0/3.0	$10^{-3}/10^{-1}$	0.1/1.0	3	T & v

shows that as more parameters are inferred, the rate of convergence increases using only one piece of data.

The decrease in convergence when attempting to infer more parameters lends to to the question of whether adding surface velocity would increase the convergence. To this end, we explore inferring the rheological parameters using both surface normal stress and surface velocity. We first infer individual parameters for both pieces of data to make sure that the correct value is attained. In Cases 9-11, we find that we correctly infer the strain rate exponent/weakfactor/activation energy within 3 iterations, suggesting that there may not be conflicts in using both data types. In Case 12, as we infer the strain rate exponent and weak factor, we also find that we infer the true value within 3 iterations. As a direct comparison to Case 8, we infer the strain rate exponent, weakfactor and activation energy in Case 13 and find that we not only are able to infer the correct values, but we do so in less iterations (4 iterations) as shown in Fig.3.2d,e,f.

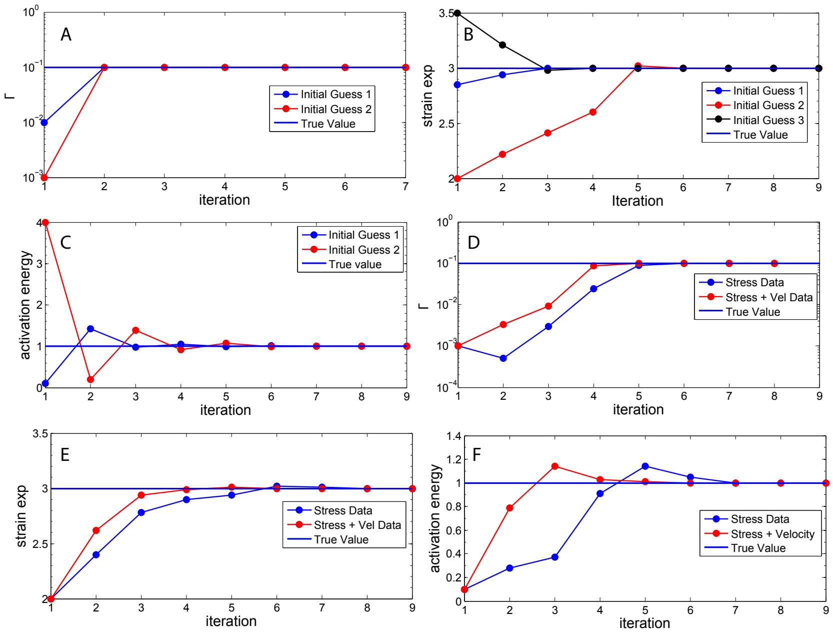

Figure 3.2: (a)Cases 1 and 2 (inference for weakfactor with only normal stress data) (b)Cases 3-5 (inference for strain rate exponent with only normal stress data) (c) Cases 6 and 7 (inference for activation energy with only normal stress data) (d)Weakfactor comparison between cases 8 and 13 (e)Strain rate exponent comparison between cases 8 and 13 (f)Activation energy comparison between cases 8 and 13

3.6 Discussion

We were able to infer various rheological parameters for the sinking mass anomaly using this new adjoint formulation. We show that in Cases 1-2, we can correctly infer the weak layer prefactor, (independent of the initial guess), within 3 iterations. We similarly find that we can infer the strain rate exponent (Cases 3-5) and activation energy (Cases 6-7) within 4-5 iterations, independent of the initial guess. Furthermore, we demonstrate that using both surface velocity and surface normal stress can potentially accelerate the convergence of inversions as shown between Case 8 and 13.

While we were able to implement and prove the validity of using the surface normal stress in the adjoint formulation, there still are issues in applying this method to subduction zones. One of these issues lies in the large variations in viscosity and the boundary conditions on the surface (Crameri et al., 2017). The problem is that there are large dynamic topography near the trench that exceed 10km in forward models, which is certainly not found in the observations. Therefore, the adjoint formulation with surface normal stress will not work when no forward model is able to produce reasonable short wavelength topographic signals.

The problematic issue of large topographic magnitudes can be traced to the large variations in viscosity of the forward model between plate and the weakzone ($\mathcal{O}(10^6)$). We find that when the viscosity variations are reduced, the magnitude of the topography was also reduced. However, this also caused an increase in the fore-bulge. Additionally, when using a sticky-air surface (weak viscosity layer at the surface), we find that the we could reduce the amplitude of the topography signal at the trench. The sticky-air method brings an added complication of measuring the topography due to the interface between the sticky-air layer and the oceanic plates. It is certainly clear from those investigations that to remedy the large trench depths requires a different formulation of the effective viscosity and/or surface boundary conditions. However, after the issue of large topographic signals is resolved, the use of the adjoint with surface normal stress can be readily used.

3.7 Supplementary Material: Gradient and Hessian Tests

3.8 Cases 1 and 2

Table 3.2: Inversion statistics for $\gamma_{\text{guess}} = 10^{-2}$

$Iteration$	$\mathcal{H}$	$\lvert\mathcal{G}\rvert$
1	$2.02 \cdot 10^{9}$	$3.675 \cdot 10^{10}$
2	$3.47 \cdot 10^{10}$	$2.948 \cdot 10^{9}$
3	$4.95 \cdot 10^{10}$	$1.899 \cdot 10^{8}$
4	$5.46 \cdot 10^{10}$	$9.91 \cdot 10^{6}$
5	$5.72 \cdot 10^{10}$	$5.06 \cdot 10^{5}$

Table 3.3: Inversion statistics for $\gamma_{\text{guess}} = 10^{-3}$

$Iteration$	$\mathcal{H}$	$\lvert\mathcal{G}\rvert$
1	$1.248 \cdot 10^{8}$	$8.452 \cdot 10^{10}$
2	$5.53 \cdot 10^{10}$	$3.7718 \cdot 10^{9}$
3	$5.775 \cdot 10^{10}$	$1.531 \cdot 10^{8}$
4	$5.917 \cdot 10^{10}$	$9.91 \cdot 10^{6}$
5	$6.002 \cdot 10^{10}$	$7.97 \cdot 10^{5}$
6	$6.05 \cdot 10^{10}$	$6.374 \cdot 10^{5}$
7	$6.08 \cdot 10^{10}$	$5.06 \cdot 10^{4}$

3.9 Cases 3-5

Table 3.4: Inversion statistics for $n_{\text{guess}} = 2.85$

$Iteration$	$\mathcal{H}$	$\lvert\mathcal{G}\rvert$
1	$3.977 \cdot 10^{12}$	$1.717 \cdot 10^{11}$
2	$3.0604 \cdot 10^{12}$	$8.663 \cdot 10^{10}$
3	$2.104 \cdot 10^{12}$	$3.356 \cdot 10^{9}$
4	$2.057 \cdot 10^{12}$	$4.461 \cdot 10^{8}$
5	$2.0638 \cdot 10^{12}$	$6.985 \cdot 10^{7}$
6	$2.06281 \cdot 10^{12}$	$1.044 \cdot 10^{7}$
7	$2.06296 \cdot 10^{12}$	$1.567 \cdot 10^{6}$
8	$2.06294 \cdot 10^{12}$	$2.342 \cdot 10^{5}$
9	N/A	$3.5047 \cdot 10^{4}$

Table 3.5: Inversion statistics for $n_{\text{guess}} = 2.0$

Iteration	$\mathcal{H}$	$\lvert\mathcal{G}\rvert$
1	$2.7665 \cdot 10^{13}$	$3.488 \cdot 10^{12}$
2	$3.944 \cdot 10^{13}$	$2.912 \cdot 10^{12}$
3	$3.092 \cdot 10^{13}$	$1.257 \cdot 10^{12}$
4	$8.617 \cdot 10^{12}$	$2.675 \cdot 10^{11}$
5	$1.797 \cdot 10^{12}$	$1.1778 \cdot 10^{10}$
6	$2.146 \cdot 10^{12}$	$3.647 \cdot 10^{9}$
7	$2.0496 \cdot 10^{12}$	$5.832 \cdot 10^{8}$
8	$2.0655 \cdot 10^{12}$	$1.137 \cdot 10^{8}$
9	$2.06245 \cdot 10^{12}$	$2.159 \cdot 10^{7}$

Table 3.6: Inversion statistics for $n_{\text{guess}} = 3.5$

Iteration	$\mathcal{H}$	$\lvert\mathcal{G}\rvert$
1	$3.658 \cdot 10^{11}$	$3.1396 \cdot 10^{11}$
2	$1.2446 \cdot 10^{12}$	$1.76443 \cdot 10^{11}$
3	$2.64779 \cdot 10^{12}$	$1.351 \cdot 10^{11}$
4	$2.03321 \cdot 10^{12}$	$6.92 \cdot 10^{9}$
5	$2.06992 \cdot 10^{12}$	$1.386 \cdot 10^{9}$
6	$2.06271 \cdot 10^{12}$	$2.525 \cdot 10^{8}$
7	$2.06406 \cdot 10^{12}$	$6.143 \cdot 10^{7}$
8	$2.06372 \cdot 10^{12}$	$2.221 \cdot 10^{7}$
9	$2.06381 \cdot 10^{12}$	$7.9271 \cdot 10^{6}$

Table 3.7: Gradient check for activation energy with $E_a^0 = 4.0$

iteration	$\mathcal{G}_{Adjoint}$	$\mathcal{G}_{FD}$
1	$3.812 \cdot 10^{8}$	$3.892 \cdot 10^{8}$
2	$-4.622 \cdot 10^{7}$	$-4.632 \cdot 10^{7}$
3	$2.114 \cdot 10^{6}$	$2.101 \cdot 10^{6}$
4	$-5.44 \cdot 10^{5}$	$-5.342 \cdot 10^{5}$
5	$6.9301 \cdot 10^{4}$	$6.922 \cdot 10^{4}$
6	$-5.10 \cdot 10^{4}$	$-5.102 \cdot 10^{4}$
7	$2.110 \cdot 10^{4}$	$2.115 \cdot 10^{4}$
8	$-1.01 \cdot 10^{4}$	$-1.02 \cdot 10^{4}$

Chapter 4

INFERENCE OF PLATE BOUNDARY PROPERTIES WITH AN ADJOINT OPTIMIZATION WITH LARGE SCALE TWO-DIMENSIONAL MODELS

ABSTRACT

Plate motions are a primary surface constraint on forward models of plate and mantle dynamics and rheology, plate boundary stresses, and the occurrence of great earthquakes. Estimates of effective viscosity regionally provide additional constraints on mantle dynamics. Here we incorporate plate motion and effective viscosity data into an optimization and derive adjoint, gradients for inferred parameters, and posterior distributions for rheological paramters, stresses within plate boundaries, and the effective viscosity of subducted slabs. We apply these methods to 2-D cross-sections of subduction zones, with temperature distributions and fault zone geometries developed from seismic and other data. Analyzing the conditional and marginal distributions, we find that the Tonga and the Marianas subduction zones have the lowest values of mechanical coupling while Chile and Sumatra the highest, among those studied. The subduction zones with the lowest coupling have back-arc extension. Globally, we find that the non-linear stress-strain exponent, n, is 3.08 ± 0.25 (in the upper mantle and lithosphere) with a pressure-independent yield stress of 130-146 MPa. The stress in shear zones is tens of MPa and the shear and the normal stresses are elevated in seismically coupled compared to uncoupled subduction zones. Relative differences in inferred mechanical couplings are similar to observed seismic coupling. We find that within the hinge zone for subduction zones is about $8 \cdot 10^{21} Pa \cdot s$. This partition of average effective viscosity suggests that there is a link between plate coupling and the average dynamic weakening for seismically coupled subduction zones.

4.1 Introduction

While slab pull may be the dominant force driving plate motions and associated mantle flow, there remains uncertainty on the relative coupling of stresses across plate boundaries at subduction zones. This coupling can either be attributed to broad-scale tectonic forces or the varying properties between plates at each subduction zone. While it is not clear whether broad-scale forces or the varying properties have the stronger contribution to the variations in seismic coupling, a valid model should appropriately represent the broad-scale forces. Seismic coupling is defined as the ratio between the observed seismic moment release to the rate of plate tectonic velocities and generally varies between 0 and 1 (Davies and Brune, 1971). Seismic coupling is sensitive to the short window of recorded earthquakes such that if many large magnitude earthquakes occur within that short window at a greater rate than the long-term average, seismic coupling could be close to or even exceed unity, whereas if the earthquakes occur at an unusually low rate, inferred seismic coupling will be small. While seismic coupling is a reasonable way to build a relationship to forecast which subduction zones have a propensity for future large events, additional data, for example, the curvature of subduction zones (Bletery et al., 2016) or along-strike gravity anomalies (Song and Simons, 2003), can better condition such forecasts.

Regardless of the controls on seismic coupling, geodynamic models should be able to explain variations between the two end-members from the least coupled Marianas to the coupled Chilean subduction zone. The Chilean subduction zone is among the most seismically active with many earthquakes above 8, including the 1960 Valdivia earthquake with moment magnitude 9.5 (Kanamori and Cipar, 1974), the largest ever recorded. On the other hand the Marianas subduction zone is among the least seismically coupled with no historic earthquakes greater than magnitude 7.7 (McCaffrey, 2008). Chile, overall is in a state of compression on the South American margin, while, the Marianas subduction zone is characterized by active back arc opening indicative of regional tension.

A simple force balance of subduction that parameterizes the broad-scale forces suggests a link between tectonic forces and the degree of seismic coupling (Scholz and Campos, 1995; Scholz and Campos, 2012). These models estimate the force distribution that arises from slab pull and a putative anchoring force, for each subduction zone. Such models do not include realistic subduction geometry, variations in rheology, and how such variations would influence the distribution of normal forces. While the analysis found a relationship between broad-scale forces and coupling, their approach may not capture the essence of the system as the actual geometry of slabs is complex with substantial variations induced by global flow (Scholz and Campos, 2012). Although simple, these force balance models haven't found general acceptance.

To accurately estimate the forces at plate boundaries, not only is the correct physics of mantle flow and lithospheric deformation needed, but an optimization scheme must be constrained by observed plate motions (Burstedde, Stadler, et al., 2013; Stadler et al., 2010), the most robust constraint on mantle dynamics. We overcome these limitations by employing an approach similar to that introduced earlier (Ratnaswamy et al., 2015), with plate motion data used for areas away from deforming plate boundaries, essentially allowing for self-consistent deformation within plate boundaries. Furthermore, the shape of fault zones play a key role in governing plate motions (Zhong and Gurnis, 1995), and these can be mapped at shallow depths with seismic observations and are needed as constraints. Augmenting surface velocities, we now incorporate constraints on the average viscosity within selected regions. Estimates of the average effective viscosity arise from post-glacial rebound and post-seismic relaxation. Using constraints on viscosity may allow for a better estimation of the strain rate exponent, upper mantle prefactor and bulk effective mantle properties compared to an optimization that solely uses plate motion data. The viscosity reduction for a shear zone representing the megathrust between plates has been inferred from the adjoint-based optimization, but not the state of stress. We show that such stresses can be estimated from an additional adjoint solve. We determine the trade-offs between the calculated stresses and inferred rheological parameters.

In this chapter, we will explore the incorporation of average effective viscosities and estimation of stress uncertainty in fault zones. While inferring plate boundary strength factors (Ratnaswamy et al., 2015) can lead to a better understanding of which plate boundaries are more mechanically coupled, such variables are intrinsic (and non-dimensional) and so here we estimate the extrinsic quantity (the magnitude of stresses) and their uncertainties. We will derive expressions for the gradients of inferred parameters using average effective viscosity and expressions for the covariance matrices of the average normal and shear stresses. We then apply these methods to 2D cross-sectional slices with observed plate motions and viscosity constraints and thermal structures and fault zone geometries constrained by a variety of other (but primarily seismic) data.

Models with a simple parameterization of plate boundary strength, in which no mechanical distinction is made between the bending plate and the zone of inter-plate coupling are to be avoided. Plate bending and interplate coupling are observationally resolved and distinct processes and if we hope to understand the plate tectonic controls on interplate seismic coupling and how slab strength may influence plate motions, while moving forward with a new framework to link geodynamics to the occurrence of great earthquakes, then the more complete formulation we have adopted is essential.

4.2 Forward Model

The underlying physics of mantle flow is governed by the creeping of mantle rocks over geological time scales. Over time scales greater than about 1 year, deformation of the mantle behaves as a viscous fluid governed by the Stokes equations

$$\begin{aligned} \nabla \cdot \boldsymbol{u} &= 0 \qquad \text{on } \Omega, \\ \nabla \cdot \boldsymbol{\sigma} &= -\mathrm{Ra} T \mathbf{e}_r \qquad \text{on } \Omega, \end{aligned} \tag{4.1}$$

with free slip boundary conditions

$$\begin{aligned} \boldsymbol{u} \cdot \mathbf{n} &= 0 \quad \text{on } \partial\Omega, \\ \mathbf{T}(\boldsymbol{\sigma}\mathbf{n}) &= 0 \qquad\qquad\qquad\qquad \text{on } \partial\Omega \end{aligned}$$

with viscous stress tensor being $\boldsymbol{\sigma} := 2\eta(T, n, \boldsymbol{\sigma}_y) - p\mathbf{I}$ where p is the forward pressure, and $\mathbf{T}$ is the tangential operator ($\mathbf{T} = \mathbf{I} - \mathbf{n} \otimes \mathbf{n}$). Furthermore, the momentum equation in (4.1) is driven by thermal buoyancy where T is the temperature field and Ra is the thermal Rayleigh number. Solving the Stokes equations, we obtain the solution of the forward velocities ($\boldsymbol{u}$) and pressures (p). An important part of the stress tensor $\boldsymbol{\sigma}$ is the rheological relationship. In our forward model we use a nonlinear rheology where we take into account the shear-thinning nature of the upper mantle through the use of a power law rheology with a strain rate exponent and the diffusion creep in the lower mantle with a linear rheology, while using a global yield stress to allow for dynamic weakening (which primarily occurs within the hinge zones, that is where slabs bend). Our viscosity formulation is

$$\eta(\dot{\varepsilon}_{\mathrm{II}}, \sigma_y) = \eta_{\mathrm{min}} + \min(\Gamma_i \min(\eta_{\mathrm{max}}, a(T)(\dot{\varepsilon}_{\mathrm{II}} - d)^{\frac{1}{2n}} \dot{\varepsilon}_{\mathrm{II}}^{-\frac{1}{2}}), \frac{1}{2}\sigma_y \dot{\varepsilon}_{\mathrm{II}}^{-\frac{1}{2}}) \tag{4.2}$$

where η_{min} is the minimum effective viscosity, Γ_i is the weak zone factor for plate margin i, σ_y is the yield stress, $a(T)$ is the temperature dependent component of viscosity, n is the strain rate exponent and d is a parameter included to regularize the solution. In (4.2) we compute the power-law and temperature dependent part of the rheology first and take the minimum between that viscosity and the maximum viscosity (η_{max}), while applying the weakfactor Γ to that viscosity. Dynamic weakening is taken into account by comparing the minimum between the viscosity from yielding and the viscosity obtained from the minimum between the maximum effective viscosity (η_{max}) and the shear-thinning, temperature dependent viscosity. We then regularize the viscosity by adding a minimum effective viscosity η_{min}.

4.3 Bayesian Problem Formulation

We cast the inverse problem in a Bayesian sense, in which we find the posterior distribution ($\boldsymbol{\pi}_{post}$) for the inferred rheological parameters (for example the strain rate exponent and weakfactors). We cast the inverse using Bayes theorem (4.3) Tarantola (2002),

$$\boldsymbol{\pi}_{post} \approx \boldsymbol{\pi}_{like}\boldsymbol{\pi}_{prior} \tag{4.3}$$

where the $\boldsymbol{\pi}_{like}$ is the likelihood distribution and $\boldsymbol{\pi}_{prior}$ is the prior distribution, as no single set of parameters represents a unique solution, so we seek the Bayesian solution to the problem. The likelihood distribution is given as,

$$\boldsymbol{\pi}_{like} = \exp\left\{-\frac{1}{2}(\boldsymbol{u}-\boldsymbol{u}_{\text{obs}})^{\intercal} C_{data}^{-1}(\boldsymbol{u}-\boldsymbol{u}_{\text{obs}})\right\} \tag{4.4}$$

where $\boldsymbol{u}_{data}$ is the observed velocity data, $\boldsymbol{u}$ is the results from a forward model and C_{data} is the covariance matrix for the observed data. The likelihood distribution gives an estimate of how well the model parameters explain the data. However, if there is knowledge of the distribution of the inferred parameters, then that knowledge can be incorporated into the prior distribution ($\boldsymbol{\pi}_{prior}$).

We build upon our earlier work (Ratnaswamy et al., 2015) through the addition of several enhancements. We quantify the uncertainty of plate boundary stresses since the uncertainty and correlations of stress with rheological parameters gives a more meaningful physical interpretation of the interactions occuring in the models. The stresses in the fault zones are not initially inferred with the adjoint formulation, and do not have a covariance distribution readily available. A Markov Chain Monte Carlo (MCMC) approach would likely recover the covariance but would require many samples (forward solutions) and make the optimization computationally intractable. Alternatively, we will derive Gaussian approximations for the covariance distributions for the stresses within fault zones. Furthermore, we incorporate the effective viscosity for selected regions of the mantle, so that the optimization problem provides a better estimate for the rheological parameters and in turn refined estimates on the stresses within plate boundaries. Incorporating the average effective viscosity requires the derivation of a new adjoint system that will be developed here. Finally, the refined method is applied to geophysical data in a series of cross-sectional models of different plates and subduction zones.

Covariance of Extrinsic Quantities

In the earlier models, we were able to estimate the parameters in the rheological relationship for synthetic models (Ratnaswamy et al., 2015); however, there were no bounds placed on the uncertainty of derived quantities, such as the shear stresses, that are dependent on the rheological parameters.

Here, we must build an approximation of such derived quantities. This quantity is embedded in the weak factors, but the weak factors are a parameterization, that requires a mapping to stress, including the normal and tangential stresses and a square-root of the second invariant of the stress tensor (σ_{avg}), i.e.

$$\sigma_{avg} = \int_{\Omega_w} (\boldsymbol{\sigma} : \boldsymbol{\sigma})^{\frac{1}{2}} d\omega \tag{4.5}$$

where Ω_w represents the volume of a partcular weak zone. Helpful quantities for addressing the origin of seismic coupling through the geographic variability of great earthquakes, include the average shear (σ_{avg}^T) and normal tractions (σ_{avg}^N) in the weak zones,

$$\sigma_{avg}^N = \int \mathbf{N}\boldsymbol{\sigma} \cdot \mathbf{n} d\Omega_w \tag{4.6}$$

$$\boldsymbol{\sigma_{avg}^T = \int \mathbf{T}\sigma \cdot \mathbf{n} d\Omega_w.} \tag{4.7}$$

The normal and shear components of the stress are important as they effectively give the resisting stresses along the plate boundaries. The larger the resisting stress, the more mechanically coupled a plate boundary, and vice versa. Here, T and **N** are the tangential and normal projection along the center line of the plate boundaries,

$$\begin{aligned} \mathrm{T} &= \mathbf{I} - \mathrm{n}_w \otimes \mathrm{n}_w \\ \mathbf{N} &= \mathrm{n}_w \otimes \mathrm{n}_w \end{aligned} \tag{4.8}$$

where n_w is the normal vector along the fault zone. We estimate Gaussian distributions of the weak factors and stresses in each plate boundary,

$$\boldsymbol{\pi}_{\Gamma_i} = \mathcal{N}(\Gamma_i^{map}, \sigma_{\Gamma_i}) \tag{4.9}$$

$$\boldsymbol{\pi}_{\sigma_i^n} = \mathcal{N}(\sigma_i^{map}, \sigma_{\sigma_i}) \tag{4.10}$$

The stresses provide a more physically intuitive description of plate coupling compared to the weak-zone pre-factors (Γ_i).

$$\mathcal{N}(\mu_{map}, s) = \int \frac{1}{s\sqrt{2\pi}} \exp(-\frac{(x-\mu_{map})^2}{2s^2}) dx \tag{4.11}$$

Unlike the rheological parameters, we do not infer the shear and normal stress in our optimization framework. Instead, a Gaussian approximation to the normal stress in Eq. (4.11) is constructed. A natural question would be how well the posterior distributions for the stresses are approximated by a Gaussian distribution. Locally, near the maximum a posteriori point (**MAP**),for this nonlinear problem, we have found that the conditional distribution and to an extent the marginal distributions are well approximated by a Gaussian approximation to the posterior distribution (Ratnaswamy et al., 2015). We define a measure of the stress from the underlying properties such as the strain rate exponent, yield stress and so forth, e.g. $\boldsymbol{m}$, the model parameters, as,

$$\boldsymbol{\sigma} = f(\boldsymbol{m}) \tag{4.12}$$

expanding $\boldsymbol{\sigma}$,

$$\boldsymbol{\sigma}(\boldsymbol{m}) = \boldsymbol{\sigma}(\boldsymbol{m}_{map}) + \frac{\partial \boldsymbol{\sigma}}{\partial \boldsymbol{m}}|_{\boldsymbol{m}_{map}}(\boldsymbol{m} - \boldsymbol{m}_{MAP}) + h.o.t \tag{4.13}$$

The mean of $\boldsymbol{\sigma}$is $\boldsymbol{\sigma}(\boldsymbol{m}_{map})$, while the covariance is defined as,

$$C = \mathcal{E}[(\boldsymbol{\sigma} - \mu_{\boldsymbol{\sigma}})^{\intercal}(\boldsymbol{\sigma} - \mu_{\boldsymbol{\sigma}})] = \mathcal{E}[(\boldsymbol{\sigma} - \boldsymbol{\sigma}(\boldsymbol{m}_{map}))^{\intercal}(\boldsymbol{\sigma} - \boldsymbol{\sigma}(\boldsymbol{m}_{map}))] \tag{4.14}$$

where $\mathcal{E}$ denotes the expectation (i.e. the mean). For example, the expected value of a continuous random variable x is defined,

$$\mathcal{E}(x) := \int x p(x) dx \tag{4.15}$$

where $p(x)$ is the probability distribution of x. Using a Taylor series expansion of the stress, while only retaining the 1^{st} order terms, we obtain

$$\boldsymbol{\sigma}(\boldsymbol{m}) - \boldsymbol{\sigma}(\boldsymbol{m}_{map}) \approx \frac{\partial \boldsymbol{\sigma}}{\partial \boldsymbol{m}}(\boldsymbol{m} - \boldsymbol{m}_{MAP}) \tag{4.16}$$

Therefore

$$C = \mathcal{E}\big[\big(\frac{\partial \boldsymbol{\sigma}}{\partial \boldsymbol{m}}|_{\boldsymbol{m}_{map}}(\boldsymbol{m} - \boldsymbol{m}_{MAP})\big)^{\intercal}\big(\frac{\partial \boldsymbol{\sigma}}{\partial \boldsymbol{m}}|_{\boldsymbol{m}_{map}}(\boldsymbol{m} - \boldsymbol{m}_{MAP})\big)\big] \tag{4.17}$$

which leads to

$$C = \Big(\frac{\partial \boldsymbol{\sigma}}{\partial \boldsymbol{m}}\Big|^{\intercal}_{\boldsymbol{m}_{map}} \mathcal{E}[(\boldsymbol{m} - \boldsymbol{m}_{MAP})^{\intercal}(\boldsymbol{m} - \boldsymbol{m}_{MAP})]\Big(\frac{\partial \boldsymbol{\sigma}}{\partial \boldsymbol{m}}\Big|_{\boldsymbol{m}_{map}}\Big) \tag{4.18}$$

where

$$\mathcal{E}[(\boldsymbol{m} - \boldsymbol{m}_{MAP})^{\intercal}(\boldsymbol{m} - \boldsymbol{m}_{MAP})] = \mathcal{H}^{-1}(\boldsymbol{m}) = C(\boldsymbol{m}) \tag{4.19}$$

leading to

$$C(\boldsymbol{\sigma}) = \frac{\partial \boldsymbol{\sigma}}{\partial \boldsymbol{m}}\Big|^{\intercal}_{\boldsymbol{m}_{map}} \mathcal{H}^{-1}(\boldsymbol{m}) \frac{\partial \boldsymbol{\sigma}}{\partial \boldsymbol{m}}\Big|_{\boldsymbol{m}_{map}} \tag{4.20}$$

or

$$C(\boldsymbol{\sigma}) = \frac{\partial \boldsymbol{\sigma}}{\partial \boldsymbol{m}}\Big|^{\intercal}_{\boldsymbol{m}_{map}} C(\boldsymbol{m}) \frac{\partial \boldsymbol{\sigma}}{\partial \boldsymbol{m}}\Big|_{\boldsymbol{m}_{map}} \tag{4.21}$$

with $C(\boldsymbol{m})$ is the covariance matrix obtained from solving for the MAP point in the original optimization problem and $\mathcal{H}$ is the Hessian. Therefore, the normal distribution of the stresses is

$$\boldsymbol{\pi}_{\boldsymbol{\sigma}} = \mathcal{N}\Big(\boldsymbol{\sigma}(\boldsymbol{m}_{map}), \frac{\partial \boldsymbol{\sigma}}{\partial \boldsymbol{m}}\Big|^{\intercal}_{\boldsymbol{m}_{map}} C(\boldsymbol{m}) \frac{\partial \boldsymbol{\sigma}}{\partial \boldsymbol{m}}\Big|_{\boldsymbol{m}_{map}}\Big) \tag{4.22}$$

To form the Gaussian approximation of the stress within each weakzone, we compute the gradient of the stress with respect to the inferred parameters. This amounts to making an additional adjoint solve, and a gradient computation. Taking variations of Eq. (4.7) with respect to the velocity

$$\boldsymbol{\sigma^{\tau}_{avg}} = \mathbf{T}\frac{\partial \boldsymbol{\sigma}}{\partial \mathbf{u}} \cdot \mathbf{n} \tag{4.23}$$

with

$$\frac{\partial \sigma}{\partial \mathbf{u}} = \frac{\partial \eta}{\partial \mathbf{u}}\dot{\epsilon}(\mathbf{u}) + \eta\dot{\epsilon}(\delta\mathbf{u}) \tag{4.24}$$

This is just an application of the linearized Newton operator to the velocity of the forward model at the **MAP** point. For the second invariant of the stress tensor, additional terms compared to the average stress are required because of the dependence of the stress on the effective viscosity,

$$\begin{aligned} \boldsymbol{\sigma}_{II} &= \frac{1}{2}\mathbf{Tra}(\boldsymbol{\sigma} : \boldsymbol{\sigma}) \\ &= \frac{1}{2}[\eta\dot{\boldsymbol{\varepsilon}}(\boldsymbol{u}) : \eta\dot{\boldsymbol{\varepsilon}}(\boldsymbol{u})] \\ &= \frac{1}{2}[\dot{\boldsymbol{\varepsilon}}(\boldsymbol{u}) : \eta^{2}\dot{\boldsymbol{\varepsilon}}(\boldsymbol{u})] \end{aligned} \tag{4.25}$$

then,

$$\frac{\partial \boldsymbol{\sigma}_{II}}{\partial \boldsymbol{u}} = \dot{\boldsymbol{\varepsilon}}(\delta \boldsymbol{u}) : \eta^2 \dot{\boldsymbol{\varepsilon}}(\boldsymbol{u}) + \dot{\boldsymbol{\varepsilon}}(\boldsymbol{u}) : \dot{\boldsymbol{\varepsilon}}(\boldsymbol{u}) \eta \frac{\partial \eta}{\partial \dot{\varepsilon}_{\mathrm{II}}} (\dot{\boldsymbol{\varepsilon}}(\boldsymbol{u}) : \dot{\boldsymbol{\varepsilon}}(\delta \boldsymbol{u})) \tag{4.26}$$

After solving for the adjoint in (4.26), we then compute the gradient for (4.7),

$$\boldsymbol{\mathcal{G}} := \mathbf{T} \frac{\boldsymbol{\partial \sigma}}{\boldsymbol{\partial m}} \cdot \mathbf{n} \tag{4.27}$$

where,

$$\frac{\partial \boldsymbol{\sigma}}{\partial \boldsymbol{m}} = \eta_{,i} \dot{\boldsymbol{\varepsilon}}(\boldsymbol{u}) \tag{4.28}$$

For the second invariant of the stress tensor, we compute the gradient

$$\mathcal{G} := \dot{\boldsymbol{\varepsilon}}(\boldsymbol{u}) : 2\eta \cdot \eta_{,\boldsymbol{m}} \dot{\boldsymbol{\varepsilon}}(\boldsymbol{u}) \tag{4.29}$$

where the derivatives of the effective viscosity with respect to the rheological parameters are

$$\begin{aligned} &\eta_{,i}(\dot{\varepsilon}_{\mathrm{II}}, \Gamma, n, \sigma_y) \\ &\quad = \begin{cases} 0 & \text{in } \Omega_y, \\ \Gamma_i \chi_i \min(\eta_{\max}, a(T)(\dot{\varepsilon}_{\mathrm{II}} - d)^{\frac{1}{2n}} \dot{\varepsilon}_{\mathrm{II}}^{-\frac{1}{2}}) & \text{in } \Omega \setminus \Omega_y. \end{cases} \end{aligned}$$

where $\Gamma_i = \exp(m_i)$.

$$\eta_{,i}(\dot{\varepsilon}_{\mathrm{II}}, \Gamma, n, \sigma_y) = \begin{cases} \frac{1}{2} \sigma_y \dot{\varepsilon}_{\mathrm{II}}^{-\frac{1}{2}} & \text{in } \Omega_y, \\ 0 & \text{in } \Omega \setminus \Omega_y. \end{cases}$$

Finally, if $m_i = \log(n)$, we obtain

$$\eta_{,i}(\dot{\varepsilon}_{\mathrm{II}}, \Gamma, n, \sigma_y) = \begin{cases} \Gamma a(T) \omega (\dot{\varepsilon}_{\mathrm{II}} - d)^{\frac{1}{2n}} \dot{\varepsilon}_{\mathrm{II}}^{-\frac{1}{2}} & \text{in } \Omega_w, \\ 0 & \text{in } \Omega \setminus \Omega_w, \end{cases}$$

where $\omega = \log((\dot{\varepsilon}_{\mathrm{II}} - d)^{-\frac{1}{2n}})$ and $\Omega_w \subset \Omega$ are the points where $\eta(\dot{\varepsilon}_{\mathrm{II}}, \Gamma, n, \sigma_y) = \eta_{\min} + a(T)(\dot{\varepsilon}_{\mathrm{II}} - d)^{1/(2n)} \dot{\varepsilon}_{\mathrm{II}}^{-1/2}$, where Ω_w is the upper mantle where there is dislocation creep, and thus the rheology depends depends on the strain rate exponent n. It should be noted that we use log parameterization of each of the inferred parameters so as to enforce the non-negativity of their values (Tarantola, 2002).

Computing the covariance matrix of the stress effectively adds regularization to the normal and shear stress covariance matrix because the stress values depend on the values of the inferred parameters at the **MAP** point. After computing the gradient of the stress, we can now form the covariance of the stress by first forming the matrix,

$$\frac{\partial \boldsymbol{\sigma}}{\partial \boldsymbol{m}} = \begin{bmatrix} \mathcal{G}^{w_1}_{,\Gamma_{w_1}} & \mathcal{G}^{w_2}_{,\Gamma_1} & \cdots & \mathcal{G}^{w_n}_{,\Gamma_1} \\ \mathcal{G}^{w_1}_{,\Gamma_2} & \mathcal{G}^{w_2}_{,\Gamma_2} & \cdots & \mathcal{G}^{w_n}_{,\Gamma_2} \\ \vdots & \vdots & \vdots & \vdots \\ \mathcal{G}^{w_1}_{,\Gamma_3} & \mathcal{G}^{w_2}_{,\Gamma_3} & \cdots & \mathcal{G}^{w_n}_{,\Gamma_3} \\ \mathcal{G}^{w_1}_{,n} & \mathcal{G}^{w_2}_{,n} & \cdots & \mathcal{G}^{w_n}_{,n} \\ \mathcal{G}^{w_1}_{,\sigma_y} & \mathcal{G}^{w_2}_{,\sigma_y} & \cdots & \mathcal{G}^{w_n}_{,\sigma_y} \end{bmatrix} \tag{4.30}$$

The values in (4.30) with superscript w_i represent the plate boundaries (plate boundary 1, plate boundary 2 and so forth).

Cost Functional with average effective viscosity data

Previously, we (Ratnaswamy et al., 2015) only used surface velocity data within areas of presumed rigid plate motion. However, there are some areas in the mantle where there are independent estimates of the average effective viscosity including regions sampled by post-glacial rebound and post-seismic relaxation such as that associated with the 2012 Indian Ocean earthquake (Hu et al., 2016). These constraints from the 2012 Indian Ocean earthquake are potentially important as the loading was from a large intraplate oceanic earthquake within the lithosphere but constrained by onshore GPS displacement data. These provide bounds on the viscosity immediately below an oceanic plate from a transient loading event. We can add these post-glacial and post-seismic constraints into our model in a 'generic' sense, that is areas under normal continental cratons and those below oceanic lithosphere just before the oceanic lithsphere starts to subduct. Estimates on the viscosity of the upper mantle below northern Europe from post glacial rebound are about 10^{21}Pa·s (Cathles, 2015). The constraints on the viscosity below North America are potentially more sensitive to both the upper mantle and the top of the lower mantle (Mitrovica and Peltier, 1995; Simons and Hager, 1997). For global models, these constraints would be added to the explicit region constrained by the transient observation.

These estimates of the average effective viscosity are only available in regions where the mantle has undergone some response from deformation and are primarily available in the upper mantle. There are a few ways to incorporate the effective viscosity, where $\overline{\eta}_j$ is the observational constraint for region j and η is the computed effective viscosity.

$$\mathcal{J}_{pointwise} = \frac{1}{2}(\overline{\eta}_j - \eta)^2 \tag{4.31}$$

Using this pointwise formulation would effectively push the region with the viscosity constraint toward a more homogeneous state, i.e. each point within the observation region is forced to have the observed effective viscosity. A more appropriate formulation is

$$\mathcal{J}_{average} = \frac{1}{2}(\overline{\eta}_j - \exp(\int_{\Omega_j} \ln \eta \, d\Omega_j))^2. \tag{4.32}$$

where $\overline{\eta}_i$ is the constrained viscosity within domain Ω_i.

Making use of this constraint, we then formulate the misfit as,

$$\mathcal{J}(\boldsymbol{u}, \boldsymbol{m}, p) := \frac{1}{2} \int_{\partial\Omega_1} (\boldsymbol{O}\boldsymbol{u} - \boldsymbol{u}_{\mathrm{obs}})^\intercal C_{vel}^{-1} (\boldsymbol{O}\boldsymbol{u} - \boldsymbol{u}_{\mathrm{obs}}) d\partial\Omega_1 + \frac{1}{2}(\overline{\eta}_j - \exp(\int_{\Omega_j} \ln \eta \, d\Omega_j))^2. \tag{4.33}$$

Taking derivatives of the cost function in (4.33) with respect to the forward variables $(\boldsymbol{u}, p)$ and employing the divergence theorem as in (Ratnaswamy et al., 2015), we arrive at the adjoint system

$$\begin{aligned} \nabla \cdot \boldsymbol{v} &= 0 \qquad \text{on } \Omega, \\ \nabla \cdot \hat{\boldsymbol{\sigma}}_{\boldsymbol{u}} &= -\nabla \cdot \Psi \qquad \text{on } \Omega, \end{aligned} \tag{4.34}$$

where $\Psi = (1 - \frac{1-n}{n} \dot{\boldsymbol{\varepsilon}}(\boldsymbol{u}) : \dot{\boldsymbol{\varepsilon}}(\boldsymbol{u}))\mathbb{I} + \frac{1-n}{n} \frac{\dot{\boldsymbol{\varepsilon}}(\boldsymbol{u}) \otimes \dot{\boldsymbol{\varepsilon}}(\boldsymbol{u})}{\dot{\boldsymbol{\varepsilon}}(\boldsymbol{u}) : \dot{\boldsymbol{\varepsilon}}(\boldsymbol{u})}$, and boundary conditions

$$\begin{aligned} \boldsymbol{v} \cdot \mathbf{n} &= 0 \quad \text{on } \partial\Omega, \\ \mathrm{T}(\hat{\boldsymbol{\sigma}}_{\boldsymbol{u}} \mathbf{n}) &= \begin{cases} 0 & \text{on } \partial\Omega \setminus \partial\Omega_t, \\ -\boldsymbol{O}^\intercal C_{\mathrm{noise}}^{-1} (\boldsymbol{O}\boldsymbol{u} - \boldsymbol{u}_{\mathrm{obs}}) & \text{on } \partial\Omega_t, \end{cases} \end{aligned}$$

where T is the tangential operator in which our primary constraint is the observed plate velocities, $\boldsymbol{u}_{\mathrm{obs}}$, optimized against the forward prediction of the velocity, $\boldsymbol{u}$. In addition, $\hat{\boldsymbol{\sigma}}_{\boldsymbol{u}} = \hat{\boldsymbol{\sigma}}_{\boldsymbol{u}}(\boldsymbol{v}, q)$ is the adjoint stress, where $\boldsymbol{v}$ is adjoint velocity field and q is the adjoint pressure,

$$\hat{\boldsymbol{\sigma}}_{\boldsymbol{u}} = 2\Big(\eta(\dot{\varepsilon}_{\mathrm{II}}, \Gamma, n, \sigma_y)\mathbb{I} + \frac{1}{2}\eta_{,\dot{\varepsilon}_{\mathrm{II}}}[\dot{\boldsymbol{\varepsilon}}(\boldsymbol{u}) \otimes \dot{\boldsymbol{\varepsilon}}(\boldsymbol{u})]\Big)\dot{\boldsymbol{\varepsilon}}(\boldsymbol{v}) - q\mathbf{I} \tag{4.35}$$

and

$$\eta_{,\dot{\varepsilon}_{\mathrm{II}}} = \begin{cases} \min\Big(0, \frac{1}{2}\Gamma a(T)(\dot{\varepsilon}_{\mathrm{II}} - d)^{\frac{1}{2n}} \dot{\varepsilon}_{\mathrm{II}}^{-\frac{1}{2}} \frac{\dot{\varepsilon}_{\mathrm{II}} - (\dot{\varepsilon}_{\mathrm{II}} - d)n}{\dot{\varepsilon}_{\mathrm{II}}(\dot{\varepsilon}_{\mathrm{II}} - d)n}\Big) & \text{in } \Omega \setminus \Omega_y \\ -\frac{1}{2}\sigma_y \dot{\varepsilon}_{\mathrm{II}}^{-\frac{3}{2}} & \text{in } \Omega_y. \end{cases} \tag{4.36}$$

and $\otimes$ is the outer vector product and $\mathbb{I}$ is the fourth-order identity tensor. The gradient is then,

$$\mathcal{G} := \int_\Omega 2\eta_{,i}(\dot{\varepsilon}_{\mathrm{II}}, \Gamma, n, \sigma_y)\dot{\boldsymbol{\varepsilon}}(\boldsymbol{u}) : \dot{\boldsymbol{\varepsilon}}(\boldsymbol{v}) d\Omega - (\overline{\eta}_i - \exp \int \ln \eta)(\exp\{\int \ln \eta\}) \int \frac{\eta_{,i}}{\eta} d\Omega_i. \tag{4.37}$$

The additional term on the right hand side of (4.37) arises from the viscosity misfit which is a function of the inferred parameters such as the strain rate exponent and yield stress.

Priors

We have pre-existing knowledge on the rheological parameters controlling the deformation of mantle materials at high temperatures from laboratory experiments Ranalli, 1995, although those are generally performed at substantially larger strain rates than the values of $10^{-15}s^{-1}$, typical of mantle flow (Korenaga and Karato, 2008). Nevertheless, those estimates can be incorporated as prior knowledge into the optimization using Bayes Theorem (Eq. (4.3)), recalling that $\boldsymbol{\pi}_{prior}$ is the distribution that represents prior knowledge of the parameters. However, the parameters from laboratory experiments vary depending on what type of conditions are present such as the strain rate exponent for either wet or dry olivine. Therefore, the variance (uncertainty) in the prior distribution should reflect the lack of certainty of the range of values a rheological parameters should be.

Choosing the prior distribution for various rheological parameters can be difficult as there is often not enough information to constrain their mean and variance. The prior distribution of the rheological parameters such as the strain rate exponent are chosen such that they reflect the acceptable parameter range that can explain the rate of deformation from laboratory experiments. However, the acceptable values from laboratory experiments may not follow a Gaussian distribution (Korenaga and Karato, 2008), and it is not apparent what distribution the prior should be. Typically, the prior distribution is chosen to be a normal distribution (Fig.4.1a). The mean (μ_{prior}) is usually chosen based on what a likely average value should be based on experiments or from the literature (Korenaga and Karato, 2008). However, the uncertainty in μ_{prior} is unknown and therefore the variance needs to be chosen with care so that the prior does not have a strong influence on the posterior.

Another possibility is to use a *non-informative prior* (Tarantola, 2005) which gives gives equal likelihood (equal probability) to each value such that no preference is given to a single value. Using non-informative priors can be advantageous when it is not apparent what an acceptable value is, such as the strength of a weak factor An example of a non-informative prior is a uniform distribution for the plate couplings

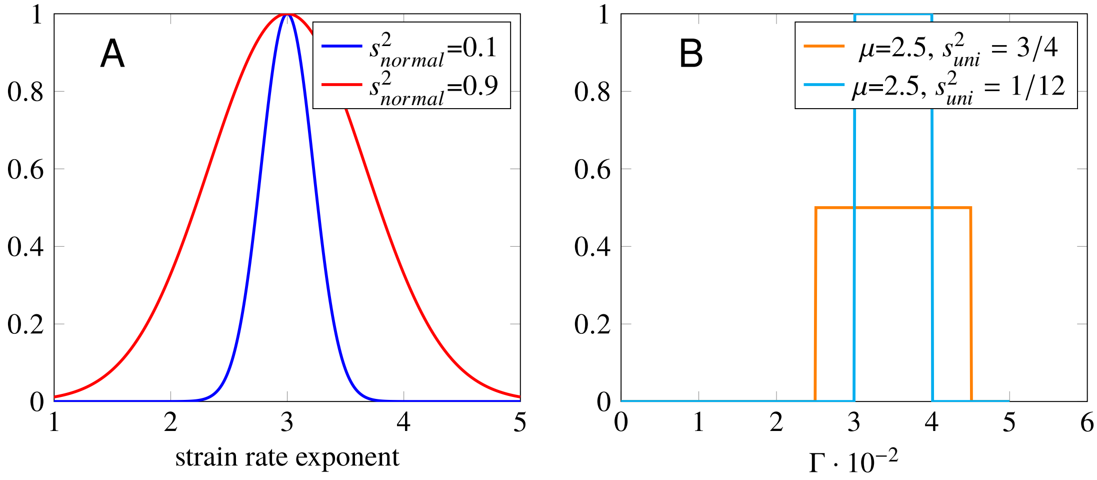

Figure 4.1: (A) Normal distributions for the strain rate exponent prior (B) Uniform distributions for the strain rate exponent prior. In (A) we compare the possibility of using two different normal distributions to demonstrate our knowledge or lack thereof of what the values of the strain rate exponent should be.

Γ_i (Fig.4.1b). A uniform distribution has the following properties,

$$\mathcal{U}(a,b) = \begin{cases} \frac{1}{b-a} & b \geq x \geq a \\ 0 & \text{otherwise} \end{cases} \tag{4.38}$$

with a mean and variance of

$$\mu(a,b) = \frac{1}{2}(a+b) \quad s^2_{uni}(a,b) = \frac{1}{12}(b-a)^2. \tag{4.39}$$

The uniform distributions (Fig. 4.1b) have the same mean, but different variance. Compared to a normal distribution, the variance for the uniform distribution is determined by the range of likely values, each of which has the same probability.

For a prior described by a normal distribution, a mean, μ, and covariance, C, are needed

$$\boldsymbol{\pi}_{prior} = \mathcal{N}(\mu, C) \tag{4.40}$$

The negative log of the prior distribution results in a weighted misfit, or

$$\mathcal{J}_{prior} = \frac{1}{2}(\boldsymbol{m} - \boldsymbol{m}_{mean})^\intercal C^{-1}(\boldsymbol{m} - \boldsymbol{m}_{mean}) \tag{4.41}$$

With the prior, the cost function would be

$$\begin{aligned} \mathcal{J}(\boldsymbol{u}, \boldsymbol{m}, p) &:= \frac{1}{2}\int_{\partial\Omega_1} (\boldsymbol{O}\boldsymbol{u} - \boldsymbol{u}_{\text{obs}})^\intercal C^{-1}_{vel}(\boldsymbol{O}\boldsymbol{u} - \boldsymbol{u}_{\text{obs}}) d\partial\Omega_1 \\ &\quad + (\eta_0 - \exp(\int_{\Omega_i} \ln \eta))^2 + \frac{1}{2}(\boldsymbol{m} - \boldsymbol{m}_{mean})^\intercal C^{-1}(\boldsymbol{m} - \boldsymbol{m}_{mean}). \end{aligned} \tag{4.42}$$

While the solution to the adjoint equation does not change, the gradient term for each parameter becomes

$$\mathcal{G} := \int_{\Omega} [2\eta_{,i}(\dot{\varepsilon}_{\mathrm{II}}, \Gamma, n, \sigma_y)\dot{\boldsymbol{\varepsilon}}(\boldsymbol{u}) : \dot{\boldsymbol{\varepsilon}}(\boldsymbol{v}) d\Omega + C^{-1}(\boldsymbol{m} - \boldsymbol{m}_{mean})\boldsymbol{m}_i d\boldsymbol{m}]. \tag{4.43}$$

These new gradients will be used to update the parameters as they measure the sensitivity of a parameter to an observation.

4.4 Model Setup

We have constructed a set of model constraints based on global observations with four components: A global temperature distribution, the geometry of faults, the kinematics of plate motion, and the geometry and bounds on the effective viscosity within selected regions of the mantle.

The temperature model has been constructed globally in a spherical shell from which selected cross-sections are taken. The temperature of oceanic lithosphere follows a half-space cooling model using updates to the digital grid of the age of oceanic plates (Müller et al., 1997). A thermal age was used within continents divided into the following three regions: Cratons (300 Ma), areas near subduction zones (75 Ma), and other areas (200 Ma), as detailed in (Stadler et al., 2010). The thermal structure of slabs were constructed as follows. Initially the top surface of the slabs was derived from the Slabs 1.0 surface, based on detailed seismic constraints, including seismicity and seismic reflection profiles (Hayes et al., 2012). With normals pointing downward from this surface, an initial thermal structure of slabs based on the half space model using the age of the plate at the position of the trench was generated. This procedure ensured continuity with the thermal structure of the oceanic lithosphere. Then, thermal conduction was solved for at each depth over a duration equal to the travel time to reach the depth with the local convergence velocity (using the relative velocity vector). Although solved only with conduction, this procedure resulted in thermal structures close to those obtained in fully dynamic models. The tops of thermal slabs were sharp in the corner of the mantle wedge and then progressively became more diffusive with depth. Within the lower mantle the thermal structure was based on scaled seismic tomographic models, including a P-wave (Simmons et al., 2012) and a S-wave model (Ritsema et al., 1999). The lithosphere and upper mantle models and the upper and lower mantle were blended together at 75 km and 550 km depths, respectively, as shown in cross sections (Fig.4.2). We have used the seismo-tectonic approach for the shallower mantle and tomographic approach for the deeper mantle, as the seismic tomography models for slabs tend to be spatially blotchy. Such blotchy structure is generally not consistent with Benioff zone seismicity and would map input variations in effective viscosity.

On the surface of the earth we generated a velocity field from MORVEL56 (Argus, Gordon, and DeMets, 2011) in a no net rotation (NNR) reference frame. Each cross-sectional model defines a great circle arc, with local unit vector **d** in the direction of the circle, such that we extracted the velocity $v_{xs} = \mathbf{d} \cdot \mathbf{v}$. The NNR reference frame was used as the side-walls on the two-dimensional cross sections preclude any large-scale differential motion between the bulk of the mantle and the plates, that is any net rotation.

Selecting a set of representative cross-sections in which all of the driving forces may be represented two-dimensionally is difficult, as it is likely that no plate and subduction zone is truly two-dimensional. Wide cross-sections with plate motion parallel to a great circle orthogonal to a subduction zone are rare and so we focused on smaller arc cross sections. Nevertheless, we have chosen a set of cross-sections in which plate motion was generally orthogonally to the strike of the trench, representing some of the end-member cases from the least to the most seismically coupled subduction zones (Fig.4.2A). To investigate the mechanical coupling for subduction zones with various degrees of seismic coupling, we consider the cross-sections in Fig. 4.2. Our primary cross-section has the largest dimension (about 240°, WEP, western to eastern Pacific) and contains three subduction zones that span the range from the seismically coupled (Chile) to the least coupled (Marianas). This cross section contains one subduction zone with back-arc extension near the Mariana trench. Additional cross-sections in Fig.4.2 are smaller than WEP, and thus do not contain the coupling variability of the larger cross-section; however those cross-sections represent subduction zones that exhibit both substantial coupling (Sumatra) and little coupling (Tonga).

The fault zone between converging plates at subduction zones, generally thought to be the places on which great earthquakes occur, were represented as weak zones with unknown viscosity. A weak zone factor, created by a stencil with a center line defined by the Slabs 1.0 surface (Hayes et al., 2012), was defined as

$$\Gamma_{stencil} = 1.0 - (1 - \Gamma_i)\exp\{-(d_i - d_0)^2/(2 \cdot w^2)\} \tag{4.44}$$

and with a coefficient Γ_i that was recovered in (4.2), d_0 is the center-line profile, w is the length-scale of smoothing for the weak zone. For our models, we assume the values of mantle parameters summarized in Table 4.1.

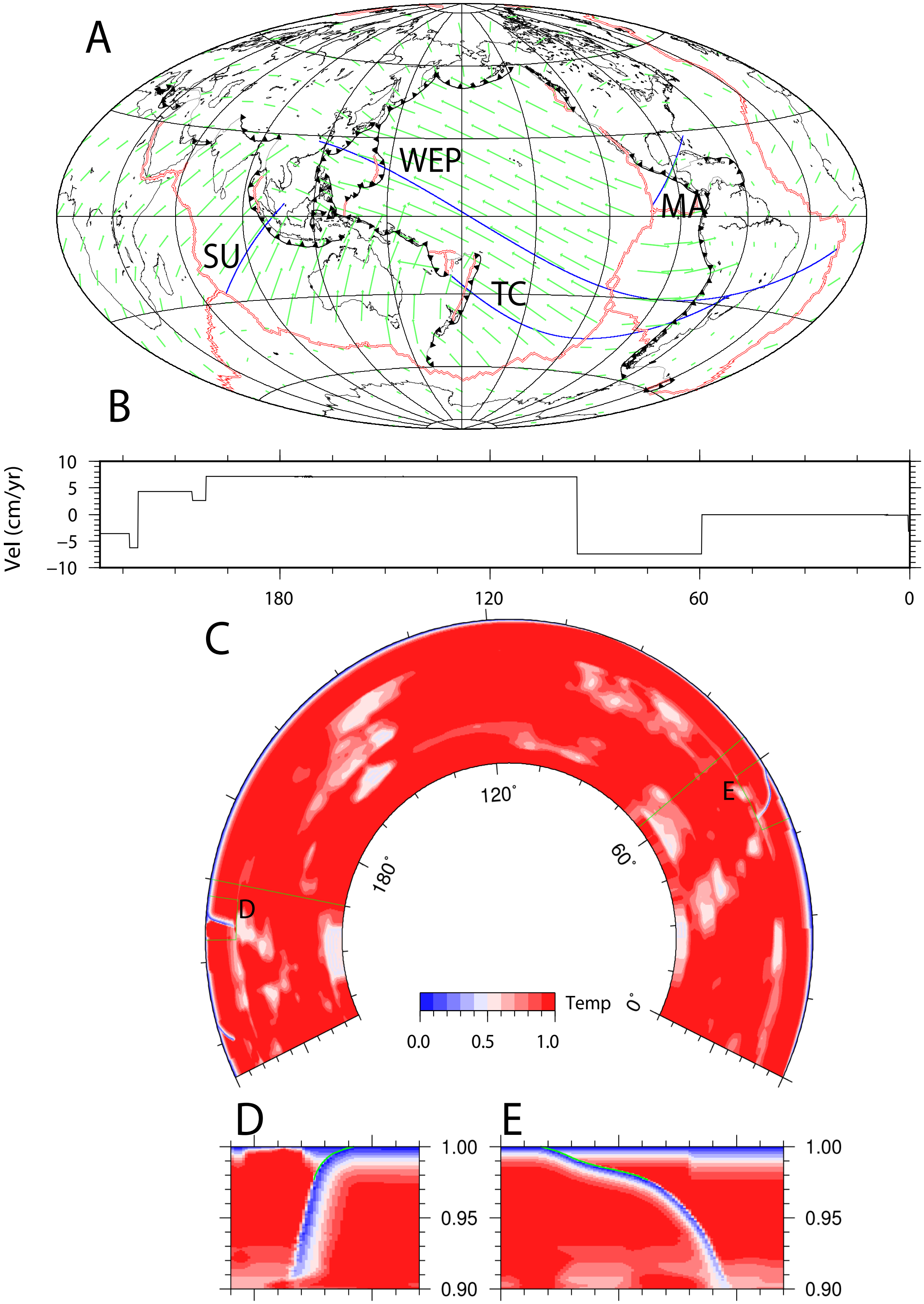
A
WEP
MA
SU
TC
B
Vel (cm/yr)
10
5
0
−5
−10
180
120
60
0
C
E
120°
60°
180°
D
Temp
0.0
0.5
1.0
0°
D
E
1.00
0.95
0.90
1.00
0.95
0.90

Figure 4.2: A. Velocity vectors in the no net rotation reference frame from MORVEL56(Argus, Gordon, and DeMets, 2011). Cross sections indicated with black lines, including western to eastern Pacific (WEP), Sumatra (SU), Tonga to Chile (TC) and Middle America (MA) B. Velocity in the direction of cross-section WEP.(C)Temperature distribution for cross section WEP. Zoom in of the Marianas (in D) and the Chilean (in E) slabs for the WEP cross section. In D and E, the solid green lines show the position of the weak zones.

Table 4.1: Assumed parameters left as constants in the

Symbol	Parameter	Value
ρ	Density (ρ)	3300 kg/m^3
g	Gravity (g)	9.81 m/s^2
α	Coefficient of Thermal expansion (α)	2×10^{-5}
ΔT	Temperature Difference ΔT	1400 K
D	Depth of layer (D)	1500 km
κ	Thermal Diffusivity (κ)	10^{-6} m^2/s
η_{ref}	Reference Viscosity (η_{ref})	10^{20} Pa · s
Ra	Rayleigh Number (Ra)	2.92×10^9
n	Strain rate exponent in lower mantle (n)	1.0

The average effective viscosity data is an additional constraint that we will explore to determine the effect it has on the inference of the rheological parameters. Since the effective viscosity is a constraint on the mantle from observations, then this data should better constrain global parameters such as the strain rate exponent, activation energy, and upper mantle prefactors. We will place the average effective viscosity constraint of $\overline{\eta}_j = 10^{21} Pa \cdot s$ under the South American continent (as it is the only plate in our models in the WEP cross section with a substantial continental plate overriding a subduction zone, Fig. 4.3B).

While we are able to solve this nonlinear Stokes flow, we need to resolve the thermal boundary layers and fault zones which requires either using small elements with uniform refinement, which would be computationally expensive, or adaptive mesh refinement (AMR), which is algorithmically more complicated. Here, we use AMR and refine the mesh in areas such as oceanic plates, slabs, the mantle wedge, and fault zones (the latter with 5 km-sized elements). AMR is implemented with the *p4est* library (Burstedde, Wilcox, et al., 2011), which ensures a 2 to 1 ordering for adjacent elements. Furthermore, we use quadratic elements for velocity along with first order discontinuous elements for pressure to ensure mass conservation. Resolving the fine scale structures of the thermal boundary layers and fault zones is part of the process of solving the nonlinear Stokes equations; however, to accurately solve the Stokes system, we need to either use Picard or Newton's method (both being iterative) obtain accurate flow velocities and the effective viscosity structure. While employing Picard is simpler to implement, it falls short in reduction of the residual of the Stokes system compared to Newton's method per iteration. Furthermore, the convergence obtained by Newton's method is significantly faster than Picard and results in a larger reduction of the residual of the Stokes system (Rudi et al., 2015). In addition to a significant reduction of the nonlinear residual of the Stokes system, solving the Stokes flow problem by an inexact Newton-Krylov method requires linearizing the nonlinear Stokes equation (providing the adjoint equation). Thus to solve the linearized Stokes system, we employ iterative Krylov (GMRES) solver while using multigrid methods (both algebraic and geometric), that are based on MATVEC methods which computes the action of a matrix on a vector, thus reducing the computational time of a forward solve. Furthermore, the solver employs a Schur-complement approximation that is based on a hybrid-spectral-geometric-algebraic multigrid approach detailed in (Rudi et al., 2015), which has a sequence of spectral coarsening of polynomial order, followed by geometric and algebraic multigrid. Code validation is provided in (Rudi et al., 2015).

Choosing a sufficient resolution for the forward model is important as it can influence what the inferred parameters are. We use a $5km$ element resolution within the fault zone, while resolving thermal boundary layers and this has been demonstrated to result in converged solutions. To determine if $5km$ element resolution is sufficient, we looked at $2.5km$ and $10km$ resolution by taking a model case such as Middle America that constrained plate motion data. We find that a $10km$ resolution is too large and results in an L^2 norm error of 8.44, while a resolution of $2.5km$ gives an L^2 error of $7.76 \cdot 10^{-4}$, approximately a 4-order magnitude difference. When comparing the error to that of $5km$ resolution ($7.76 \cdot 10^{-4}$), we find that a $5km$ resolution is appropriate as there is very little difference between both $2.5km$ vs $5km$ resolution. We completed a similar analysis for the WEP cross-sectional models and found that $5km$ resolution with the weak zones lead to convergent solutions.

For each of cross-section, we solve the forward models in a cut out of a sphere; that is, while the geometry is a two-dimensional domain and resembles a cylindrical geometry, the flow is computed in a spherical coordinate system. It is possible that the solution to the Stokes flow in a cut-out of a cylinder would change the forward outputs (effective viscosity, plate motions); however, the salient geophysical behavior of the solution should be similar and all of the critical dynamics of slab pull, bending in the hinge zone, and shear weakening occur at shallow depths where the differences between the geometries is small.

An important part of our inversions is the plate motion data (MORVEL56-NNR), which contains the plate motions along with their uncertainties. To account for the uncertainty in plate motion data, we use a diagonal covariance matrix of 0.1 mm/year uncertainty for each plate, similar to what was done in (Ratnaswamy et al., 2015). While (Argus, Gordon, and DeMets, 2011) provided a covariance matrix for the correlations between each of the 56 plates, we find that there are inconsistencies in their uncertainty when analyzing their covariance matrix–specifically the lack of positive-definiteness of their covariance matrix. Therefore, using a realistic variance for each plate is a reasonable compromise, though we do so at the expense of a realistic representation of the data uncertainty.

4.5 Results

Overview and stability

We infer rheological parameters that best fit observed plate motions. Unlike earlier use of a forward-adjoint Stokes optimization (Ratnaswamy et al., 2015) where the rheological parameters were known, here they are not. While inferring parameters, we ensure that the misfit with plate motions is minimized by reducing the norm of the gradient by three orders of magnitude, which lead to a goodness of fit ($\chi^2 < \mathcal{O}(10^{-5})$). In the context of earlier work (Ratnaswamy et al., 2015) in which conditional and marginal distributions were computed through repeated forward solves (without assumptions on their form using MCMC), we found that the distributions were smooth, without local minima, and well approximated by assuming that they are Gaussian near the best fitting values. We test the sensitivity of inferences on the initial guess of strain rate exponent, n, to rule out the existence of multiple or local minimas in the new inversions. For our standard case (Case 1), using the wide western to eastern Pacific (WEP) cross section with n, σ_y and plate couplings inferred, we find no sensitivity on the initial guess of n ranging from 2.0 to 3.5 (Table 4.2). This confirms that the posterior distribution for this particular set of parameters constrained by the velocity data is sufficiently smooth with no local minima and establishes that multiple inversions with different guesses are not required to confidently infer these rheological parameters.

Looking at Case 1 ($\chi^2 = 6.15 \cdot 10^{-6}$) in detail, the inversion rapidly minimizes the

Table 4.2: Sensitivity of initial guesses for Case 1

n_{guess}	n_{infer}	σ_y	Γ(SAM/RYU/IZU) $\cdot 10^{-5}$
2.0	3.079	137.01	62.39/0.7109/0.742
2.95	3.079	136.99	62.4/0.7109/0.7409
3.5	3.079	137.02	62.4/0.711/0.742

cost function during several iterations with the forward velocity converging toward the plate motion data, including the major plates as well as small plates in the back-arc (Fig. 4.3B). The effective viscosity varies between 10^{18} and 10^{24} Pa-s with major strain thinning within the upper mantle below the plates and weakening in the hinge zone of each subducting plate (Fig. 4.3A). Besides the larger cross-section (WEP) we also use three other smaller cross sections with different regional structure (slab dip and length, for example) and different expected degrees of coupling. We use the coupled Middle America subduction zone and configuration to illustrate the non-linear feedbacks which occur in this plate-mantle system. We start with a typical inversion in which the non-linear exponent, yield stress, and coupling factors are all left free, Case 32 ($\chi^2 = 6.92 \cdot 10^{-6}$); the inversion gives $\Gamma = 7.75 \times 10^{-5}$ during convergence to the observed velocity of the subducting plate (6.83 cm/yr). We see a moderate amount of shear thinning below the subducting plate (Fig. 4.4A) and some around the slab as evident through the reduction of effective viscosity; there is yielding within the hinge zone (Fig. 4.4B). In a forward model with all parameters set to the values in Case 32 ($\chi^2 = 6.05 \cdot 10^{-7}$), except for an increase in the value of the coupling factor (to $\Gamma = 4 \cdot 10^{-3}$) we see a distinct reduction in the amount of shear thinning around the slab and a reduction in the amount of hinge zone yielding (Fig. 4.4C) as the subducting plate velocity reduces to 3.79 cm/yr. However, when the coupling factor is decreased by only a small amount (to $\Gamma = 4 \cdot 10^{-5}$), the plate velocity increases modestly to 7.61 cm/yr but the amount of strain rate weakening increases substantially as evident through a much expanded area of reduced effective viscosity below the plate and around the slab; in addition the degree of yielding within the hinge zone expands (Fig. 4.4D). This interplay between the rheological parameters is important and demonstrates a strong interaction between the global rheological parameters (yield stress and strain rate exponent) and local coupling parameter. The forward models well illustrate the tradeoffs that will be expected between the inferred rheological parameters in the inverse models.

Returning to inversion with Case 1, the five parameters, n, σ_y and the three coupling factors all converge to stable values in about seven iterations (Fig. 4.3C-E). The nonlinear exponent is 3.08, the yield stress is 137 MPa and the coupling factors show a clear difference between Ryukyu and Mariana (with about the same small coupling values) and Chile with a much larger coupling value (Table 4.5). The actual, dimensional stress on these shear zones requires another adjoint solve, considered below.

With the stability of inversion established, we now systematically infer rheological parameters and the influence of the choice of which parameters are retained in the inversion. In subsequent sections, we will isolate parameter trade-offs, and determine the influence of adding additional viscosity data and prior knowledge. Starting with the larger cross-section (WEP), we hold fixed different combinations of strain rate exponent, yield stress, activation energy and upper mantle prefactor in Cases 2-5, all variants of Case 1; in all inversions the plate couplings are left free. The range of inferred strain rate exponent lies within 3.05 to 3.09, the yield stress lies within 130 to 143 MPa, and the activation energy, E_a, lies within 199 to 233 kJ/mol. In the least restrictive inversion (Case 6) with all of the rheological parameters left free, the non-linear exponent, yield stress and plate couplings all converge with stable values in about seven iterations (Fig. 4.3D-E). The inferred ordering of the coupling factors and their inferred values only varies by a small amount compared to the $\sim 10^2\times$ change between the low coupling values of Ryukyu and Mariana compared to the large value for Chile. The rheological parameters and coupling values appear to be robustly inferred with this set of input data.

The Sumatra and Tonga subduction zones are of particular interest as they are thought to be among the most and the least seismically coupled subduction zones, respectively. Therefore, we repeat similar sets of cases for these additional cross sections, for Sumatra, Middle America, and Tonga. The global rheological parameters strain-rate exponent and yield stress generally recover values within the range found from the WEP cross section. Only small differences are found: n can be as high as 3.12 for Sumatra and Middle America and the smallest yield stresses (127 MPa) occur for Tonga.

Conditionals

The uncertainty of inferred rheological parameters is examined through posterior distributions as conditionals. The conditional distributions convey not only uncertainty in each parameter and trade-offs between them, but they show how these parameters contribute to the underlying physics of plate mantle coupling. We find

Table 4.3: Summary of inversions (**bold** values held fixed)

Case	Subduction Zone	n	σ_y	Γ (CHL/RYU/MAR) $\cdot 10^{-5}$	UM Prefactor	$E_a(kJ/mol)$	Visc. data	Prior	Average $\eta_{UM}(10^{21})$	$\eta_{hinge}(10^{21})$
1	WEP	3.079	137	62.4/0.711/0.742	**2000**	**203.5**	no	no	3.96	7.59/8.71/8.07
2	WEP	3.072	139	64.7/0.702/0.781	**2000**	198.5	no	no	2.98	7.44/8.84/8.01
3	WEP	3.09	143	69.7/0.773/0.798	2098.9	**203.5**	no	no	4.47	7.40/8.31/7.97
4	WEP	**3.0**	129.5	63.3/0.703/0.725	**2000**	**203.5**	no	no	4.57	7.49/8.81/8.17
5	WEP	3.047	**120**	73.9/0.681/0.733	**2000**	**203.5**	no	no	3.11	7.38/8.89/8.13
6	WEP	3.066	141	69.8/0.656/0.745	3019.1	232.7	no	no	2.29	7.42/8.80/8.11
7	WEP	3.051	146	72.3/0.744/0.791	**2000**	**203.5**	no	yes	6.65	7.27/8.41/8.05
8	WEP	3.039	137	76.1/0.692/0.71	**2000**	217.7	no	yes	4.51	7.25/8.92/8.23
9	WEP	**3.0**	139	60.1/0.655/0.733	**2000**	**203.5**	no	yes	4.43	7.48/8.89/8.14
10	WEP	3.055	**120**	65.1/0.711/0.761	**2000**	**203.5**	no	yes	4.62	7.43/8.73/8.12
12	WEP	3.052	143	70.7/0.735/0.81	3471.4	230.4	yes	no	4.73	7.40/8.74/8.11
13	WEP	3.042	137	72.1/0.709/0.767	**2000**	**203.5**	yes	yes	3.79	7.37/8.79/8.14
14	WEP	3.047	135	69.8/0.726/0.799	4293.8	247.9	yes	yes	3.01	7.49/8.82/8.08
15	Sumatra	3.087	143.1	63.9	**2000**	**203.5**	no	no	3.61	7.79
16	Sumatra	3.11	141	44.1	3881.4	239.2	no	no	2.81	7.87
17	Sumatra	3.077	137	38.2	**2000**	200.1	no	no	2.04	7.89
18	Sumatra	**3.0**	129	30.7	2399.1	229.4	no	no	3.97	7.78
19	Sumatra	3.077	**120**	41.7	2604.3	227.6	no	no	1.89	7.88
20	Sumatra	3.048	143.1	63.9	**2000**	**203.5**	no	yes	3.61	7.51
21	Sumatra	3.1	138	40.3	3394.1	231.4	no	yes	1.94	7.85
22	Sumatra	**3.0**	128.1	38.2	2000	203.5	no	yes	3.07	7.88
23	Sumatra	3.063	**120**	34.8	2302.6	227.4	no	yes	3.55	7.90
24	Tonga	3.0621	139.1	0.63	**2000**	**203.5**	no	no	2.89	8.59
25	Tonga	3.051	135.2	0.7	3196.1	225.8	no	no	3.07	8.53
26	Tonga	3.087	**120**	0.83	2000	219.1	no	no	3.55	8.41
27	Tonga	**3.0**	127.7	0.67	3441.7	232.7	no	no	2.89	8.49
28	Tonga	3.076	139.1	0.74	**2000**	**203.5**	no	yes	3.97	8.45
29	Tonga	**3.0**	135.2	0.61	3014.9	217.4	no	yes	3.14	8.49
30	Tonga	3.097	**120**	0.73	3639.7	228.3	no	yes	3.29	8.40
31	Tonga	3.083	142	0.79	3492.3	225.8	no	yes	1.93	8.39
32	Middle America	3.0621	139.1	7.75	**2000**	**203.5**	no	no	3.1	8.95
33	Middle America	3.12	**120**	0.83	**2000**	178.1	no	no	1.89	8.9
34	Middle America	**3.0**	132.1	0.92	**2000**	207.2	no	no	4.29	8.86
35	Middle America	3.0	132.1	0.92	2000	207.2	no	no	4.29	8.86
36	Middle America	3.084	140	2.73	4091.4	241.8	no	no	3.11	8.73
37	Middle America	3.089	141	1.94	**2000**	**203.5**	no	yes	3.15	8.79
38	Middle America	3.092	143	1.06	3471.3	233.7	no	yes	2.98	8.87
39	Middle America	3.092	143	1.06	3471.3	233.7	no	yes	2.98	8.87

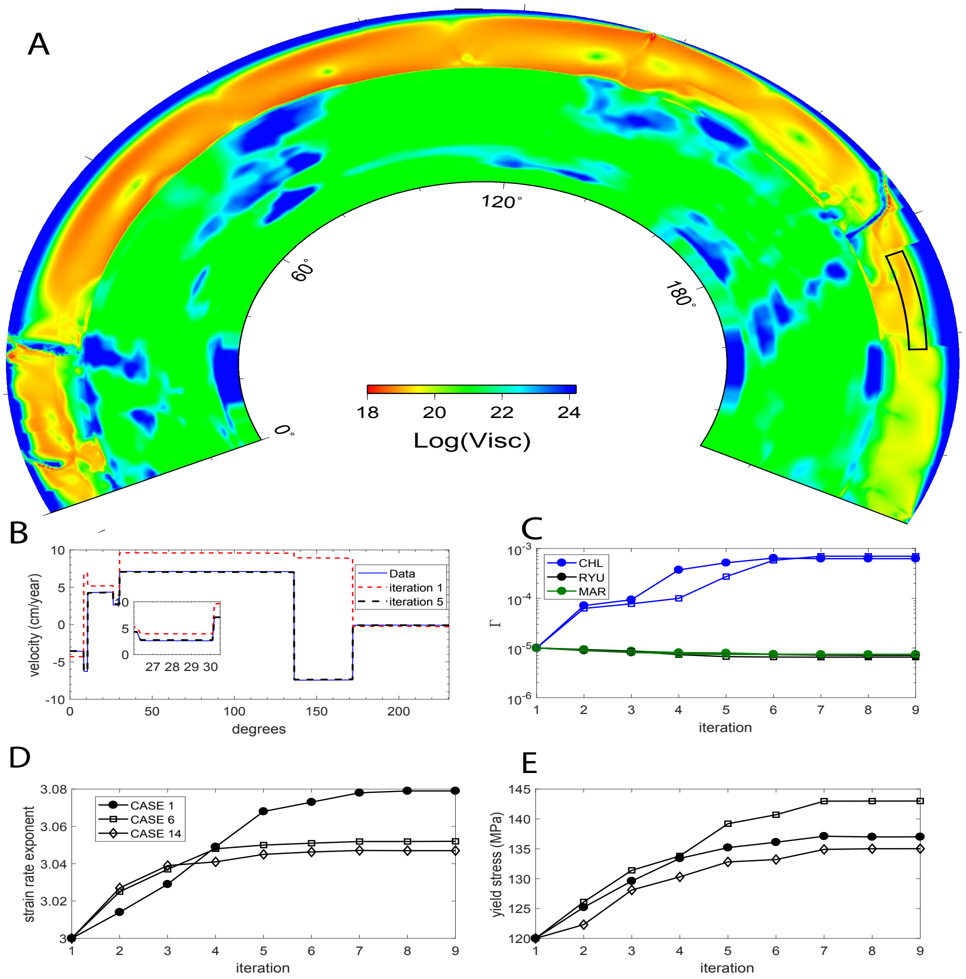

Figure 4.3: (A) Effective viscosity in the final converged state of Case 1 for the WEP cross section. Distance in degrees east along the great circle. (B) Case 1 surface velocity at two different iterations (dashed lines) compared with plate motion data (solid blue line). The velocity near the Mariana plate margin is shown in detail. (C) Convergence of coupling factors for Case 1 (solid circles) and Case 6 (open squares) for the Chile (CHL in blue), Ryukyu (RYU in black), and Mariana (MAR in green) plate margins. Convergence for the non-linear exponent (n, shown in D) and yield stress (σ_y, shown in E) for three cases (Case 1 and 6 have the same symbol as in C while Case 14 is shown with the open diamond symbols).

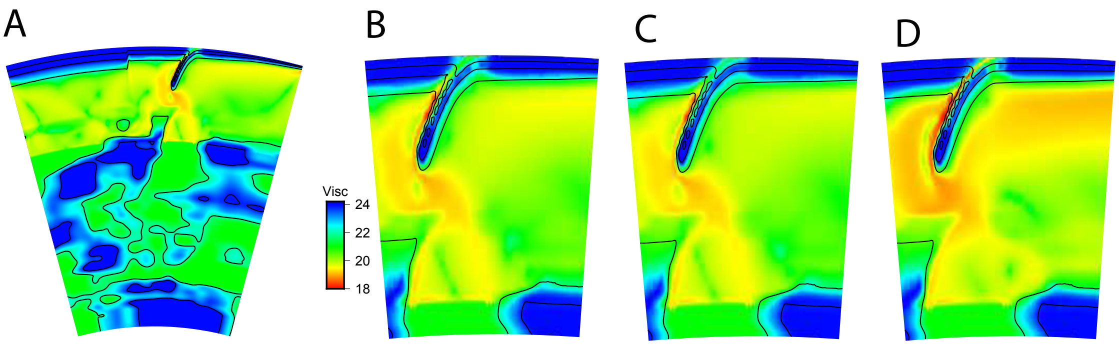

Figure 4.4: Effective viscosity for Middle America: (A) the inversion Case 32 ($\Gamma = 7.75 \cdot 10^{-5}$, $\sigma_y = 139.1$ MPa, and $n = 3.062$); (B) zoom in of Middle America slab from Case 32; (C) otherwise identical forward model except $\Gamma = 4.0 \cdot 10^{-3}$; (D) otherwise identical forward model except ($\Gamma = 4.0 \cdot 10^{-5}$).

conditionals by using the covariance matrix of model parameters through an inverse of the Hessian matrix, e.g. (4.19).

Using the conditionals for Case 1, we see a positive correlation between strain rate exponent and yield stress (Fig. 4.5A), a weak negative correlation between the plate couplings and yield stress (Fig. 4.5B) and a weak positive correlation between plate couplings and strain rate exponent (Fig. 4.5C). Yield stress, σ_y, and strain-rate exponent, n, both control the degree of nonlinearity of the system; nonlinearity increases with larger n, so σ_y must increase in order to fit the kinematic constraints. The positive correlation between the strain rate exponent and yield stress suggests that as the strain rate exponent increases, upper mantle viscosity decreases and the drag on the base of plates decrease, but resistance in the hinge zone must increase to fit the kinematic constraint achieved with an increase in yield stress. Likewise, an increase in plate coupling could be accomplished through either changes in n or σ_y. One means would be a decrease in upper mantle viscosity realized by a larger non-linear exponent, n; an alternative means is accomplished through a decrease in hinge viscosity realized through a reduction in yield stress.

The differences in the coupling factors for different subduction zones are best shown using the conditional distributions; for Case 1 (Fig. 4.5B,C), we find that there is a clear demarcation between Ryukyu and Marianas the least mechanically coupled subduction zones and Chile and this conclusion is independent of the non-linear exponent and yield stress, in spite of the large variance of global rheological parameters. The variance on the nonlinear exponent n is quite large, 0.67, that is

$n = 3.08 \pm 0.67$. We have repeated the inversions for the smaller cross sections (leaving only n, σ_y and coupling factors free) and we find that the MAP points of n and σ_y are close to values inferred from either the larger WEP or any of the three smaller cross sections. However, the variance on n is reduced somewhat in the small cross sectional models compared to the wide cross sectional WEP models. We again find a clear demarcation between the coupling factors with a low coupling value for Tonga and Middle America and a high value for Sumatra. Middle America has a larger coupling factor compared with Tonga at greater than a 95% confidence level.

The coupling factors are intrinsic quantities, not depending on the forces in a particular subduction zone or case. Using just the kinematic data, in conjunction with the geometry and amplitude of the driving forces (e.g. temperature distribution), the partitioning of the subduction zones into distinct groups suggest that the Chilean and Sumatran plate boundaries are more mechanically coupled compared to Ryukyu, Marianas, and Tonga regardless of the global parameter (yield stress and strain rate exponent).

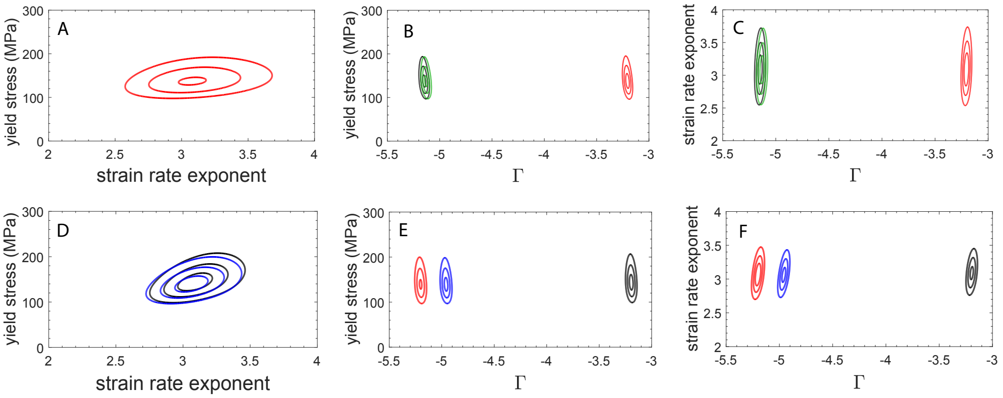

Figure 4.5: Case 1: Strain rate exponent vs. yield stress (A), yield stress vs. plate coupling (B), and strain rate exponent vs. plate coupline (C). Chile (red), Ryukyu (black) and Marianas (green). Cases 15, 24 and 32 (Sumatra in black, Tonga in red and Middle America in blue): Yield stress vs. strain rate exponent (D), yield stress vs. plate coupling (E), and non-linear exponent vs. plate coupling (F). Contour levels correspond to 30%, 60% and 90% probabilities.

Adding priors

Priors are introduced with Gaussian distributions for each of the inferred parameters assuring that we do not restrict the likelihood to a particular parameter space. Repeating a set of inversions in Cases 7-10 for the WEP cross section, we determine that the form of the correlations remain invariant, including a positive correlation between the strain rate exponent and yield stress (Fig. 4.6A). Furthermore, we confirm that the ordering of plate couplings, where Chile is more coupled than the Marianas and Ryukyu is also unchanged. The convergence of the parameters during the course of inversion remain close to 7 iterations such that adding priors does not substantially impact the overall computational work (Fig. S1). For the conditional distributions of E_a vs. n using generic, permissive priors, we find that the activation energy remains around 200 kJ/mol and the non-linear exponent remains around 3.1 with the variance on both reduced somewhat for both the WEP and Sumatra cross sections with priors (Fig. 4.6A,B).

Instead of generic priors, we now turn to the use of prior knowledge from rock mechanics experiments. We use priors of $E_a = 550$ kJ/mol and $n = 3.5$ which are typical values for olivine in a dislocation creep regime (Karato and Wu, 1993). We use a large generic, permissive variance on these values and find a distinct shift in both the recovered activation energy and non-linear exponents to higher values (from $E_a = 233$ to 312 kJ/mol) and from $n = 3.1$ to about 3.35, but the strain rate exponent does not overlap with $n = 3.5$ at the 95% confidence interval (Fig. 4.6C). With the use of these priors, we see a distinct shift to parameter values that would tend to change the viscosity of the slab; the activation energy shifts to larger values (which by itself would increase the viscosity of slabs) coupled with a shift to larger stress-strain rate exponents, which would tend to decrease the viscosity of slabs. Only if we make priors restrictive, that is by reducing the variance on the priors by an order of magnitude from $5 \cdot 10^{-2}$ to $5 \cdot 10^{-3}$ are we able to recover a value near the 550 kJ/mol from rock mechanics, but significantly the posterior distribution of n still fails to overlap with $n = 3.5$ at greater than a 95% confidence level (Fig. 4.6D-red contours). With these more restrictive variances on the priors for n, E_a, and σ_y, the overall ordering of the coupling factors Γ remains the same, with Chile more coupled than the Marianas or Ryukyu, however, the coupling factor for the later two uncoupled subduction zones have jumped by an order of magnitude (Fig. 4.6E). Interestingly, E_a and n have both jumped significantly (Fig. 4.6D), but the viscosity for these hinge zones (Table 4.5) remains nearly the same, around 8×10^{21} Pa-s. With a substantial jump in the non-linear exponent n, though, there is now much more shear thinning in the upper mantle and so some of the coupling factors, in turn, have increased.

Inclusion of viscosity data

We now include constraints on the average effective viscosity below continental cratons as data in the inversions, for example as indicated in the WEP cross section (Fig. 4.3C). In Fig.4.10A we see the conditional distributions without the viscosity data (Case 6) and with the viscosity data (Case 12) for WEP. The additional effective viscosity data acts as prior information and marginally reduces the uncertainty on the inferred parameters. By including the viscosity constraint as a value within the upper mantle below the continental lithosphere, the viscosity there has increased somewhat in Case 12 compared to Case 6 without the constraint. However, more importantly, at the scale of the entire conditional distributions the inference of either upper mantle viscosity or the non-linear exponent has not changed substantially (Fig.4.10A). Moreover, the yield stress, coupling factors, activation energy and resulting hinge zone viscosities (considered below) have not changed appreciably (Table 4.5).

Inference of fault zone stresses

The stress on faults is a fundamental quantity in arguments on the origin of variation in megathrust behavior along strike and between subduction zones. Fault zone stress is an extrinsic quantity and is not in our set of unknown model parameters, **m**. Stress is a function of both model parameters and forces and an additional adjoint solve allows the inference of the optimal shear and normal stress within the plate boundaries and the covariance with **m**.

Using optimizations in which all of the rheological parameters are left free and with no prior knowledge or inclusion of viscosity data (Case 6 for WEP and Cases 16, 25 and 35 for Sumatra, Tonga and Middle America, respectively) we see a consistent pattern (Fig. 4.7). The shear and normal stresses are small and only vary between about 7 and 16 MPa for all of the plate boundaries considered. For the more shallow dipping and more mechanically coupled boundaries, Chile and Sumatra, the shear stresses are about 25% larger than the normal stresses. In these boundaries with a gradually curving subduction interface, the motion of the subducting plate imposes a shear flow, a Couette flow, within the low viscosity channel (i.e. the weak zone) and these shear stresses resist plate motion.

We further examine the stresses in the fault zone and plates by computing the principal stress axes in Figs.(4.8,4.9) for Case 6 for WEP and Cases 16, 25 and 35 for Sumatra, Tonga and Middle America, respectively. We find that a state of compression dominates the fault-zone for the more coupled subduction zones (Sumatra and Chile) in Fig.4.8b,d, compared to Middle America, Ryukyu and Marianas in Fig.4.8a,c and e respectively. Furthermore, we find that fault zones such as Sumatra and Chile that have a pattern of compressive stresses within the fault zone tend to have slabs that are in a state of tension, while the overriding plate is in a state of compression (Fig.4.9b,d), while the converse is true for Middle America, Ryukyu and Marianas (Fig.4.8a,c and e).

Hinge zone viscosity

The yield stress governs weakening in the hinge zone and relieves otherwise large stresses as plates bend. The inferred yield stress is in the range of 130-146 MPa through all of the inversions considered (Table 4.5). Dynamic weakening does occur within the hinge zone, evident by the reduction in the effective viscosity (Fig. 4.3A). Furthermore, in Cases 1-6, the average effective viscosity in the hinge zone is approximately 7-9 10^{21} Pa s, regardless of which combination of the parameters are inferred, suggesting that there is a bounded effective viscosity in the hinge zone that best minimizes the misfit in observed plate motions and model results. Given the rather small range of all of the inverted hinge zone viscosities, we see no appreciable change among the three subduction zones in the WEP cross section (Fig. 4.10B). Despite the large variation in the recovered coupling values for these three subduction zones, when yielding is made a single global parameter, there does not seem to be any variation in hinge zone viscosities between subduction zones.

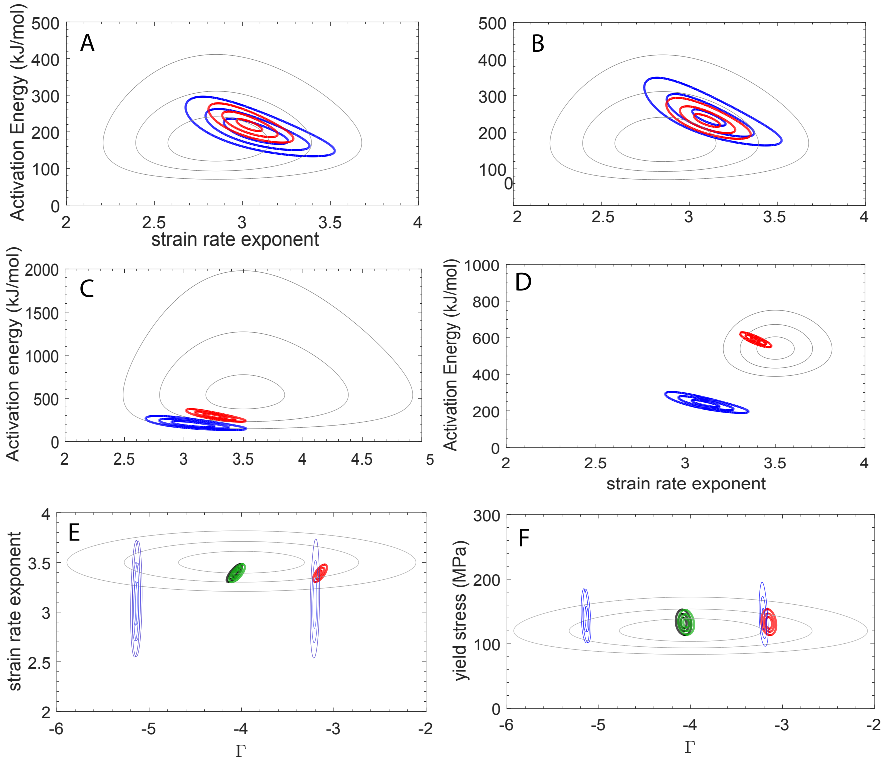

Figure 4.6: The influence of priors on the conditional distribution of activation energy vs. strain rate exponent. Generic priors on (A) WEP and (B) Sumatra. For the WEP cross section, conditional distribution with permissive (C) and restrictive prior knowledge (D). Throughout, thin black contours are the priors, thick blue ones are conditionals without priors, and thick red ones are those with priors. (E) WEP model comparison for no-priors (blue contours) and restrictive priors (Γ_i vs. strain rate exponent) (F) WEP model comparison for no-priors (blue contours) and restrictive priors (Γ_i vs yield stress). Contour levels correspond to 30%, 60% and 90% probabilities.

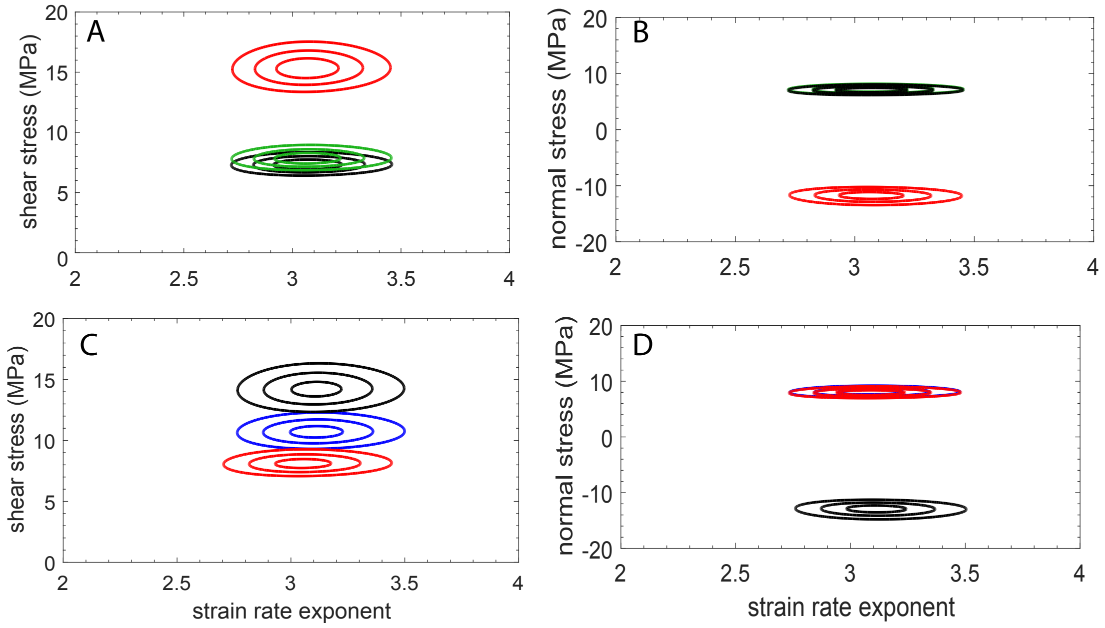

Figure 4.7: Fault zone stresses (Tensile stresses are positive while compressive are negative). Results for the WEP with Case 6 with Chile (red), Ryukyu (black) and the Marianas (green) resolved for the (A) stress stress and the (B) normal stress. Results for the Sumatra (black, Case 16), Tonga (red, Case 24) and Middle America (blue for Case 35) resolved for the (C) shear stress and (D) normal stress. Contour levels correspond to 30%, 60% and 90% probabilities.

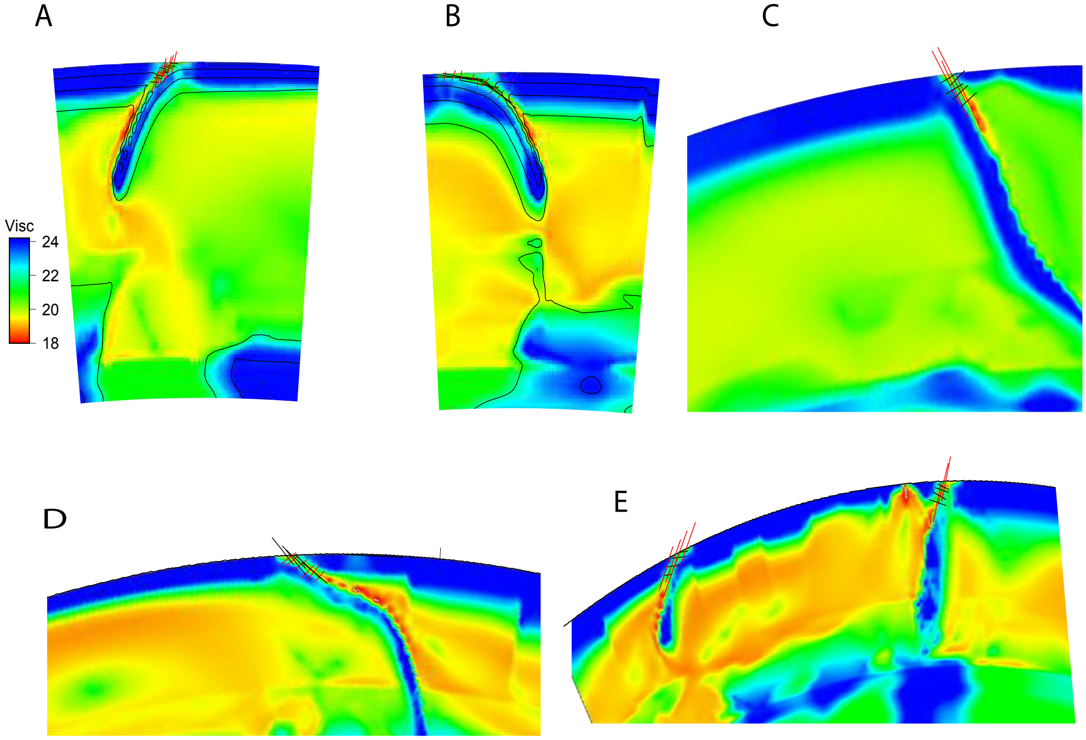

Figure 4.8: Principal stresses in the fault zones. Compression (-) and Tensional Axis (-) for (a)Middle America (Case 35) (b) Sumatra (Case 16) (c)Tonga (Case 24) (d)Chile (WEP) (e)Ryukyu and Marianas (WEP) Case 6 within the fault zone.

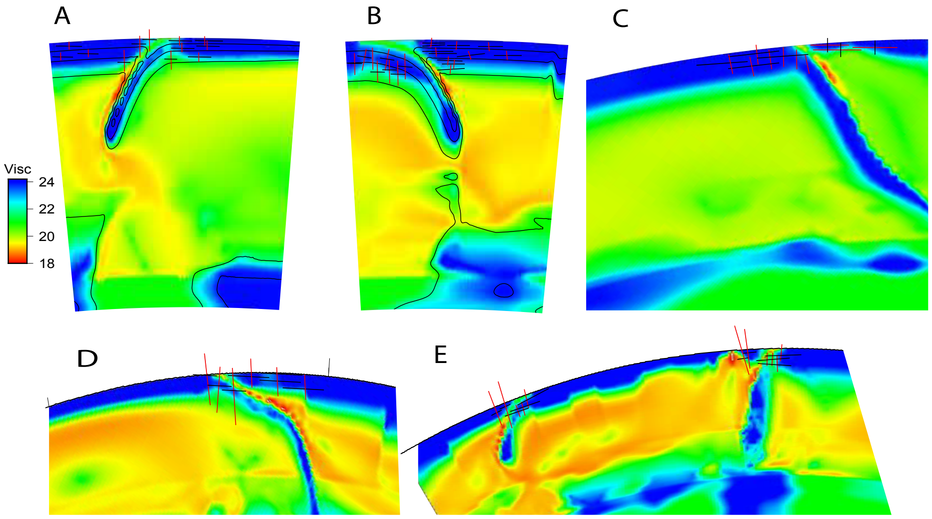

Figure 4.9: Principal stresses in the fault zones. Compression (-) and Tensional Axis (-) for (a)Middle America (Case 35) (b) Sumatra (Case 16) (c)Tonga (Case 24) (d)Chile (WEP) (e)Ryukyu and Marianas (WEP) Case 6 within the plates.

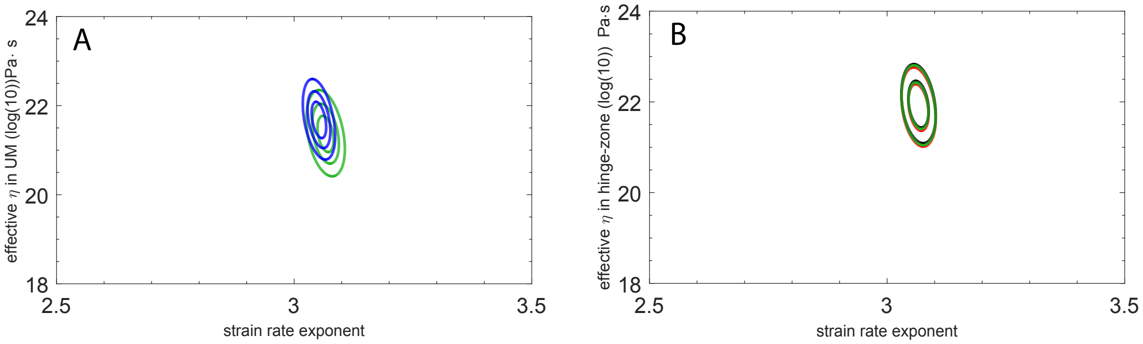

Figure 4.10: (A) Average effective viscosity vs. strain rate exponent in the upper mantle showing the influence of adding viscosity data to the inversion (blue, Case 12) compared to Case 6 without (green). (B) Average effective viscosity in hinge zones vs. strain rate exponent for Case 6. Note that all of the distributions are close for the three subduction zones in WEP and so they appear to overlie one another. Contour levels correspond to 30%, 60% and 90% probabilities.

4.6 Discussion

In our models here, we make several advances from our earlier work (Ratnaswamy et al., 2015) through the addition of effective viscosity data, using realistic temperature and fault zone structures from seismic models and plate motions, while estimating quantities of interest including the extrinsic stresses and average effective viscosities. Using these methods, we primarily focus on the inferred parameters and the geophysical implications from previous estimates through experiments. We considered four cross-sections: WEP, Sumatra, Tonga, and Middle America as they represent varying degrees of seismic coupling and therefore inferring the rheological parameters for each of these cross-sections can inform the degree to which the inferred parameters vary for each subduction zone. The WEP contains three subduction zones: Chile, Marianas, and Ryukyu, where the Chilean subduction zone is thought to be the most seismically coupled and the Marianas and Ryukyu are thought of among the least seismically coupled (Scholz and Campos, 2012).

We formally invert for the non-linear exponent n, a parameter that controls the amount of shear-thinning in the upper mantle. In Table 4.5, we find across all subduction zones that inferred strain rate exponent is < 3.5. The value we infer with and without non-restrictive priors is closer to what is assumed for wet olivine (Karato and Wu, 1993), suggesting that our cross-sectional models are more associated with wet olivine. However, when prior knowledge is used, we infer strain rate exponents for all four cross-sectional models in the range of 3.35-3.4, values that are closer to what is obtained for dry-olivine (Karato and Wu, 1993). The variance between the strain rate exponent varies substantially between using non-permissive prior knowledge and permissive knowledge due to the small variance used; however, this restrictive prior knowledge led to a shift in the MAP point for the strain rate exponent, while also influencing the activation energy and plate couplings. It should be noted, that we considered positive values of the strain rate exponent when imposing priors ($n > 0$); however, a velocity strengthening material may be possible for $n < 0$ that can give rise stick-slip motion (Bercovici, 1993). However, while (Bercovici, 1993) found that a value of $n = -1$ can produce plate-like behavior, the rheology that was used was a power-law rheology and did not consider yielding and a temperature dependent rheology.

The activation energy is a parameter that we explored in this study but not in our earlier one (Ratnaswamy et al., 2015). In our studies, we used a linearized-Arrehnius law, instead of the typical Arrehnius law (Billen and Hirth, 2007), which may have an effect on the inferred activation energy. In our inversions in Table 4.5, we find the inferred activation energy is in the range of 199 – 242 kJ/mol, which is less than what was found for both dry and wet olivine of 540 and 430 kJ/mol respectively (Karato and Wu, 1993) for dislocation creep. Comparatively, the inferred values in Table 4.5 compare more to the activation energy for the diffusion creep regime (Karato and Wu, 1993); however, when using prior knowledge (Fig.4.6), we find we can recover values in the range of 520 – 589 kJ/mol, which is in the range for both wet and dry olivine (Karato and Wu, 1993). A natural question arises as to which values are closer to the actual mantle values since the inversions depend on the type of priors used. The dynamics are similar in both cases, such that the average effective viscosity is similar: A weak upper mantle ($\eta \approx 10^{20} Pa \cdot s$), while the plates are strong. Since the average effective viscosity is conserved, the answer to that question depends on if experimental studies (Karato and Wu, 1993; Ranalli, 1995) are to be given more weight compared to allowing more emphasis on geophysical inversions alone (the likelihood).

While the activation energy and strain rate exponent are key in understanding the dynamics of plate motion, the yield stress is also key as it influences the bending resistance at the hinge zone. We find a yield stress in the range of 128 – 143 MPa. This value of the yield stress is 4x smaller compared to what was found in rock mechanics experiments ($600MPa$)(Mei et al., 2010). Potentially, a high yield stress found experimentally can be attributed to the extrapolation from laboratory strain rates to geological strain rates. In contrast to (Mei et al., 2010), estimates of 100-200 MPa have been made by comparing load induced deformation of the lithosphere. The inferred yield stress from our inversions are within the range 100 – 200 MPa (Zhong and Watts, 2013) compared to those from laboratory experiments (Mei et al., 2010) of 600 MPa and promote dynamic weakening in the hinge zone. Furthermore, for our models a value of 600 MPa, would be too large to promote dynamic weakening to reduce the bending force. This conclusion based on comparing mechanical models to generic plate motion values is in-line with previous studies using forward geodynamic models (Zhong and Gurnis, 1996; Moresi and Gurnis, 1996b). Additionally, if a large yield stress is used such that the bending force is not reduced, the amount of decoupling would increase to overcome the bending force.

The other important part of our studies is the inference of the plate couplings Γ_i. With our models, we find a strong demarcation between the Chilean (largest coupling) vs. the Ryukyu and Marianas subduction zone. To put this into context, we compare the variations in plate coupling to seismic coupling in Table 4.4, we find that the larger coupling for the Chilean subduction zone is similar to the large seismic coupling in Central Chile vs. Tonga. This result from our inversion, suggests that there may be a correlation between the large-scale mechanical couplings with the seismic couplings from (Scholz and Campos, 2012). Furthermore, we arrive at similar results in coupling distributions when using priors (restrictive and prior knowledge). In Fig.4.6, we find a similar partitioning of the mechanical coupling of Chile vs. Marianas and Ryukyu, suggesting that even with priors, the dynamics and plate boundaries from a viscous flow perspective suggests that the Chilean subduction zone is more coupled. Finally, we find a similar partitioning for Sumatra, Middle America and Tonga, where Sumatra is more coupled than Middle America and Tonga–a similar trend to what is found in seismic coupling.

The correlation between the weakfactor and yield stress is an emergent trade-off we see within all the cross-section models. We find that as the weakfactor increases, the channel in the fault zone becomes more viscous and there is a mild negative correlation with the yield stress. This negative correlation implies that when the weakfactor increases, there is a reduction in the yield stress which promotes weakening in the hinge zone to counter the increased resistance. In particular, we see that as yielding occurs as plates bend in the Nazca plate, we find that the weakfactor is comparably larger than Ryukyu and Marianas (where both of those subduction zones have less yielding). Similarly, this trade-off occurs in the Sumatra model, where we see that there is a significant amount of coupling while there is sufficient yielding within the slab. This trade-off between the weakfactor and yield stress comes about because the increased resistance from the plate coupling causes more weakening around the slab as it falls into the upper mantle. The Middle America cross-section represents the opposite case compared to Sumatra, that is, there is a decoupling between the overriding plate and subduction zone. This decoupling represents an increase in plate speed, therefore to compensate for the increase in plate velocity would require an increase in the bending force in the hinge zone-that is there would be an increase in the yield stress to increase the bending force.

While estimating the mechanical coupling between subduction zones, we looked at the stresses within the subduction zones while comparing to those provided by seismological constraints. We find that in all our cases (WEP, Sumatra, Middle America and Tonga) that the estimates of shear and normal stresses are less than 20 MPa (Brune et al., 1969), which satisfies seismological constraints, suggesting that

Table 4.4: Summary of seismic coupling coefficients (χ_s) is the seismic coupling coefficient, while χ_g is the geodetic coupling coefficient (Scholz and Campos, 2012).

Subduction Zone	χ_s	χ_g	$\sigma_n(MPa)$	$\sigma_t(MPa)$	Γ
Marianas	0.01	N/A	7.22	7.99	$7.42 \cdot 10^{-6}$
South Ryukyu	0.05	N/A	8.47	8.72	$9.11 \cdot 10^{-6}$
Central Chile	0.70	1.0	12.3	16.4	$7.02 \cdot 10^{-4}$
Sumatra	0.5-0.83	1.0	11.73	15.33	$3.93 \cdot 10^{-4}$
Middle America	0.10	0.20	9.22	10.23	$5.51 \cdot 10^{-5}$
North/South Tonga	0.66/0.14	N/A	7.32	8.74	$8.32 \cdot 10^{-5}$

the inferred rheological parameters give rise a reasonable state of stress. While the stress values are in the correct range, we find that the conditional distributions have bounds on how large the stresses are-which are under 20 MPa. Examining the stress conditionals for WEP (Fig. 4.7), we find that the **MAP** point for the shear stresses are consistently larger than those of the normal stresses. Many models of subduction with a frictional material have a shear stress that is a fraction of the normal stress.

Here, we have purely viscous flow, Couette flow in a low viscosity channel, adjacent to the moving slab. Looking at the normal stresses within the fault zones for Sumatra, Tonga and Middle America, we find that Sumatra is under a state of compression compared to Tonga and Middle America (Fig.4.7D). This state of compression can be attributed to the increased mechanical coupling compared to Tonga and Middle America. Comparing the state of compression of Sumatra to Tonga and Middle America, we find that both fault zones are in a state of tension, suggesting that there is a correlation between the mechanical coupling and the state of stress in the fault zones.

We also find in the WEP models, that the more mechanically coupled Chilean subduction zone is in compression (Fig.4.8D) compared to Marianas and Ryukyu (Fig.4.8E), which are are in tension. Furthermore, the state of stress in the Chilean subduction zone exhibits compression in the overriding plate, while tension in the subducting plate, while the opposite is true for Ryukyu and Marianas, where the subducting plate is in compression, while the overriding plate is in tension (Fig.4.9). The stresses in the conditional distributions align with what is found in the state of stress, suggesting that our estimation of the tangential stresses in a UQ sense is validated by the stress axis within the fault zone. We also note that the stress distribution within the plates favor a state of tension in the overriding plate while the subducting plate is in a state of compression when the fault zone is in a state of of tension. Conversely, the Chilean subduction zone gives rise to a compressive state of stress in the overriding plate while the subducting plate is in a state of tension when the fault zone is in a state of compression. Similarly, we see the same trend for the Sumatra, Middle America and Tonga (Fig. 4.8 and Fig. 4.9 A, B. and C).

The connection between the state of stress (Fig.4.8, 4.9) suggests that there may be a feedback between the mechanical coupling (Γ_i) and the broad-scale forces within plates and plate boundaries. We posit this relationship between both plate couplings and broad-scale tectonic forces because in our inversions the stresses within plate boundaries depends explicitly on the plate couplings (Γ_i) due to the rheology within plate boundaries. While, there is a dependence between the plate boundary stress and the plate couplings, it is certainly not clear from the outset whether it was either plate couplings, or tectonic forces that would partition seismically coupled subduction zones. Our exploration in both stresses and plate couplings is different than studies that focused on partitioning based on forces (Scholz and Campos, 1995; Scholz and Campos, 2012) or studies that focused on mechanical properties (Heuret et al., 2012) and seismic coupling, in that we looked at both these aspects and find that both mechanical properties and broad-scale forces may contribute to subduction zones that are strongly seismically coupled vs. those that are not.

The partitioning of the subduction zones, (both mechanically and from dynamic forces), and values of the inferred rheological parameters are specific to the plate motion data that we used (MORVEL56-NNR) and there may be a possibility that those parameters can increase and decrease. Using a different plate motion model that has net-rotation such as HS3-NUVEL1A (Gripp and Gordon, 2002). A natural question arises as to whether the mechanical and stress coupling remains the same (Fig.4.5 and Fig.4.7) will be needed to be explored in future studies. While a change in the magnitude of the rheological parameters would occur, the distribution of mechanical and thus stress couplings should not because the overall variations in plate motions are not substantial to warrant a much larger coupling in Ryukyu and Marianas. Furthermore, the nature of the slabs (dip angle, age) play a more crucial role in the determination of the forces, while the plate velocities are an outcome.

Ultimately, our inversions give rise to estimates of the strain rate exponent, yield stress and activation energy that are within the bounds found in laboratory experiments that are extrapolated to geological strain rates. Furthermore, we find that it may be the combination of both mechanical properties and broad-scale forces that give rise to great earthquakes based on our formulation of our models and the interplay between the large-scale forces and the rheology of the mantle. However, to test the robustness of the inferred rheological parameters, the extension of this work to global, spherical models will be needed as those models will contain both toroidal and poloidal nature of the flow-field of the mantle. With the use of spherical models, the conclusion that both mechanical properties and broad-scale forces can give rise to great earthquakes can be robustly tested and therefore build a connection between seismic coupling of subduction zones.

Supplementary Figures and Information

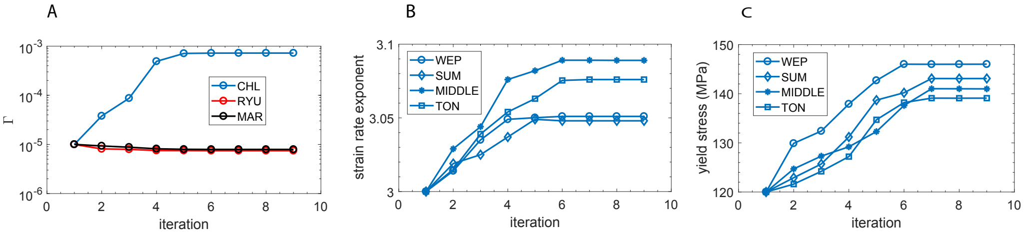

Figure 4.11: (A) Convergence for the plate couplings in Case 7 for WEP (b) convergence for the strain rate exponent (c) convergence for the yield stress (Case 7 for WEP, Case 20 for Sumatra, Case 37 for Middle America and Case 28 for Tonga).

Derived Covariance Estimates

We have previously set models in how to estimate quantities that are are inferred such as the stresses. In this section, we will thoroughly discuss how to apply this Gaussian approximation to various quantities of interest. Mapping of covariance matrices from one space to another requires a transformation,i.e. using the Jacobian. As an example, we will look at transforming a Gaussian distribution for the inferred yield stress and strain rate exponent, that is $\boldsymbol{\pi}(\boldsymbol{m}) := \mathcal{N}([n, \boldsymbol{\sigma}_y], C) \rightarrow \boldsymbol{\sigma}(\gamma \boldsymbol{m})$, where we look at the scaled space between the parameters. To determine the mapping of the covariance we make use of, Case 1: 1D Normal

$$\frac{\partial \boldsymbol{\sigma}}{\partial \boldsymbol{m}} = \gamma \tag{4.45}$$

leading to

$$\boldsymbol{\pi}_2 = \mathcal{N}(\mu, \gamma^2 \sigma) \tag{4.46}$$

Case 2: 2D Normal We consider the case when we apply a stretch factor in the form of $\gamma = [\gamma_1, \gamma_2]$, that is $\boldsymbol{m} = [\boldsymbol{m}_1, \boldsymbol{m}_2]$. Therefore $\boldsymbol{\sigma} = [\gamma_1 \boldsymbol{m}_1, \gamma_2 \boldsymbol{m}_2]$. The follwoing now holds

$$\frac{\partial \boldsymbol{\sigma}}{\partial \boldsymbol{m}} = \begin{bmatrix} \gamma_1 & 0 \\ 0 & \gamma_2 \end{bmatrix} \tag{4.47}$$

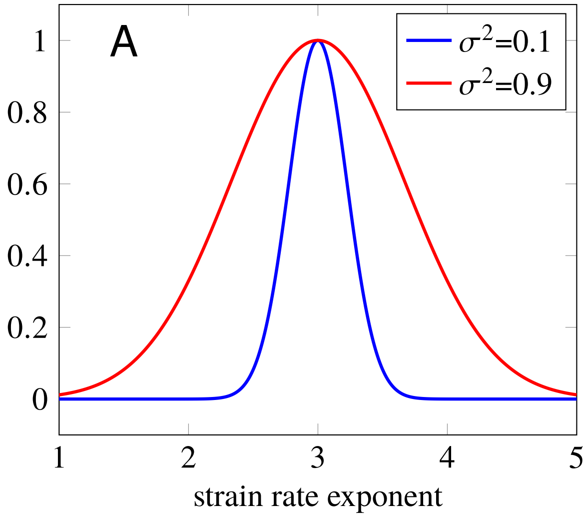

leading to

$$C = \begin{bmatrix} \gamma_1^2 a & \gamma_1\gamma_2 b \\ \gamma_1\gamma_2 b & \gamma_2^2 c \end{bmatrix} \tag{4.48}$$

$$\boldsymbol{\pi}_2 = \mathcal{N}(\mu, \gamma^2\sigma) \tag{4.49}$$

An important point is to construct the covariance matrix for the relationship between the stress and inferred parameters (strain rate exponent, yield stress). To do so, we form the vector $\boldsymbol{\sigma}_a$ such that $\boldsymbol{\sigma}_a = (\boldsymbol{\sigma}, n, \sigma_y..)^\intercal$. Doing so, we find the Jacobian is

$$\frac{\partial \boldsymbol{\sigma}_a}{\partial \boldsymbol{m}} = \frac{\partial[\boldsymbol{\sigma}, n, \sigma_y...]^\intercal}{\partial \boldsymbol{m}} \tag{4.50}$$

which results in

$$C = \begin{bmatrix} \frac{\partial \sigma}{\partial n} & \frac{\partial \sigma_a}{\partial \sigma_y} \\ \frac{\partial n}{\partial n} & \frac{\partial n}{\partial \sigma_y} \\ \frac{\partial \sigma_y}{\partial n} & \frac{\partial \sigma_y}{\partial \sigma_y} \end{bmatrix} \tag{4.51}$$

which leads to

$$C = \begin{bmatrix} \frac{\partial \sigma}{\partial n} & \frac{\partial \sigma_a}{\partial \sigma_y} \\ 1 & 0 \\ 0 & 1 \end{bmatrix} \tag{4.52}$$

Uncertainty estimates for Effective viscosity

While we have developed this machinery for normal and shear stresses, we can extend it to the effective viscosity in a region. The average effective effective viscosity we are interested in is,

$$\eta_{avg} = \exp(\int_{\Omega_i} \log \eta d\Omega_i) \tag{4.53}$$

The jacobian is then,

$$\frac{\partial \eta_{avg}}{\partial \boldsymbol{m}} = \eta_{avg} \int_{\Omega_i} \frac{\eta), i}{\eta} \tag{4.54}$$

The transformation then yields

$$C = \begin{bmatrix} \frac{\partial \boldsymbol{\sigma}}{\partial n} & \dots & \frac{\partial \boldsymbol{\sigma}_a}{\partial \sigma_y} & \\ 1 & 0 & \dots & 0 \\ 0 & 1 & \dots & 0 \\ \vdots & \vdots & \ddots & 0 \\ 0 & 0 & \dots & 1 \end{bmatrix} \tag{4.55}$$

Chapter 5

FUTURE WORK

In this dissertation, we have developed the machinery to infer the rheological parameters using adjoints and in turn construct the Hessian to obtain robust estimates of the plate couplings and global rheological parameters such as the strain rate exponent, yield stress and activation energy. We first used a proof of concept model in Chapter 2 where we considered an idealized geophysical scenario where we had young and old subduction zones with various forces acting on the plates. We were able to illustrate how well our methods were able to infer the parameters and understand where the adjoint falls short. Furthermore, we made use of the covariance matrix (inverse of the Hessian) to obtain the trade-offs between the rheological parameters and understand how those parameters affect surface observables such as plate velocity.

Building on this work in Chapter 2, we extend these methods to include average effective viscosity data where available. Furthermore, we extend our statistical estimation to extrinsic quantities such as stresses in the the fault zones and local viscosities. By doing so, we were able to infer not only the plate couplings but the average shear and normal stresses within some of the major subduction zones.

We also extended our methods to using topography data and show a proof of concept model for a simple sphere falling in the viscous mantle. While we determine the adjoint for stress data, we encountered computational limitations with free-slip boundary conditions. We found that the free-slip boundary condition does not allow for realistic topography and instead we encountered larger stresses than are observed at oceanic trenches.

Moving forward, there needs to be changes to the forward model, namely the boundary condition such that there is a more robust method for the forward prediction of topography at trenches such that those forward model results can be incorporated into an inverse problem. While incorporating topography is an important aspect of this inverse problem, the use of the gravity field can be of fundamental importance for these types of inverse problems. Previous work have made use of the geoid (a surface of the geoid potential) to test forward models results with less realistic approaches. Incorporating the geoid can be formulated in such a way to allow for a self-gravitating model with present day observations which would be a large step toward more accurate uncertainty quantification in geodynamics. Incorporating the geoid in such a way, would require a similar formulation of the adjoing and Hessian based on work presented in this thesis.

While topography as a measure of stress is important data, the observed stress orientations within plates and slabs is another constraint that can be incorporated. However, formulating the adjoint based on stress orientations is not clear as it requires care on whether the misfit should focus on the direction of stress orientations and then how to map this post-processing of the data to an inverse problem. Incorporating different kinds of data is important; however, understanding which parameters are sensitive to which data is important as it can help to reduce the variance of an inferred parameter. To aid in this, one can use global sensitivity analysis to determine which parameters can best explain the data, which in turn will allow for more high fidelity estimates of such parameters.

While we have outlined how to improve upon the parameter inference, there are underlying issues pertaining to data uncertainty. In our forward models, we assume that there is no error in the buoyancy distribution, which is not the case based on a hierarchy of geophysical models. However, attempting to constrain the data uncertainty of the buoyancy is not simple as the degree to which the thermal distribution of slab can vary is not well constrained. Furthermore, the uncertainty of the fault zone geometry must be taken into account, as this can influence the range of inferred estimates of the rheology. Additionally, accounting for model discrepancy is a next step in making uncertainty estimates. Therefore, while we have focused on the traditional case of using surface observations to inform the rheological parameters while adding a statistical estimation using the Hessian, there still is a limitation in which our uncertainty quantification methodology does not take into account model error. Building upon these ideas of reformulating the adjoint in the presence of different data, forward propagation of uncertainty and stochastic models for model error can advance the field of uncertainty quantification in geodynamics, which in itself is still in its infancy.

Once inverting for the rheological parameters in a global model, a more rigorous comparison can be made between the broad-scale forces such as the normal force and shear force at plate boundaries to those obtained from inverse cross-sectional models (WEP, Sumatra, Middle America and Tonga). A natural question would be how much strike-slip motion would affect the state of stress of the overriding plates. If there is a change in the state of stress between global and 2D inverse models, then there needs to be more data-constraints on those 2D cross-sections (stress orientation, topography) that can provide more accurate estimations of the state of stress within the plates.

The net-rotation of the lithosphere is a value that can be constrained in global inversions that otherwise could not be investigated in 2D inversions. It is thought that the lithosphere has a net-rotation due to the large variations in effective viscosity. However, constraining the magnitude of the net-rotation depends on the plate motion model used, such as comparing to a fixed hot-spot model or a model that assumes no-net rotation. Furthermore, it would be important to ascertain to what degree-(if any)-the frame of reference would influence the inferred rheological parameters and the state of stress. If there is a pronounced difference between a rotating reference frame compared to a no-net rotational reference frame, then the use of no-net-rotational plate motions should be avoided.

The strength of slabs is important when it comes to building an understanding in how stresses propagate to oceanic plates. Part of the investigation of how strong slabs are can relate to the type of tomography models used in the lower mantle. The structure of the slabs in the lower mantle and the degree to which slabs are connected to oceanic plates can play a roll in the state of stress of the major subduction zones and where great earthquakes occur. It is plausible that the variation in cold material and how firmly slabs are embedded in the lower mantle can change the state of stress and inferred rheology. Thus, investigating the amount of buoyancy in the lower mantle can help in understanding to what degree the anomalies in the lower mantle can impact the state of stress in the slabs compared to what is found in observations.

BIBLIOGRAPHY

Farrington, RJ, L-N Moresi, and FA Capitanio (2014). "The role of viscoelasticity in subducting plates". In: *Geochemistry, Geophysics, Geosystems* 15.11, pp. 4291–4304.

Mao, Xiaolin, Michael Gurnis, and Dave A May (2017). "Subduction initiation with vertical lithospheric heterogeneities and new fault formation". In: *Geophysical Research Letters* 44.22.

Forsyth, D. and S. Uyeda (1975). "On the Relative Importance of the Driving Forces of Plate Motion". In: *Geophysical Journal International* 43.1. DOI: 10.1111/j.1365-246X.1975.tb00631.x, pp. 163–200. eprint: `http://gji.oxfordjournals.org/content/43/1/163.full.pdf+html`. URL: `http://gji.oxfordjournals.org/content/43/1/163.abstract`.

Chapple, W. M. and T. E. Tullis (1977). "Evaluation of the forces that drive the plates". In: *Journal of Geophysical Research* 82.14. 10.1029/JB082i014p01967, pp. 1967–1984. ISSN: 2156-2202. URL: `http://dx.doi.org/10.1029/JB082i014p01967`.

Conrad, C. P. and C. Lithgow-Bertelloni (2002). "How Mantle Slabs Drive Plate Tectonics". In: *Science* 298.5591. DOI: 10.1126/science.1074161, pp. 207–209. eprint: `http://www.sciencemag.org/content/298/5591/207.full.pdf`. URL: `http://www.sciencemag.org/content/298/5591/207.abstract`.

Conrad, C. P. and B. H. Hager (1999). "Effects of plate bending and fault strength at subduction zones on plate dynamics". In: *Journal of Geophysical Research: Solid Earth* 104.B8. DOI: 10.1029/1999JB900149, pp. 17551–17571. ISSN: 2156-2202. URL: `http://dx.doi.org/10.1029/1999JB900149`.

Buffett, B. A. and D. B. Rowley (2006). "Plate bending at subduction zones: Consequences for the direction of plate motions". In: *Earth and Planetary Science Letters* 245.1, pp. 359–364.

Buffett, B. A. and T. W. Becker (2012). "Bending stress and dissipation in subducted lithosphere". In: *Journal of Geophysical Research: Solid Earth* 117.B5. DOI: 10.1029/2012JB009205. ISSN: 2156-2202. URL: `http://dx.doi.org/10.1029/2012JB009205`.

Elsasser, W. M. (1969). "Convection and stress propagation in the upper mantle." In: *The Application of Modern Physics to the Earth and Planetary Interiors*, pp. 1–41.

Stadler, G. et al. (2010). "The Dynamics of Plate Tectonics and Mantle Flow: From Local to Global Scales". In: *Science* 329.5995. DOI: 10.1126/science.1191223, pp. 1033–1038. eprint: `http://www.sciencemag.org/content/329/5995/`

`1033.full.pdf`. URL: `http://www.sciencemag.org/content/329/5995/1033.abstract`.

Scholz, C. H. and J. Campos (1995). “On the mechanism of seismic decoupling and back arc spreading at subduction zones”. In: *Journal of Geophysical Research* 100.B11, pp. 22103–22.

Uyeda, Seiya and Hiroo Kanamori (1979). “Back-arc opening and the mode of subduction”. In: *Journal of Geophysical Research: Solid Earth* 84.B3, pp. 1049–1061.

Ruff, L. and H. Kanamori (1983a). “Seismic coupling and uncoupling at subduction zones”. In: *Tectonophysics* 99.2–4. http://dx.doi.org/10.1016/0040-1951(83)90097-5, pp. 99–117. ISSN: 0040-1951. URL: `http://www.sciencedirect.com/science/article/pii/0040195183900975`.

– (1983b). “Seismic coupling and uncoupling at subduction zones”. In: *Tectonophysics* 99.2, pp. 99–117.

Stein, Seth and Emile A Okal (2007). “Ultralong period seismic study of the December 2004 Indian Ocean earthquake and implications for regional tectonics and the subduction process”. In: *Bulletin of the Seismological Society of America* 97.1A, S279–S295.

Conrad, Clinton P, Susan Bilek, and Carolina Lithgow-Bertelloni (2004). “Great earthquakes and slab pull: interaction between seismic coupling and plate–slab coupling”. In: *Earth and Planetary Science Letters* 218.1, pp. 109–122.

Scholz, C. H. and J. Campos (2012). “The seismic coupling of subduction zones revisited”. In: *Journal of Geophysical Research: Solid Earth (1978–2012)* 117.B5.

Ruina, Andy (1983). “Slip instability and state variable friction laws”. In: *Journal of Geophysical Research: Solid Earth* 88.B12, pp. 10359–10370.

Geersen, Jacob et al. (2015). “Subducting seamounts control interplate coupling and seismic rupture in the 2014 Iquique earthquake area”. In: *Nature communications* 6.

Karato, S. and P. Wu (1993). “Rheology of the upper mantle: A synthesis”. In: *Science* 260.5109, pp. 771–778.

Zhong, Shijie (2001). “Role of ocean-continent contrast and continental keels on plate motion, net rotation of lithosphere, and the geoid”. In: *Journal of Geophysical research* 106.B1, pp. 703–712.

Billen, M. I. and G. Hirth (2005). “Newtonian versus non-Newtonian upper mantle viscosity: Implications for subduction initiation”. In: *Geophysical Research Letters* 32.19. DOI: 10.1029/2005GL023457. ISSN: 1944-8007. URL: `http://dx.doi.org/10.1029/2005GL023457`.

Billen, M. I. and G. Hirth (2007). “Rheologic controls on slab dynamics”. In: *Geochemistry, Geophysics, Geosystems* 8.8. DOI: 10.1029/2007GC001597. ISSN: 1525-2027. URL: `http://dx.doi.org/10.1029/2007GC001597`.

Forte, A. M. and W. R. Peltier (1991). “Viscous flow models of global geophysical observables: 1. Forward problems”. In: *Journal of Geophysical Research: Solid Earth* 96.B12. DOI: 10.1029/91JB01709, pp. 20131–20159. ISSN: 2156-2202. URL: `http://dx.doi.org/10.1029/91JB01709`.

Ghosh, A., T. W. Becker, and S. J. Zhong (2010). “Effects of lateral viscosity variations on the geoid”. In: *Geophysical Research Letters* 37.1. DOI: 10.1029/2009GL040426. ISSN: 1944-8007. URL: `http://dx.doi.org/10.1029/2009GL040426`.

Tarantola, A. (2002). *Inverse problem theory: Methods for data fitting and model parameter estimation*. Elsevier Science.

Baumann, T. S., B. J. P. Kaus, and A. A. Popov (2014). “Constraining effective rheology through parallel joint geodynamic inversion”. In: *Tectonophysics* 631. DOI:10.1016/j.tecto.2014.04.037, pp. 197–211.

Argus, D. and R. Gordon (1991). “No-net-rotation model of current plate velocities incorporating plate motion model NUVEL-1”. In: *Geophysical Research Letters* 18, pp. 2039–2042.

Argus, D. F., R. G. Gordon, and C. DeMets (2011). “Geologically current motion of 56 plates relative to the no-net-rotation reference frame”. In: *Geochemistry, Geophysics, Geosystems* 12.11. DOI: 10.1029/2011GC003751. ISSN: 1525-2027. URL: `http://dx.doi.org/10.1029/2011GC003751`.

Petra, N. and G. Stadler (2011). *Model variational inverse problems governed by partial differential equations*. Tech. rep. 11-05. The Institute for Computational Engineering and Sciences, The University of Texas at Austin.

Kikuchi, M. and H. Kanamori (1995). “The Shikotan earthquake of October 4, 1994: lithospheric earthquake”. In: *Geophysical research letters* 22.9, pp. 1025–1028.

Ruff, L. J. (1989). “Do trench sediments affect great earthquake occurrence in subduction zones?” In: *Subduction Zones Part II*. Springer, pp. 263–282.

Hager, B. H. and R. J. O’Connell (1981). “A simple global model of plate dynamics and mantle convection”. In: *Journal of Geophysical Research: Solid Earth (1978–2012)* 86.B6, pp. 4843–4867.

Forte, A. M. and W. R. Peltier (1987). “Plate tectonics and aspherical Earth structure: The importance of poloidal-toroidal coupling”. In: *Journal of Geophysical Research* 92.B5, pp. 3645–3679.

Zhong, S., M. Gurnis, and L. Moresi (1998). “Role of faults, nonlinear rheology, and viscosity structure in generating plates from instantaneous mantle flow models”. In: *Journal of Geophysical Research: Solid Earth* 103.B7. DOI: 10.1029/98JB00605, pp. 15255–15268. ISSN: 2156-2202. URL: `http://dx.doi.org/10.1029/98JB00605`.

Alisic, L., M. Gurnis, G. Stadler, C. Burstedde, and O. Ghattas (2012). “Multi-scale dynamics and rheology of mantle flow with plates”. In: *Journal of Geophysical Research: Solid Earth* 117.B10. DOI: 10.1029/2012JB009234. ISSN: 2156-2202. URL: `http://dx.doi.org/10.1029/2012JB009234`.

Alisic, L., M. Gurnis, G. Stadler, C. Burstedde, L. C. Wilcox, et al. (2010). “Slab stress and strain rate as constraints on global mantle flow”. In: *Geophysical Research Letters* 37.22. DOI: 10.1029/2010GL045312. ISSN: 1944-8007. URL: `http://dx.doi.org/10.1029/2010GL045312`.

Ismail-Zadeh, A. et al. (2004). “Inverse problem of thermal convection: numerical approach and application to mantle plume restoration”. In: *Physics of the Earth and Planetary Interiors* 145.1–4. DOI: http://dx.doi.org/10.1016/j.pepi.2004.03.006, pp. 99–114. ISSN: 0031-9201. URL: `http://www.sciencedirect.com/science/article/pii/S0031920104001384`.

Spasojevic, S., L. Liu, and M. Gurnis (2009). “Adjoint models of mantle convection with seismic, plate motion, and stratigraphic constraints: North America since the Late Cretaceous”. In: *Geochemistry, Geophysics, Geosystems* 10.5. DOI: 10.1029/2008GC002345, Q05W02. ISSN: 1525-2027. URL: `http://dx.doi.org/10.1029/2008GC002345`.

Bunge, H.-P., C. R. Hagelberg, and B. J. Travis (2003). “Mantle circulation models with variational data assimilation: inferring past mantle flow and structure from plate motion histories and seismic tomography”. In: *Geophysical Journal International* 152.2. 10.1046/j.1365-246X.2003.01823.x, pp. 280–301. ISSN: 1365-246X. URL: `http://dx.doi.org/10.1046/j.1365-246X.2003.01823.x`.

Horbach, A., H.-P. Bunge, and J. Oeser (2014). “The adjoint method in geodynamics: derivation from a general operator formulation and application to the initial condition problem in a high resolution mantle circulation model”. In: *Int J Geomath.* DOI: 10.1007/s13137-014-0061-5, pp. 1–32.

Worthen, J. et al. (2014). “Towards an adjoint-based inversion for rheological parameters in nonlinear viscous mantle flow”. In: *Physics of Earth and Planetary Interiors* 234. DOI: 10.1016/j.pepi.2014.06.006, pp. 23–34.

Stocker, R. L. and M. F. Ashby (1973). “On the rheology of the upper mantle”. In: *Reviews of Geophysics* 11.2, pp. 391–426.

Tarantola, A. (2005). *Inverse Problem Theory and Methods for Model Parameter Estimation*. Philadelphia, PA: SIAM, pp. xii+342.

Kaipio, J. and E. Somersalo (2005). *Statistical and Computational Inverse Problems*. Vol. 160. Applied Mathematical Sciences. New York: Springer-Verlag, pp. xvi+339.

Vogel, C. R. (2002). *Computational Methods for Inverse Problems*. Vol. 23. SIAM.

Nocedal, J. and S. J. Wright (2006). *Numerical Optimization*. second. Berlin, Heidelberg, New York: Springer Verlag.

Hastings, W. K. (1970). “Monte Carlo sampling methods using Markov chains and their applications”. In: *Biometrika* 57.1, pp. 97–109.

Gilks, W. R. (2005). *Markov Chain Monte Carlo*. Wiley Online Library.

Tröltzsch, F. (2010). *Optimal Control of Partial Differential Equations: Theory, Methods and Applications*. Vol. 112. Graduate Studies in Mathematics. American Mathematical Society.

Petra, N., H. Zhu, et al. (2012). “An inexact Gauss-Newton method for inversion of basal sliding and rheology parameters in a nonlinear Stokes ice sheet model”. In: *Journal of Glaciology* 58.211, pp. 889–903.

Bui-Thanh, T. et al. (2013). “A computational framework for infinite-dimensional Bayesian inverse problems Part I. The linearized case, with application to global seismic inversion”. In: *SIAM Journal on Scientific Computing* 35.6, A2494–A2523.

Hayes, G. P., D. J. Wald, and R. L. Johnson (2012). “Slab 1.0: A three-dimensional model of global subduction zone geometries”. In: *Journal of Geophysical Research: Solid Earth* 117.B01302. DOI: 10.1029/2011JB008524. URL: `http://dx.doi.org/10.1029/2011JB008524`.

Elman, H. C., D. J. Silvester, and A. J. Wathen (2005). *Finite Elements and Fast Iterative Solvers with applications in incompressible fluid dynamics*. Oxford: Oxford University Press.

King, S. D. and B. H. Hager (1990). “The relationship between plate velocity and trench viscosity in Newtonian and power-law subduction calculations”. In: *Geophysical Research Letters* 17.13. DOI: 10.1029/GL017i013p02409, pp. 2409–2412. ISSN: 1944-8007. URL: `http://dx.doi.org/10.1029/GL017i013p02409`.

Haario, H. et al. (2006). “DRAM: efficient adaptive MCMC”. In: *Statistics and Computing* 16.4, pp. 339–354.

Robert, Christian P and George Casella (2004). *Monte Carlo statistical methods*. Vol. 319. Citeseer.

Arredondo, K. M. and M. I. Billen (2012). “Rapid weakening of subducting plates from trench-parallel estimates of flexural rigidity”. In: *Phys. Earth Planet. Int.* 196–197. DOI: 10.1016/j.pepi.2012.02.007, pp. 1–13.

Wells, R. E. and W. McCaffrey (2013). “Steady rotation of the Cascade arc”. In: *Geology* 41.9. DOI: 10.1130/G34514.1, pp. 127–130.

McCaffrey, R. et al. (2013). “Active tectonics of northwestern U.S. inferred from GPS-derived surface velocities”. In: *Journal of Geophysical Research: Solid Earth* 118. DOI: 10.1029/2012JB009473, pp. 1–15.

Gordon, R. and S. Stein (1992). “Global tectonics and space geodesy”. In: *Science* 256. DOI: 10.1126/science.256.5055.333, pp. 333–342.

Gordon, R. G., C. DeMets, and J.-Y. Royer (1998). “Evidence for long-term diffuse deformation of the lithosphere of the equatorial Indian Ocean”. In: *Nature* 395. DOI:10.1038/26463, pp. 370–374.

Kreemer, C. W. et al. (2012). “A geodetic strain rate model for the Pacific-North American plate boundary, western United States”. In: *Nevada Bureau of Mines and Geology Map* 178.

Ratnaswamy, Vishagan, Georg Stadler, and Michael Gurnis (2015). “Adjoint-based estimation of plate coupling in a non-linear mantle flow model: theory and examples”. In: *Geophysical Journal International* 202.2, pp. 768–786.

Gripp, A. E. and R. G. Gordon (1990). “Current plate velocities relative to the hotspots incorporating the NUVEL-1 global plate motion model”. In: *Geophysical Research Letters* 17.8. DOI: 10.1029/GL017i008p01109, pp. 1109–1112. ISSN: 1944-8007. URL: `http://dx.doi.org/10.1029/GL017i008p01109`.

Kreemer, Corné, William E Holt, and A John Haines (2003). “An integrated global model of present-day plate motions and plate boundary deformation”. In: *Geophysical Journal International* 154.1, pp. 8–34.

Hager, Bradford H, Robert W Clayton, et al. (1984). “Lower mantle heterogeneity, dynamic topography and the geoid”. In:

Flament, Nicolas, Michael Gurnis, and R Dietmar Müller (2013). “A review of observations and models of dynamic topography”. In: *Lithosphere* 5.2, pp. 189–210.

Yang, Ting and Michael Gurnis (2016). “Dynamic topography, gravity and the role of lateral viscosity variations from inversion of global mantle flow”. In: *Geophysical Journal International* 207.2, pp. 1186–1202.

Moresi, Louis and Michael Gurnis (1996a). “Constraints on the lateral strength of slabs from three-dimensional dynamic flow models”. In: *Earth and Planetary Science Letters* 138.1-4, pp. 15–28.

Kaufmann, Georg and Kurt Lambeck (2000). “Mantle dynamics, postglacial rebound and the radial viscosity profile”. In: *Physics of the Earth and Planetary Interiors* 121.3, pp. 301–324.

Billen, Magali I and Michael Gurnis (2001). “A low viscosity wedge in subduction zones”. In: *Earth and Planetary Science Letters* 193.1, pp. 227–236.

Korenaga, Jun and Shun-Ichiro Karato (2008). “A new analysis of experimental data on olivine rheology”. In: *Journal of Geophysical Research: Solid Earth* 113.B2.

Rudi, Johann et al. (2015). “An extreme-scale implicit solver for complex PDEs: highly heterogeneous flow in earth’s mantle”. In: *Proceedings of the international conference for high performance computing, networking, storage and analysis*. ACM, p. 5.

Crameri, F, CR Lithgow-Bertelloni, and PJ Tackley (2017). “The dynamical control of subduction parameters on surface topography”. In: *Geochemistry, Geophysics, Geosystems*.

Davies, Geoffrey F and James N Brune (1971). “Regional and global fault slip rates from seismicity”. In: *Nature* 229.4, pp. 101–107.

Bletery, Quentin et al. (2016). “Mega-earthquakes rupture flat megathrusts”. In: *Science* 354.6315, pp. 1027–1031.

Song, Teh-Ru Alex and Mark Simons (2003). “Large trench-parallel gravity variations predict seismogenic behavior in subduction zones”. In: *Science* 301.5633, pp. 630–633.

Kanamori, H. and J. J. Cipar (1974). “Focal process of the great Chilean earthquake May 22, 1960”. In: *Physics of the Earth and Planetary Interiors* 9, pp. 128–136.

McCaffrey, Robert (2008). “Global frequency of magnitude 9 earthquakes”. In: *Geology* 36.3, pp. 263–266.

Burstedde, Carsten, Georg Stadler, et al. (2013). “Large-scale adaptive mantle convection simulation”. In: *Geophysical Journal International* 192.3. 10.1093/gji/ggs070, pp. 889–906.

Zhong, S. and M. Gurnis (1995). “Mantle Convection with Plates and Mobile, Faulted Plate Margins”. In: *Science* 267.5199. DOI: 10.1126/science.267.5199.838, pp. 838–843. eprint: `http://www.sciencemag.org/content/267/5199/838.full.pdf`. URL: `http://www.sciencemag.org/content/267/5199/838.abstract`.

Hu, Yan et al. (2016). “Asthenosphere rheology inferred from observations of the 2012 Indian Ocean earthquake”. In: *Nature*.

Cathles, Lawrence M (2015). *Viscosity of the Earth’s Mantle*.

Mitrovica, JX and WR Peltier (1995). “Constraints on mantle viscosity based upon the inversion of post-glacial uplift data from the Hudson Bay region”. In: *Geophysical Journal International* 122.2, pp. 353–377.

Simons, Mark and Bradford H Hager (1997). “Localization of the gravity field and the signature of glacial rebound”. In: *Nature* 390.6659, pp. 500–504.

Ranalli, Giorgio (1995). *Rheology of the Earth*. Springer Science & Business Media.

Müller, R Dietmar et al. (1997). “Digital isochrons of the world’s ocean floor”. In: *Journal of Geophysical Research: Solid Earth* 102.B2, pp. 3211–3214.

Simmons, Nathan A et al. (2012). “LLNL-G3Dv3: Global P wave tomography model for improved regional and teleseismic travel time prediction”. In: *Journal of Geophysical Research: Solid Earth* 117.B10.

Ritsema, Jeroen, Hendrik Jan van Heijst, and John H Woodhouse (1999). “Complex shear wave velocity structure imaged beneath Africa and Iceland”. In: *Science* 286.5446, pp. 1925–1928.

Burstedde, Carsten, Lucas C Wilcox, and Omar Ghattas (2011). “p4est: Scalable algorithms for parallel adaptive mesh refinement on forests of octrees”. In: *SIAM Journal on Scientific Computing* 33.3, pp. 1103–1133.

Bercovici, David (1993). “A simple model of plate generation from mantle flow”. In: *Geophysical Journal International* 114.3, pp. 635–650.

Mei, S et al. (2010). “Experimental constraints on the strength of the lithospheric mantle”. In: *Journal of Geophysical Research: Solid Earth* 115.B8.

Zhong, Shijie and AB Watts (2013). “Lithospheric deformation induced by loading of the Hawaiian Islands and its implications for mantle rheology”. In: *Journal of Geophysical Research: Solid Earth* 118.11, pp. 6025–6048.

Zhong, Shijie and Michael Gurnis (1996). “Interaction of weak faults and non-Newtonian rheology produces plate tectonics in a 3D model of mantle flow”. In: *Nature* 383.6597, p. 245.

Moresi, L. and M. Gurnis (1996b). “Constraints on the lateral strength of slabs from three-dimensional dynamic flow models”. In: *Earth and Planetary Science Letters* 138.1–4. DOI: http://dx.doi.org/10.1016/0012-821X(95)00221-W, pp. 15–28. ISSN: 0012-821X. URL: `http://www.sciencedirect.com/science/article/pii/0012821X9500221W`.

Brune, James N, Thomas L Henyey, and Robert F Roy (1969). “Heat flow, stress, and rate of slip along the San Andreas fault, California”. In: *Journal of Geophysical Research* 74.15, pp. 3821–3827.

Heuret, Arnauld et al. (2012). “Relation between subduction megathrust earthquakes, trench sediment thickness and upper plate strain”. In: *Geophysical Research Letters* 39.5.

Gripp, Alice E and Richard G Gordon (2002). “Young tracks of hotspots and current plate velocities”. In: *Geophysical Journal International* 150.2, pp. 321–361.

Appendix A

ANALYSIS OF DATA COVARIANCE FOR PLATE MOTION MODELS

ABSTRACT

The incorporation of plate motion data to infer the mantle's rheology is important. Doing so requires a variety of assumptions such as the rigidity of the plates in addition to the pole of rotation, both of which are uncertain. Furthermore, there is an issue of what the correct reference frame should be for an absolute plate motion model. We will focus our attention on the no-net rotation reference frame and analyze the data uncertainty between plate pairs. Unfortunately, this reference frame assumes that there is zero lithosphere rotation, which is incorrect because of lateral variations in viscosity. An important part of the optimization procedure is the incorporation of data uncertainty. The plate motion model that contains the covariance information is the NNR-MORVEL56 model that contains the correlation between plates. We will perform an analysis on the covariances to determine how certain plates (size and proximity) correlate with each other.

A.1 Introduction

Slab pull is probably the dominant force driving plate motions and associated mantle flow, there remains substantial uncertainty on the relative coupling of stresses across plate boundaries at subduction zones. This coupling can either be attributed to broad-scale tectonics forces or to the varying properties between the plates at each subduction zone. While it is not clear whether broad-scale forces or the varying tectonic properties have the stronger contribution to the variations in seismic coupling, a valid model should appropriately represent the broad-scale forces.

To accurately constrain these broad-scale forces requires minimizing the misfit of observed data such as plate motions. To first order, the rheological parameters can be constrained by using plate motion data for rigid areas (Ratnaswamy et al., 2015). While plate motion data is important in constraining the mantle's rheology, there lies a problem in which reference frame should be used. The multiple reference frames are the no-net rotation reference frame where it is assumed that the net rotation of the lithosphere is zero. However, from mantle flow models with lateral variations in viscosity, this is not the case.

When using Bayesian inversions to infer parameter distributions, we make assumptions of the underlying parameter distributions (normal distribution). Furthermore, we assume the form of the prior along with its mean and variance. The posterior distribution takes the form of

The data covariance matrix C_{data}^{-1} is typically treated as a diagonal matrix when there is not a good estimate of data uncertainty. However, for plate motions, we do have a more complete estimate of data uncertainties in terms of a *full* covariance matrix for each plate relative to each other. The covariance matrix is given for the Euler pole for each plate pair.

An important issue is how to transform this covariance matrix for Euler poles to that of surface velocities.

A.2 Transformation of Covariance

When plate motion data re constructed, there typically involves using a chi-squares test on the data. It appears that the covariance for the uncertainty of plate motion uncertainties are done through a linear propagation. What this means is that the data uncertainty that goes into all these plate motion models are pulled from different methods.

It appears that after the Euler poles for each plates are found, the authors use the errors for each plate to build a 3x3 covariance matrix in x-y-z space. Therefore each entry relates to *xx,yy,zz,xy,xz..* For each plate pair there is a covariance matrix. The linear propagation method that the authors use that the covariance for the transformation is also Gaussian.

As an example we will consider the uncertainty for plate motion. We are interested in the misfit in surface velocity data,

$$\mathbf{Cov}(\omega, \omega) = \mathcal{E}[(\omega - \omega_{mean})^T (\omega - \omega_{mean})] \tag{A.1}$$

A motion of a point on the sphere can be described by **Euler's fixed point theorem**. Euler's fixed point theorem states that a point that a displacement of a point on a rigid body can be described by a rotation about an axis through that point. When looking at plate motion data, one usually has the latitude and longitude of the Euler pole. To convert the Euler pole to plate velocity we need to use the cross product formula,

$$\mathbf{u} = \omega \quad \mathrm{x} \quad \mathbf{r} \tag{A.2}$$

To review, the spherical to Cartesian transformation is,

$$\begin{aligned} x &= r \cos\theta \cos\phi \\ y &= r \cos\theta \sin\phi \\ z &= r \sin\theta. \end{aligned} \tag{A.3}$$

To transform the angular rotation to Cartesian coordinates from spherical,

$$\begin{aligned} \omega_x &= \omega \cos\theta \cos\phi \\ \omega_y &= \omega \cos\theta \sin\phi \\ \omega_z &= \omega \sin\theta. \end{aligned} \tag{A.4}$$

To transform rotation to angular velocity, the following holds, In the literature, one is provided with the rotation rate ω and the latitude and longitude for a plate pair. The covariance matrices are reported in terms of the rotation rate as function of Cartesian coordinates.

A.3 Covariance Mapping

To map the covariance from angular velocity in spherical coordinates, to its Cartesian components, one will need the Jacobian of the transformation,

$$\frac{\partial \boldsymbol{\omega}}{\partial \mathbf{x}_{sphere}} = \frac{\partial \boldsymbol{\omega}}{\partial (r, \theta, \phi)} \tag{A.5}$$

or

$$\frac{\partial \boldsymbol{\omega}}{\partial \mathbf{x}_{sphere}} = \begin{bmatrix} \frac{\partial \omega_r}{\partial r} & \frac{\partial \omega_r}{\partial r} & \frac{\partial \omega_r}{\partial r} \\ \frac{\partial \omega_\theta}{\partial r} & \frac{\partial \omega_\theta}{\partial r} & \frac{\partial \omega_\theta}{\partial r} \\ \frac{\partial \omega_\phi}{\partial r} & \frac{\partial \omega_\phi}{\partial r} & \frac{\partial \omega_\phi}{\partial r} \end{bmatrix} \tag{A.6}$$

Transforming the covariance matrix,

$$C(x, y, z) = [\frac{\partial \boldsymbol{\omega}}{\partial \mathbf{x}_{sphere}}]^T C(r, \theta, \phi)[\frac{\partial \boldsymbol{\omega}}{\partial \mathbf{x}_{sphere}}] \tag{A.7}$$

The terms in the Jacobian are,

$$\begin{aligned} \frac{\partial \omega_x}{\partial r} &= 0 \\ \frac{\partial \omega_x}{\partial \theta} &= -\omega \sin\theta \cos\phi \\ \frac{\partial \omega_x}{\partial \phi} &= -\omega \cos\theta \sin\phi \\ \frac{\partial \omega_y}{\partial r} &= 0 \\ \frac{\partial \omega_y}{\partial \theta} &= -\omega \sin\theta \cos\phi \\ \frac{\partial \omega_y}{\partial \phi} &= \omega \cos\theta \cos\phi \\ \frac{\partial \omega_x}{\partial r} &= 0 \\ \frac{\partial \omega_x}{\partial \theta} &= \omega \cos\theta \\ \frac{\partial \omega_x}{\partial \phi} &= 0 \end{aligned} \tag{A.8}$$

Note that the velocity is

$$\begin{aligned} v_x &= \omega_y \cdot z - \omega_z \cdot y \\ v_y &= -(\omega_x \cdot z - \omega_z \cdot x) \\ v_z &= \omega_x \cdot y - \omega_y \cdot x \end{aligned} \tag{A.9}$$

Since we are dealing with the misfit in plate motions, we need the covariance matrix for each plate pair as a function of velocity. We therefore need to map the covariance from angular velocity to surface velocity. To do so we form the following Jacobian,

$$\frac{\partial \mathbf{v}}{\partial \boldsymbol{\omega}} = \frac{\partial \mathbf{v}}{\partial (\omega_x, \omega_y, \omega_z)} \tag{A.10}$$

The Jacobian is then,

$$\frac{\partial \mathbf{v}}{\partial \boldsymbol{\omega}} = \begin{bmatrix} \frac{\partial v_x}{\partial \omega_x} & \frac{\partial v_x}{\partial \omega_x} & \frac{\partial v_y}{\partial \omega_z} \\ \frac{\partial v_y}{\partial \omega_x} & \frac{\partial v_y}{\partial \omega_y} & \frac{\partial v_y}{\partial \omega_z} \\ \frac{\partial v_z}{\partial \omega_x} & \frac{\partial v_z}{\partial \omega_y} & \frac{\partial v_z}{\partial \omega_z} \end{bmatrix} \tag{A.11}$$

The partial derivatives in the Jacobian are,

$$\begin{aligned} \frac{\partial v_x}{\partial \omega_x} &= 0 \\ \frac{\partial v_x}{\partial \omega_y} &= z \\ \frac{\partial v_x}{\partial \omega_z} &= y \\ \frac{\partial v_y}{\partial \omega_x} &= -z \\ \frac{\partial v_y}{\partial \omega_y} &= 0 \\ \frac{\partial v_y}{\partial \omega_z} &= x \\ \frac{\partial v_z}{\partial \omega_x} &= y \\ \frac{\partial v_z}{\partial \omega_y} &= -x \\ \frac{\partial v_z}{\partial \omega_z} &= 0 \end{aligned} \tag{A.12}$$

The following holds,

$$\frac{\partial \mathbf{v}}{\partial \boldsymbol{\omega}} = \begin{bmatrix} 0 & z & y \\ -z & 0 & x \\ y & -x & 0 \end{bmatrix} \tag{A.13}$$

A.4 Reference Frames

Since we may be interested in looking at euler poles relative a to certain reference frame, we will need to look at relative motion. To do so we consider the following where we consider the relative motion between plates A,B and C,

$$\begin{aligned} \boldsymbol{\omega}_{A\backslash B} &= \boldsymbol{\omega}_{A\backslash C} + \boldsymbol{\omega}_{C\backslash B} \\ &= \boldsymbol{\omega}_{A\backslash C} - \boldsymbol{\omega}_{B\backslash C} \end{aligned} \tag{A.14}$$

However, we may also consider adding a rotational component to the NNR covariance matrix. We will define the rotation vector as,

$$\omega_i = \omega_{NNR} + \omega_{ROT} \tag{A.15}$$

We will define the following,

$$\begin{aligned} \omega_N &= \omega_{NNR} \\ \omega_R &= \omega_{ROT} \end{aligned} \tag{A.16}$$

Assuming we have the covariance matrix for ω_{ROT} then we can make use of,

$$\begin{aligned} C(\omega_i, \omega_j) &= C([\omega_N + \omega_R]_i, [\omega_N + \omega_R]_j) \\ &= C(\omega_{Ni} + \omega_{R_i}, \omega_{N_j} + \omega_{R_j}) \end{aligned} \tag{A.17}$$

which yields,

$$\begin{aligned} C([\omega_N + \omega_R]_i, [\omega_N + \omega_R]_j) &= C(\omega_{N_i}, \omega_{N_j}) + C(\omega_{N_i}, \omega_{R_j}) + C(\omega_{R_i}, \omega_{N_j}) + C(\omega_{R_i}, \omega_{R_j}) \\ &= C(\omega_{N_i}, \omega_{N_j}) + 2C(\omega_{N_i}, \omega_{R_j}) + C(\omega_{R_i}, \omega_{R_j}) \end{aligned} \tag{A.18}$$

There would be a minor issue with is the covariance term $C(\omega_N, \omega_R)$ since we do not have this covariance matrix explicitly. However, we can assume that the random variables $\omega_{NNR}, \omega_{ROT}$ are uncorrelated, which means

$$C(\omega_{N_i}, \omega_{R_j}) = 0 \tag{A.19}$$

In the case of the rotational and NNR component of the angular velocity being uncorrelated, then

$$C([\omega_N + \omega_R]_i, [\omega_N + \omega_R]_j) = C(\omega_{N_i}, \omega_{N_j}) + C(\omega_{R_i}, \omega_{R_j}) \tag{A.20}$$

A.5 No-Net Rotation Reference Frame

We have data uncertainty for the Euler Poles (Argus, Gordon, and DeMets, 2011), however this data uncertainty is using the NNR reference frame. Furthermore, the data uncertainty is on the angular velocity components $(\omega_x, \omega_y, \omega_z)$. There are 56 plates, so there 168 (56 x 3) random variables, which results in a covariance matrix of 168 x 168. However, we need to extract this information for each plate, which ultimately requires either conditioning or marginalizing this data covariance matrix for each plate. What we have is a global data uncertainty matrix,

$$C_{data} = \begin{bmatrix} c_{1,1} & x_{1,2} & c_{1,3} & \cdots & c_{1,168} \\ c_{2,1} & c_{2,2} & c_{2,3} & \cdots & c_{2,168} \\ \vdots & \vdots & \vdots & \ddots & \vdots \\ c_{168,1} & c_{168,2} & c_{168,3} & \cdots & c_{168,168} \end{bmatrix} \tag{A.21}$$

The problem arises as our cost function,

$$\mathcal{J} = \int \frac{1}{2}(O\boldsymbol{u} - \boldsymbol{u}_{obs})^T C_{data}^{-1}(O\boldsymbol{u} - \boldsymbol{u}_{obs}) \tag{A.22}$$

where $C_{data} = C_{data}(\mathbf{x})$, and $\boldsymbol{u} = \boldsymbol{u}(\mathbf{x}$. To extract the appropriate information we need to either marginalize or condition on C_{data}. If one were interested in solely the data covariance for a particular plate regardless of the other 55 plates, then the marginal distribution would be appropriate. To marginalize the distribution would be computing $\boldsymbol{\pi}(p1) = \int \boldsymbol{\pi}(p1, p2, p3.., p56)dp2...dp56$. To compute the marginal covariance for plate1, we will define the global data covariance in block format,

$$C_{data} = \begin{bmatrix} C_{11} & C_{12} \\ C_{21} & C_{22} \end{bmatrix} \tag{A.23}$$

The covariance matrix from marginalizaing the distribution (plate1)

$$C(x, y, z)[plate1] = C_{11} \tag{A.24}$$

However, if one wants to include the correlations between the other plates, one should consider the conditional data distribution, i.e. $\boldsymbol{\pi}(p1|p2...p56)$. To do this we would compute the data covariance for each plate, conditioning on the other 55 plates.

$$C_{p1} = C_{11} - C_{12}C_{22}^{-1}C_{21} \tag{A.25}$$

Effectively compute the appropriate Schur complement for each plate, then transform from angular velocity data space to translational data space.

However, we can make a comparison by plotting the plate velocity vectors (N-S and E-W components) with their error ellipses. This is done in Fig. A.2.

Example using Nazca Plate

We will consider the Nazca plate from (Argus, Gordon, and DeMets, 2011), where we have the data covariance for the three angular velocity components. Note the units of the covariance is given in $rads^2/Ma^2$. We will first look at the marginal

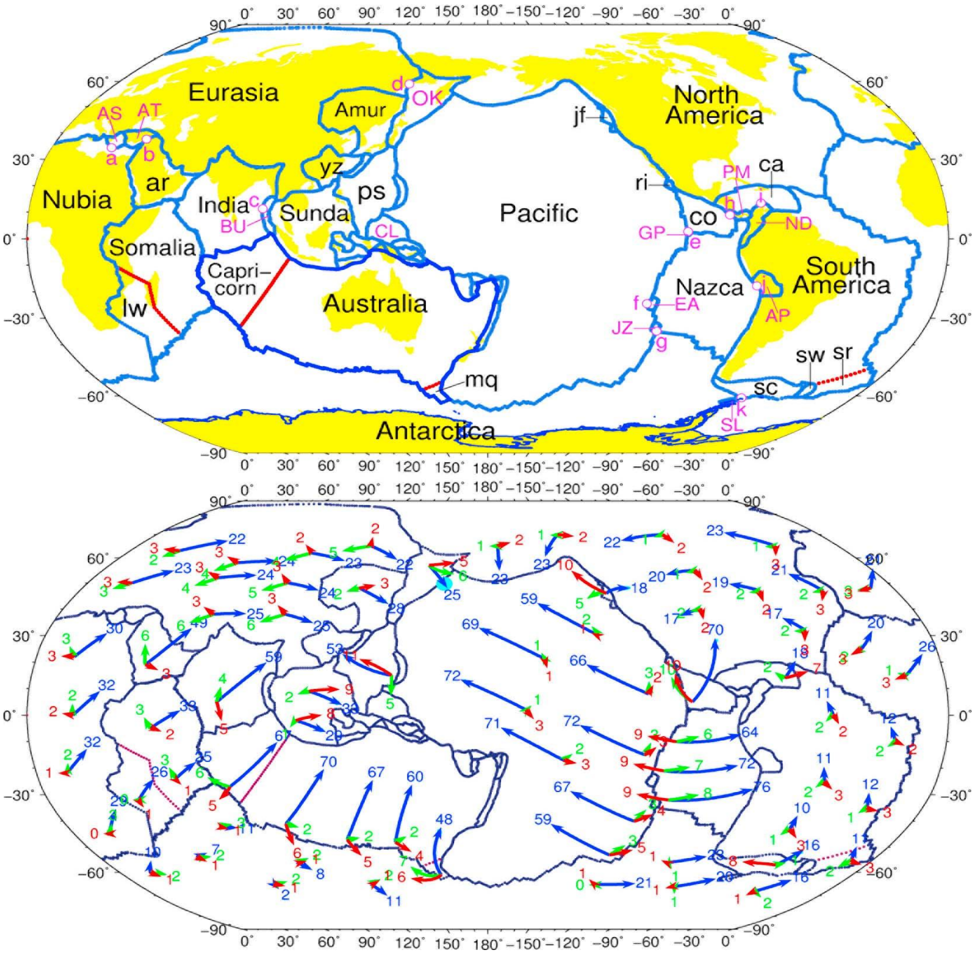

Figure A.1: Plates on the surface of the earth and the vectors from (Argus, Gordon, and DeMets, 2011)

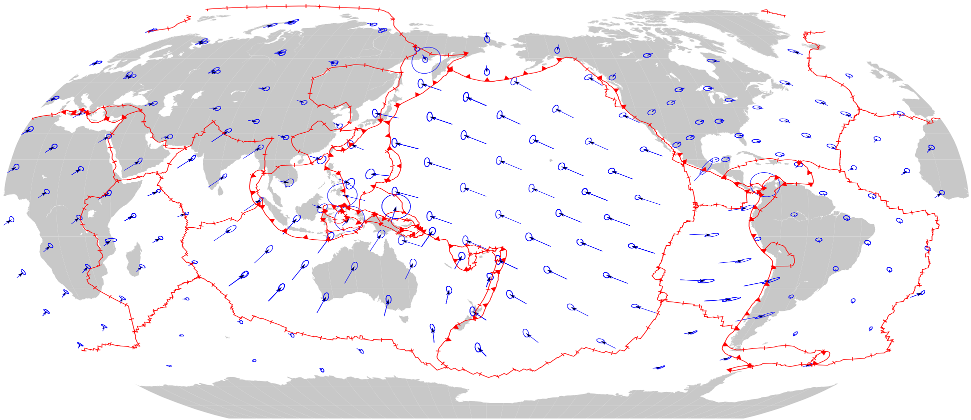

Figure A.2: Plates on the surface of the earth with velocity vectors and corresponding error ellipses

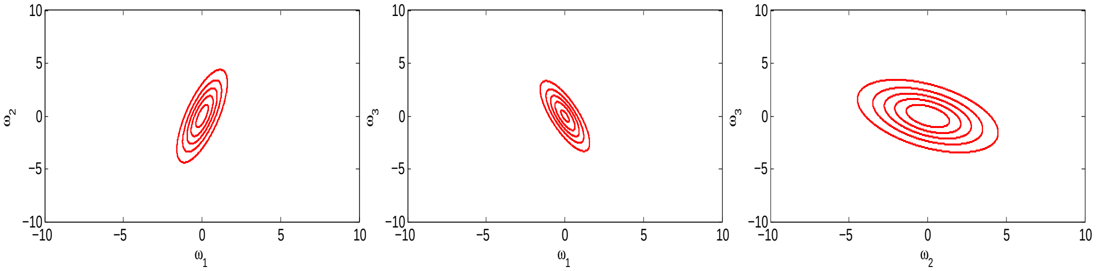

Figure A.3: Covariance data distributions for Nazca between each of its angular velocity components (a)ω_1 vs ω_2 (b)ω_1 vs ω_3 (c)ω_2 vs ω_3

data covariance for Nazca, which can be found in the supplement or in Table 2 of (Argus, Gordon, and DeMets, 2011). The marginal data covariance for Nazca is

$$C_{Nazca} = \begin{bmatrix} 75 & 147 & -121 \\ 147 & 564 & -199 \\ -121 & -199 & 332 \end{bmatrix} \tag{A.26}$$

Note Eq (A.26) is in units of 10^{-10} $rads^2/Ma^2$. It is important to note that we assume for the data distribution as $\boldsymbol{\pi}(Nazca) = \mathcal{N}(0, C_{Nazca})$, essentially a normal distribution with mean of zero ($\mu = 0$) and a covariance distribution of C_{Nazca}. Below, we show the data covariance distribution for Nazca (marginal) between its three components ($\omega_1, \omega_2, \omega_3 rads/Myr$). Note, for plotting purposes, the units of C_{Nazca} is $10^{-8} rads^2/Ma^2$. However, since mantle flow models produce a degree-1 rotation because of lateral variations in viscosity, we will add a rotational component to each Euler pole for a new reference frame. To do so, we assume that this new reference frame (e.g. moving hotspot reference frame) has a covariance distribution (diagonal assumed) and is indpendent of the NNR reference frame. Then the new covariance is transformed as,

$$C([\omega_{NNR} + \omega_{HS}]_i, [\omega_{NNR} + \omega_{HS}]_j) = C(\omega_{NNR_i}, \omega_{NNR_j}) + C(\omega_{HS_i}, \omega_{HS_j}) \tag{A.27}$$

where C_{NNR} is the covariance for the NNR reference frame and C_{HS} is the covariance for the rotational velocity in the hot-spot reference frame. As an example, we will create C_{HS} by choosing a diagonal covariance with entries that are the RMS of the diagonal of C_{NNR}. The blue contours in the figure below are the transformed covariance in this reference frame.

Pacific Plate vs Amur Plate

We consider the effect that the Amur plate has on the Pacific plate. We form the marginal covariance distribution from the 168x168 global data covariance between

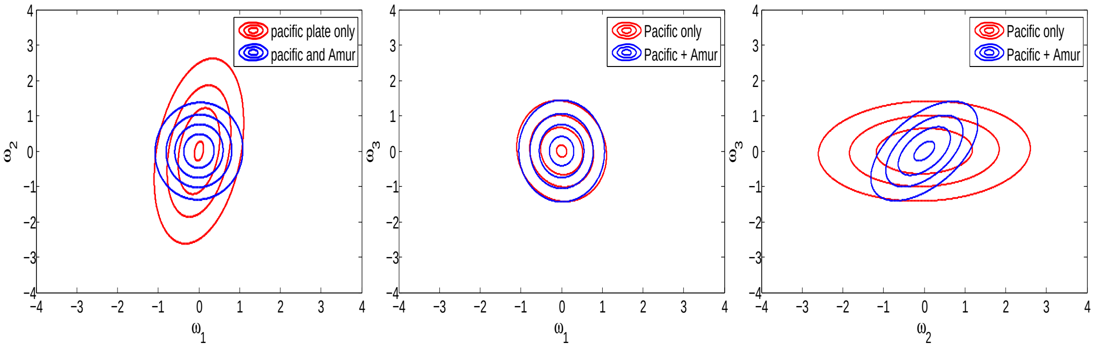

Figure A.4: Covariance data distributions for Pacific (conditioned on Amur) with a rotational component between each of its angular velocity components (a)ω_1 vs ω_2 (b)ω_1 vs ω_3 (c)ω_2 vs ω_3

the Pacific and Amur rotation covariances in Eq. (A.28).

$$C_{Pacific-Amur} = \begin{bmatrix} 43.2 & 31.3 & -4.7 & 28.7 & 16.3 & -9.5 \\ 31.3 & 244.8 & 7.6 & 157.8 & 110.7 & 79.4 \\ -4.7 & 7.6 & 72.5 & -24.4 & -13.8 & -10.1 \\ 28.7 & 157.8 & -24.4 & 223 & -67.2 & -102.2 \\ 16.3 & 110.7 & -13.8 & -67.2 & 376.3 & 309.3 \\ -9.5 & 79.4 & -10.1 & -102.2 & 309.3 & 535.3 \end{bmatrix} \tag{A.28}$$

From there, we then compute the effect that Amur has on the Pacific plate (angular velocity) by forming the conditional distribution below Eq. (A.29)

$$C_{Pacific-Amur-cond} = \begin{bmatrix} 36.828 & 1.5397 & -0.35517 \\ 1.5397 & 59.916 & 34.757 \\ -0.35517 & 34.757 & 68.491 \end{bmatrix} \tag{A.29}$$

The comparison of the data covariance between the angular velocity components of the Pacific plate by itself (red contours) and with the effect of Amur (blue contours) is shown in the figure below.

Pacific Plate vs Juan DeFuca Plate

We consider the effect that the Amur plate has on the Pacific plate. We form the marginal covariance distribution from the 168x168 global data covariance between the Pacific and Amur rotation covariances in Eq. (A.30).

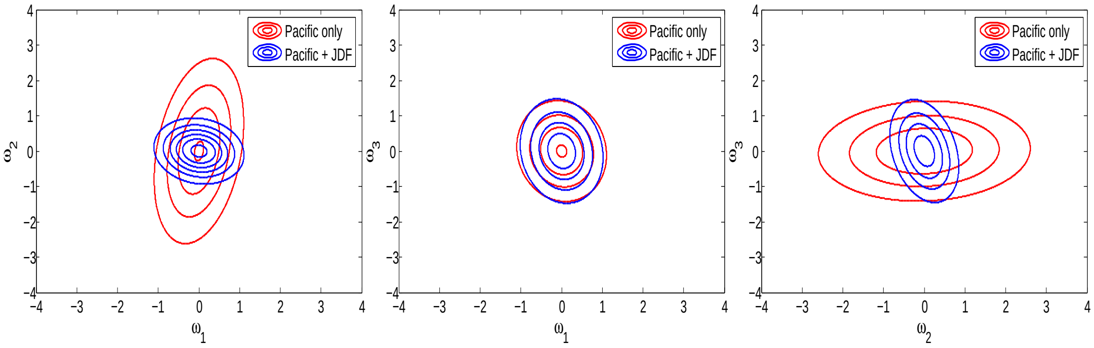

Figure A.5: Covariance data distributions for Pacific (conditioned on JDF) with a rotational component between each of its angular velocity components (a)ω_1 vs ω_2 (b)ω_1 vs ω_3 (c)ω_2 vs ω_3

$$C_{Pacific-JDF} = \begin{bmatrix} 43.2 & 31.3 & -4.7 & 70.2 & 47.6 & 8.7 \\ 31.3 & 244.8 & 7.6 & 289.9 & 400.4 & 134.2 \\ -4.7 & 7.6 & 72.5 & -15.3 & 1 & 67.7 \\ 70.2 & 289.9 & -15.3 & 10237 & 13370 & -15644 \\ 47.6 & 400.4 & 1 & 13370 & 17959 & -20659 \\ 8.7 & 134.2 & 67.7 & -15644 & -20659 & 25637 \end{bmatrix} \tag{A.30}$$

From there, we then compute the effect that Amur has on the Pacific plate (angular velocity) by forming the conditional distribution below Eq. (A.31)

$$C_{Pacific} = \begin{bmatrix} 33.148 & -3.3644 & -5.9062 \\ -3.3644 & 23.626 & -12.348 \\ -5.9062 & -12.348 & 69.803 \end{bmatrix} \tag{A.31}$$

The comparison of the data covariance between the angular velocity components of the Pacific plate by itself (red contours) and with the effect of Juan DeFuca (blue contours) is shown in the figure below.

Pacific Plate vs Nazca Plate

We consider the effect that the Amur plate has on the Pacific plate. We form the marginal covariance distribution from the 168x168 global data covariance between

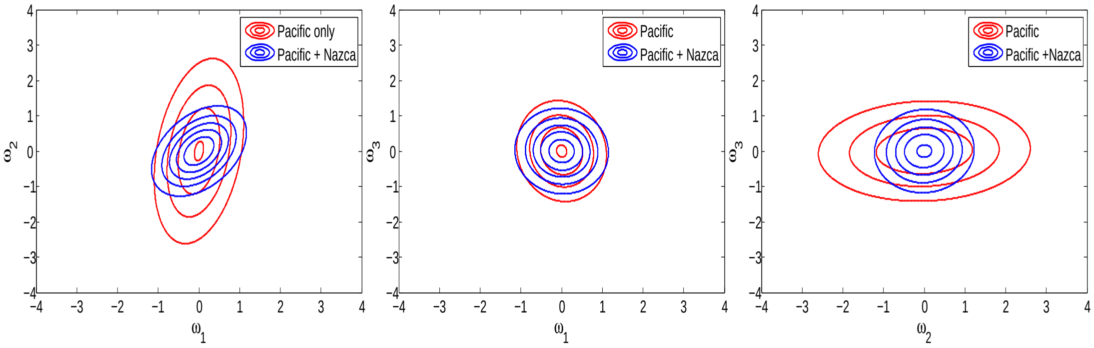

Figure A.6: Covariance data distributions for Pacific (conditioned on Nazca) with a rotational component between each of its angular velocity components (a)ω_1 vs ω_2 (b)ω_1 vs ω_3 (c)ω_2 vs ω_3

the Pacific and Amur rotation covariances in Eq. (A.32).

$$C_{Pacific-Nazca} = \begin{bmatrix} 43.2 & 31.3 & -4.7 & 3.3 & -12.8 & 13.8 \\ 31.3 & 244.8 & 7.6 & -98.1 & -263.2 & 231.8 \\ -4.7 & 7.6 & 72.5 & -12 & 60.5 & 49.5 \\ 3.3 & -98.1 & -12 & 74.7 & 147.1 & -120.7 \\ -12.8 & -263.2 & 60.5 & 147.1 & 563.6 & -199.2 \\ 13.8 & 231.8 & 49.5 & -120.7 & -199.2 & 332.2 \end{bmatrix} \tag{A.32}$$

From there, we then compute the effect that Amur has on the Pacific plate (angular velocity) by forming the conditional distribution below Eq. (A.33)

$$C_{Pacific} = \begin{bmatrix} 38.074 & 16.921 & -1.275 \\ 16.921 & 45.629 & 1.8067 \\ -1.275 & 1.8067 & 42.195 \end{bmatrix} \tag{A.33}$$

The comparison of the data covariance between the angular velocity components of the Pacific plate by itself (red contours) and with the effect of Nazca (blue contours) is shown in the figure below.

Pacific Plate vs Cocos Plate

We consider the effect that the Cocos plate has on the Pacific plate. We form the marginal covariance distribution from the 168x168 global data covariance between

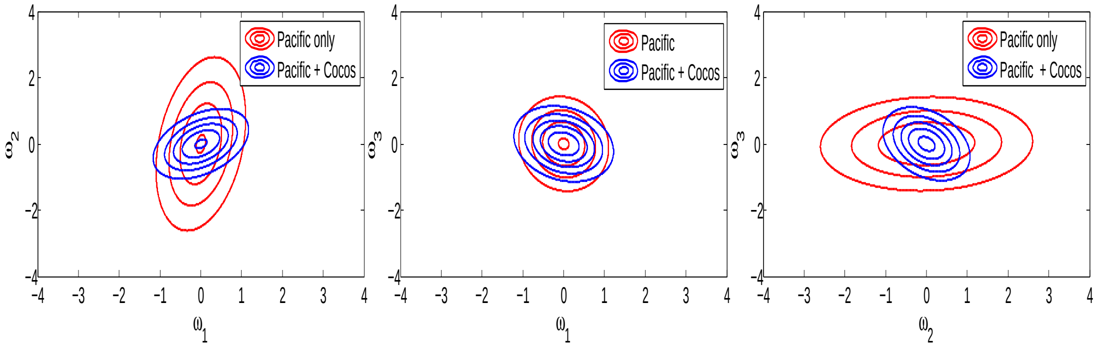

Figure A.7: Covariance data distributions for Pacific (conditioned on Cocos) with a rotational component between each of its angular velocity components (a)ω_1 vs ω_2 (b)ω_1 vs ω_3 (c)ω_2 vs ω_3

the Pacific and Cocos rotation covariances in Eq. (A.34).

$$C_{Pacific-Cocos} = \begin{bmatrix} 43.2 & 31.3 & -4.7 & -27.4 & -5.8 & 26.8 \\ 31.3 & 244.8 & 7.6 & -393.3 & -101.3 & 337.8 \\ -4.7 & 7.6 & 72.5 & 0.2 & 49 & 49.5 \\ -27.4 & -393.3 & 0.2 & 774.4 & 273.3 & -616.2 \\ -5.8 & -101.3 & 49 & 273.3 & 1035.6 & -366.5 \\ 26.8 & 337.8 & 49.5 & -616.2 & -366.5 & 613.1 \end{bmatrix} \tag{A.34}$$

From there, we then compute the effect that Amur has on the Pacific plate (angular velocity) by forming the conditional distribution below Eq. (A.35)

$$C_{Pacific} = \begin{bmatrix} 41.897 & 15.486 & -8.1451 \\ 15.486 & 33.987 & -12.092 \\ -8.1451 & -12.092 & 36.687 \end{bmatrix} \tag{A.35}$$

The comparison of the data covariance between the angular velocity components of the Pacific plate by itself (red contours) and with the effect of Cocos (blue contours) is shown in the figure below.

Pacific Plate vs Nubia Plate

We consider the effect that the Nubia plate has on the Pacific plate. We form the marginal covariance distribution from the 168x168 global data covariance between

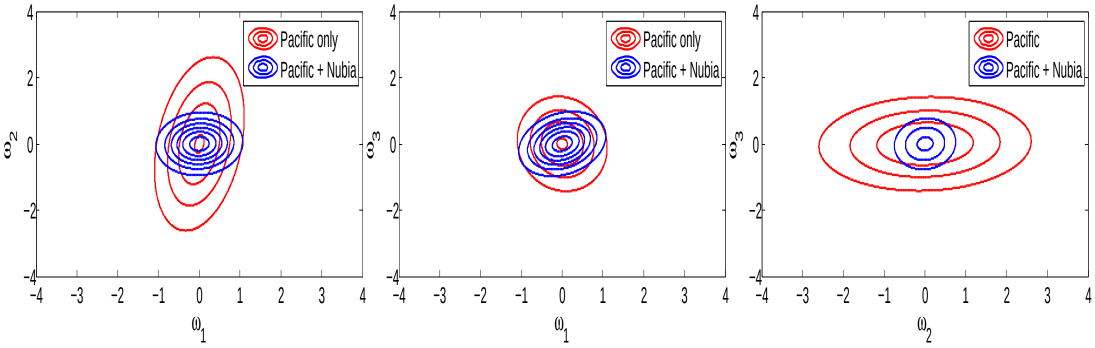

Figure A.8: Covariance data distributions for Pacific (conditioned on Nubia) with a rotational component between each of its angular velocity components (a)ω_1 vs ω_2 (b)ω_1 vs ω_3 (c)ω_2 vs ω_3

the Pacific and Nubia rotation covariances in Eq. (A.38).

$$C_{Pacific-Nubia} = \begin{bmatrix} 43.2 & 31.3 & -4.7 & -16.8 & -16.8 & 12.3 \\ 31.3 & 244.877.6 & -1.4 & -127.4 & -29.6 & \\ -4.7 & 7.6 & 72.5 & 19.1 & 1.7 & -48.0 \\ -16.8 & -1.4 & 19.1 & 30.6 & -0.4 & -27.1 \\ -16.8 & -127.4 & 1.7 & -0.4 & 74.5 & 13.2 \\ 12.3 & -29.6 & -48.0 & -27.1 & 13.2 & 54.1 \end{bmatrix} \tag{A.36}$$

From there, we then compute the effect that Amur has on the Pacific plate (angular velocity) by forming the conditional distribution below Eq. (A.39)

$$C_{Pacific} = \begin{bmatrix} 30.0835 & 1.5338 & 6.6333 \\ 1.5338 & 23.9752 & 1.8159 \\ 6.6333 & 1.8159 & 25.1215 \end{bmatrix} \tag{A.37}$$

The comparison of the data covariance between the angular velocity components of the Pacific plate by itself (red contours) and with the effect of Nubia (blue contours) is shown in the figure below.

Pacific Plate vs Nubia Plate

We consider the effect that the Nubia plate has on the Pacific plate. We form the marginal covariance distribution from the 168x168 global data covariance between

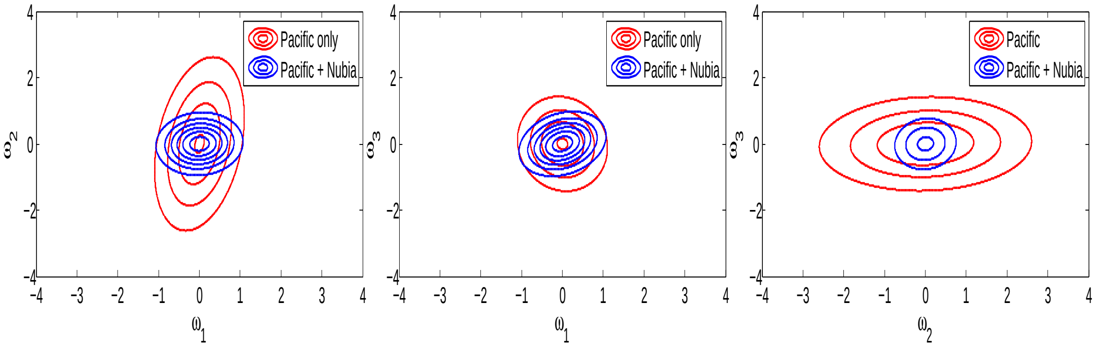

Figure A.9: Covariance data distributions for Pacific (conditioned on Nubia) with a rotational component between each of its angular velocity components (a)ω_1 vs ω_2 (b)ω_1 vs ω_3 (c)ω_2 vs ω_3

the Pacific and Nubia rotation covariances in Eq. (A.38).

$$C_{Pacific-Nubia} = \begin{bmatrix} 43.2 & 31.3 & -4.7 & -16.8 & -16.8 & 12.3 \\ 31.3 & 244.877.6 & -1.4 & -127.4 & -29.6 & \\ -4.7 & 7.6 & 72.5 & 19.1 & 1.7 & -48.0 \\ -16.8 & -1.4 & 19.1 & 30.6 & -0.4 & -27.1 \\ -16.8 & -127.4 & 1.7 & -0.4 & 74.5 & 13.2 \\ 12.3 & -29.6 & -48.0 & -27.1 & 13.2 & 54.1 \end{bmatrix} \tag{A.38}$$

From there, we then compute the effect that Amur has on the Pacific plate (angular velocity) by forming the conditional distribution below Eq. (A.39)

$$C_{Pacific} = \begin{bmatrix} 30.0835 & 1.5338 & 6.6333 \\ 1.5338 & 23.9752 & 1.8159 \\ 6.6333 & 1.8159 & 25.1215 \end{bmatrix} \tag{A.39}$$

The comparison of the data covariance between the angular velocity components of the Pacific plate by itself (red contours) and with the effect of Nubia (blue contours) is shown in the figure below.

Comparison of the correlations between other plate's angular rotation components with Pacific

We compare the the conditional distributions between Nazca, Juan DeFuca, Cocos against Nubia for the Pacific plate. In Table A.1 gives the summary of the correlations the aforementioned plates have with the Pacific Plate.

In Fig.A.10, we compare the conditional distribution of the Pacific-Nubia plate pair with the Pacific-Cocos plate pair.

Table A.1: Comparison of correlations between Pacific and other plates, (ω_i, ω_j) represent the correlation of the Pacific plate's angular velocity with another plate of interest.

Plate	(ω_1, ω_2)	(ω_1, ω_2)	(ω_2, ω_3)
Amur	1.5397	-0.35517	34.757
Juan DeFuca	-3.3644	-5.9062	-12.348
Nazca	16.921	-1.275	1.8067
Cocos	15.486	-8.1451	-12.092
Nubia	1.5338	6.6333	1.8159

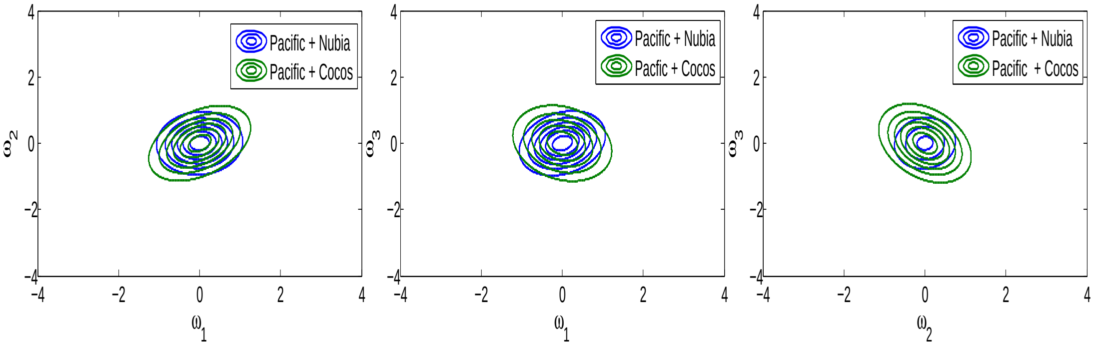

Figure A.10: Covariance data distributions for Pacific (conditioned on Nubia) with a rotational component between each of its angular velocity components (a)ω_1 vs ω_2 (b)ω_1 vs ω_3 (c)ω_2 vs ω_3

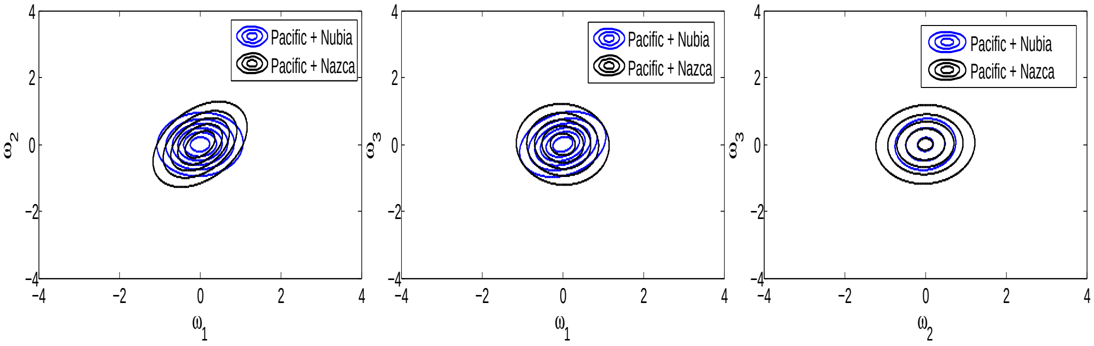

Figure A.11: Covariance data distributions for Pacific (conditioned on Nubia) with a rotational component between each of its angular velocity components (a)ω_1 vs ω_2 (b)ω_1 vs ω_3 (c)ω_2 vs ω_3

In Fig.A.11, we compare the conditional distribution of the Pacific-Nubia plate pair with the Pacific-Nazca plate pair.

In Fig.A.12, we compare the conditional distribution of the Pacific-Nubia plate pair with the Pacific-Juan deFuca plate pair.

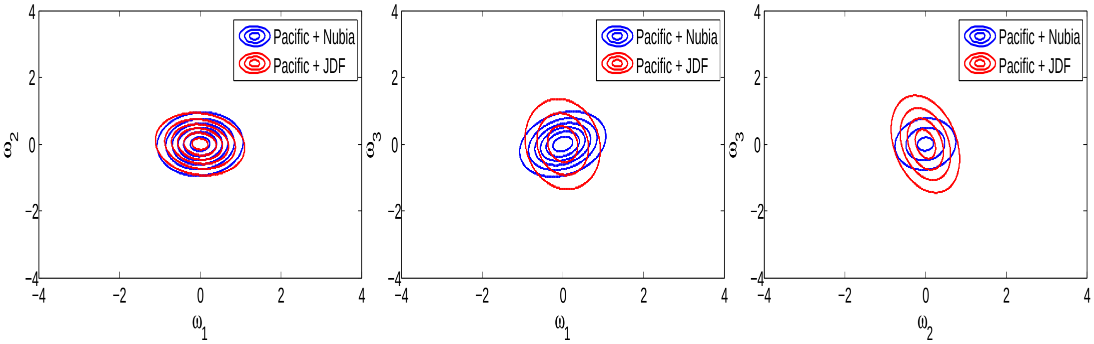

Figure A.12: Covariance data distributions for Pacific (conditioned on Nubia) with a rotational component between each of its angular velocity components (a)ω_1 vs ω_2 (b)ω_1 vs ω_3 (c)ω_2 vs ω_3

Issue with Global covariance in NNR

While we can compute the effect of the other 55 plates on a specific plate of interest, there seems to arise an issue where when we condition the covariance matrix on those other 55 plates, the resulting covariance matrix is no longer positive definite. In fact, one may have negative variances as in the case of the Pacific plate conditioned on the North American Plate. The Pacific-North America Plate covariance is given in Eq. (A.40)

$$C_{Pacific-NorthAmerica} = \begin{bmatrix} 43.2 & 31.3 & -4.7 & -31.4 & -14.3 & -3.3 \\ 31.3 & 244.8 & 7.6 & 18.7 & -170.2 & -95.1 \\ -4.7 & 7.6 & 72.5 & 16.2 & 5.2 & -47.2 \\ -31.4 & 18.7 & 16.2 & 58.5 & -30 & -18.1 \\ -14.3 & -170.2 & 5.2 & -30 & 119.2 & 53.7 \\ -3.3 & -95.1 & -47.2 & -18.1 & 53.7 & 108.1 \end{bmatrix} \tag{A.40}$$

After conditioning Eq. (A.40), we arrive at Eq. (A.41). However, Eq. (A.41) is no longer postivie definite.

$$C_{Pacific} = \begin{bmatrix} 17.443 & -5.6996 & 7.9469 \\ -5.6996 & -14.734 & 11.487 \\ 7.9469 & 11.487 & 38.7 \end{bmatrix} \tag{A.41}$$

Summary

- Plates that are in close proximity to the Pacific plate have stronger correlations (see Cocos compared to Nubia).

- There may be an issue when when conditions the global covariance as in some cases it produces non-positive definite covariance matrices.

A.6 Analysis of Corner Flow and its Application to Normal and Shear stresses in a Viscous Subduction Zone Model

Here, we investigate the normal and shear stress along a certain direction. To do this we look at a corner flow. We will thus analyze a classic case of corner flow from Batchelor. We look at Navier-Stokes system,

$$\begin{aligned} \frac{d\rho}{dt} + \mathbf{u}\nabla\rho = 0 \\ \frac{D(\rho\mathbf{u})}{dt} = \nabla \cdot \sigma + \mathbf{F} \end{aligned} \tag{A.42}$$

With the incompressibility constraint, and assuming the inertial force is negligible, we arrive at,

$$\begin{aligned} \nabla \cdot \mathbf{u} = 0 \\ \nabla p = \mu\nabla^2\mathbf{u} \end{aligned} \tag{A.43}$$

We then simplify to

$$\nabla^2(\nabla^2\psi) = 0 \tag{A.44}$$

with boundary conditions,

$$\frac{\partial\psi}{\partial r} = 0 \qquad \frac{1}{r}\frac{\partial\psi}{\partial\theta} = -U \qquad \text{at} \qquad \theta = 0 \tag{A.45}$$

$$\frac{\partial\psi}{\partial r} = 0 \qquad \frac{1}{r}\frac{\partial\psi}{\partial\theta} = 0\text{at}\theta = \theta_0 \tag{A.46}$$

Note,

$$\begin{aligned} u_r = \frac{1}{r}\frac{\partial\psi}{\partial\theta} \\ u_\theta = -\frac{\partial\psi}{\partial r} \end{aligned} \tag{A.47}$$

The solution for the stream-function is of the form,

$$\psi = \frac{\mathbf{r}U}{\theta_0^2 - \sin^2\theta_0}[-\theta_0^2\sin\theta + (\theta_0 - \sin\theta_0\cos\theta_0)\theta\sin\theta + \sin^2\theta_0\theta\cos\theta] \tag{A.48}$$

Therefore, the velocities are

$$u_\theta = -\frac{U}{\theta_0^2 - \sin^2\theta_0}[-\theta_0^2\sin\theta + (\theta_0 - \sin\theta_0\cos\theta_0)\theta\sin\theta + \sin^2\theta_0\theta\cos\theta] \tag{A.49}$$

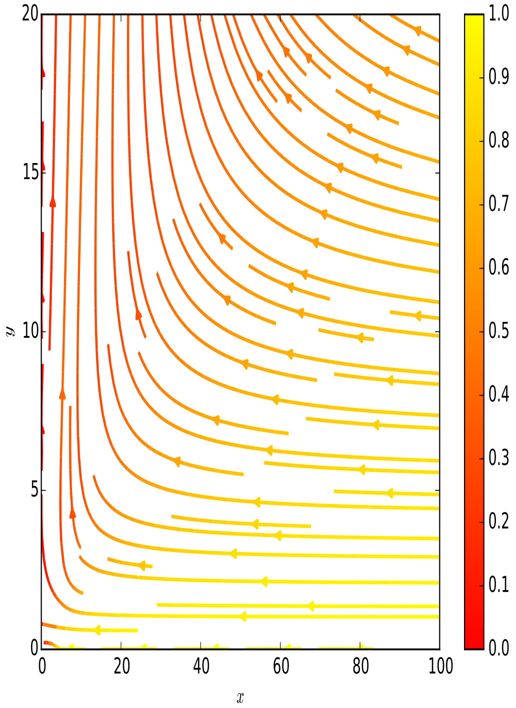

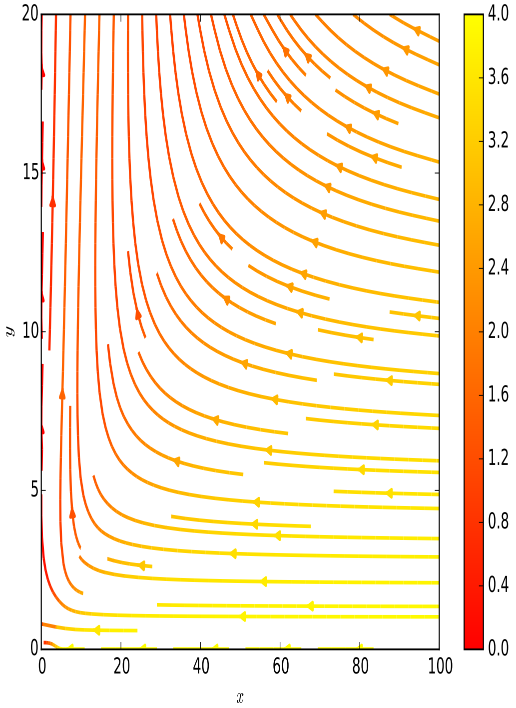

and

$$u_r = \frac{U}{\theta_0^2 - \sin^2\theta_0}[-\theta_0^2\cos\theta+(\theta_0-\sin\theta_0\cos\theta_0)(\sin\theta+\theta\cos\theta)+\sin^2\theta_0(\cos\theta-\theta\sin\theta)] \tag{A.50}$$

The streamlines with the computed velocities are,

We will assume a constant viscosity ($\mu = 1$) and the deviatoric stress tensor is then

$$\sigma = \dot{\boldsymbol{\varepsilon}}(\boldsymbol{u}) \tag{A.51}$$

or

$$\dot{\boldsymbol{\varepsilon}}(\boldsymbol{u}) = \begin{bmatrix} \sigma_{rr} & \sigma_{r\theta} \\ \sigma_{r\theta} & \sigma_{\theta\theta} \end{bmatrix} \tag{A.52}$$

$$\begin{aligned} \sigma_{rr} &= \frac{\partial u_r}{\partial r} \\ \sigma_{\theta\theta} &= (\frac{1}{r}\frac{\partial u_\theta}{\partial\theta} + \frac{u_r}{r}) \\ \sigma_{r\theta} &= [r\frac{\partial}{\partial r}(\frac{u_\theta}{r}) + \frac{1}{r}\frac{\partial u_r}{\partial\theta}] \end{aligned} \tag{A.53}$$

The analytical expressions for the stress components are,

$$
\begin{aligned}
\sigma_{rr} &= 0 \\
\sigma_{\theta\theta} &= 0 \\
\sigma_{r\theta} &= \frac{U}{r(\theta_0^2 - \sin^2\theta_0)}[-\theta_0^2\cos\theta + (\theta_0 - \sin\theta_0\cos\theta_0)(\sin\theta + \theta\cos\theta) + \sin^2\theta_0(\cos\theta - \theta\sin\theta)] \\
&\quad + \frac{U}{r(\theta_0^2 - \sin^2\theta_0)}[\theta_0^2\sin\theta + (\theta_0 - \sin\theta_0\cos\theta_0)(2\cos\theta - \theta\sin\theta) - \sin^2\theta_0(2\sin\theta - \theta\cos\theta)]
\end{aligned}
\tag{A.54}
$$

Note, the only non-zero stress component is $\sigma_{r\theta}$, or

$$
\begin{aligned}
\sigma_{r\theta} = &\frac{U}{r(\theta_0^2 - \sin^2\theta_0)}[\theta_0^2(\sin\theta - \cos\theta) + \\
&(\theta_0 - \sin\theta_0\cos\theta_0)(\sin\theta + \theta\cos\theta + 2\cos\theta - \theta\sin\theta) + \sin^2\theta_0(\cos\theta - \theta\sin\theta + 2\sin\theta - \theta\cos\theta)]
\end{aligned}
\tag{A.55}
$$

The stress tensor is then,

$$
\dot{\boldsymbol{\varepsilon}}(\boldsymbol{u}) = \begin{bmatrix} 0 & \sigma_{r\theta} \\ \sigma_{r\theta} & 0 \end{bmatrix} \tag{A.56}
$$

As noted by .. the stress varies according to r^{-1}. We then transform the stress-tensor to Cartesian coordinates, with the following rule,

$$
\sigma^{cart} = \mathbf{Q}^T\sigma^{polar}\mathbf{Q} \tag{A.57}
$$

where

$$
\mathbf{Q} = \begin{bmatrix} \cos\theta & -\sin\theta \\ \sin\theta & \cos\theta \end{bmatrix} \tag{A.58}
$$

The Cartesian components as a function of $(\mathbf{r}, \theta)$ are

$$
\begin{aligned}
\sigma_{xx} &= 2\sin\theta\cos\theta\sigma_{r\theta} \\
\sigma_{xy} &= \sigma_{r\theta}(\cos^2\theta - \sin^2\theta) \\
\sigma_{yy} &= -2\sin\theta\cos\theta\sigma_{r\theta}
\end{aligned}
\tag{A.59}
$$

The stress distributions are,

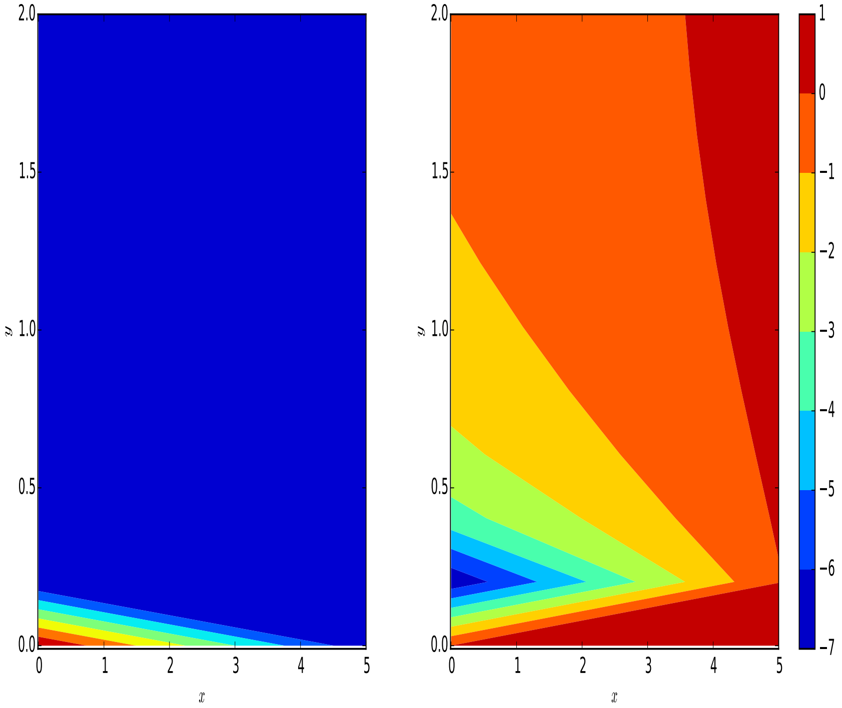
2.0
1.5
1.0
0.5
0.0
y
0
1
2
3
4
5
x
2.0
1.5
1.0
0.5
0.0
y
0
1
2
3
4
5
x
1
0
−1
−2
−3
−4
−5
−6
−7

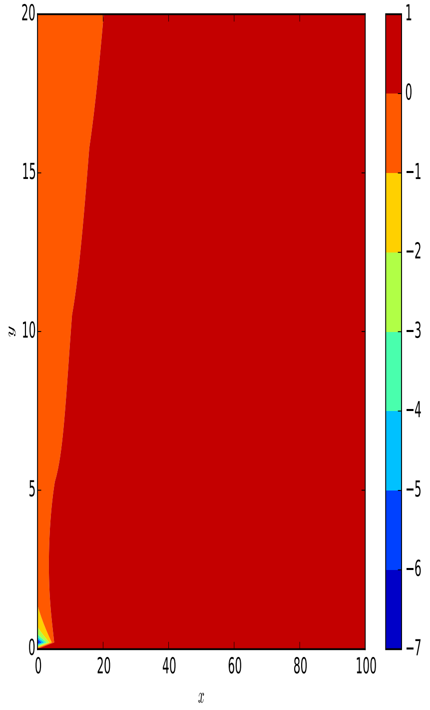
20
15
10
5
0
y
0
20
40
60
80
100
x
1
0
−1
−2
−3
−4
−5
−6
−7